

**GEDIZ UNIVERSITY ★ GRADUATE SCHOOL OF SCIENCE**  
**ENGINEERING AND TECHNOLOGY**

**NANOSTRUCTURES FOR PLASMONIC BIOSENSORS**

**M.Sc. THESIS**

**Aysel TOMAK**

**Institute of Science**

**Nanotechnology Graduate Programme**

**Thesis Supervisor: Assistant Prof. Dr. Hadi M. Zareie**

**JULY 2013**

**GEDIZ UNIVERSITY ★ GRADUATE SCHOOL OF SCIENCE**  
**ENGINEERING AND TECHNOLOGY**

**NANOSTRUCTURES FOR PLASMONIC BIOSENSORS**

**M.Sc. THESIS**

**Aysel TOMAK**  
**60071003**

**Nanotechnology Graduate Programme**

**Thesis Supervisor: Assistant Prof. Dr. Hadi M. Zareie**

**JULY 2013**

**GEDİZ ÜNİVERSİTESİ ★ FEN BİLİMLERİ ENSTİTÜSÜ**

**PLASMONİK BİYOSENSÖRLER İÇİN NANOYAPILAR**

**YÜKSEK LİSANS TEZİ**

**Aysel Tomak  
(60071003)**

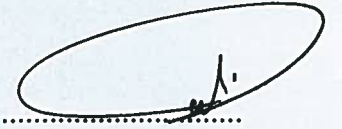
**Nanoteknoloji Yüksek Lisans Programı**

**Tez Danışmanı: Yrd. Doç. Dr. Hadi M. ZAREIE**

**TEMMUZ 2013**

**Aysel TOMAK**, a **M.Sc.** student of Gediz University, **Institute of Science with** student ID No: 60071003, successfully defended the **thesis** entitled **“NANOSTRUCTURES FOR PLASMONIC BIOSENSORS”**, which she prepared after fulfilling the requirements specified in the associated legislations, before the jury whose signatures are below.

**Thesis Advisor :** **Assistant Prof. Dr. Hadi M. ZAREIE**  
Gediz University



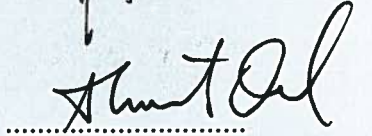
**Jury Members :** **Assistant Prof. Dr. Hadi M. ZAREIE**  
Gediz University



**Assistant Prof. Dr. Mustafa M. DEMIR**  
IYTE, İzmir Institute of Technology



**Prof. Dr. Ahmet ORAL**  
METU, Middle East Technical University



**Date of Submission :** **June 2013**  
**Date of Defense :** **July 2013**

*To my family,*

## ACKNOWLEDGEMENT

I would like to thank my supervisor, Dr. Hadi M. Zareie, for his generous support and encouragement that directly provided the motivation in completion of this thesis. The answers to my many questions, the help learning my way around instruments and softwares, and editorial advice for this thesis has been invaluable. Also his patience with my thesis in reference to completion time has been much appreciated.

I would also like to thank Hasan Aydın for his assistance with AFM and SERS. Thanks to Dr. Volga Bulmus and Ekrem Özer for providing the polymers in this project. A special mention for Uğur Kayran for years of friendship and his valuable help with SPR and conversation.

Furthermore, I am thankful to: Ümit Çelik and Cansu Alpan in Nanomagnetic Instruments for endless patience, advices and servicing during numerous SPM study; Öner Ekiz in Nanodev Ltd. for his help with understanding the LSPR and SERS processes through individual steps.

To my parents; father, mother, and my sister and my brother, for their bottomless love, support. I could not have done this without them.

I would like to thank the TUBITAK (PROJECT NO:110T759) for providing financial support to this project and to me.

## **CERTIFICATE OF ORIGINALITY**

I certify that the work in this thesis has not previously been submitted for a degree nor has it been submitted as part of requirements for a degree except as fully acknowledged within the text.

I also certify that the thesis has been written by me. Any help that I have received in my research work and the preparation of the thesis has been acknowledged. In addition, I certify that all information sources and literature used are indicated in the thesis.

July 2013

Aysel TOMAK

## TABLE OF CONTENTS

	<u>Page</u>
<b>ACKNOWLEDGEMENT</b> .....	<b>III</b>
<b>CERTIFICATE OF ORIGINALITY</b> .....	<b>IV</b>
<b>TABLE OF CONTENTS</b> .....	<b>V</b>
<b>ABBREVIATIONS</b> .....	<b>VII</b>
<b>LIST OF FIGURES</b> .....	<b>IX</b>
<b>NANOSTRUCTURES FOR PLASMONIC BIOSENSORS</b> .....	<b>XIII</b>
<b>ABSTRACT</b> .....	<b>XIII</b>
<b>PLASMONİK BİYOSENSÖRLER İÇİN NANOYAPILAR</b> .....	<b>XIV</b>
<b>ÖZET</b> .....	<b>XIV</b>
<b>1 INTRODUCTION</b> .....	<b>1</b>
1.1 What is a Biosensor? .....	1
1.1.1 The principle of Biorecognition system.....	3
1.1.2 Types of Biosensors .....	4
1.1.3 Biosensor Characteristics .....	5
1.1.4 Applications of Biosensor .....	6
1.1.5 Literature Review .....	7
1.2 Introduction to Localized Surface Plasmon Resonance (LSPR).....	8
1.2.1 Biosensor based on Localized Surface Plasmon Resonance.....	9
1.2.2 Theory behind Localized Surface Plasmon Resonance .....	10
1.2.3 Similarities between SPR and LSPR Sensors .....	12
1.2.4 Literature Review .....	14
1.3 Introduction to Surface Enhanced Raman Scattering (SERS) .....	18
1.3.1 Raman scattering: definition .....	18
1.3.2 Stokes and anti-Stokes scattering.....	19
1.3.3 Raman signal enhancement.....	21
1.3.4 Electromagnetic theory .....	21
1.3.5 Chemical theory .....	22
1.3.6 SERS spectrum .....	22
1.3.7 Enhancement factor (EF) .....	23
1.3.8 Similarities between Raman, Fluorescence and Infrared (IR) Spectroscopy .....	24
1.3.9 Literature Review .....	24
1.4 Nano-Lithography .....	29
1.4.1 Nanosphere Lithography.....	30
1.4.2 Literature Review .....	33
1.5 Nanorods Overview .....	37
1.5.1 Literature Review .....	39
<b>2 EXPERIMENTAL AND METHODS</b> .....	<b>43</b>



2.1	Method for Nanosandwiches.....	43
2.1.1	Materials.....	43
2.1.2	Substrate preparation.....	44
2.1.3	Nanosphere Lithography.....	44
2.1.4	Metal deposition.....	44
2.1.5	Nanostructure functionalization with Temperature Responsive Polymers.....	45
2.1.6	Biorecognition of Nanosandwich arrays for LSPR Biosensor.....	45
2.2	Method for Nanorods (NRs), Nanoparticles (NPs) and Nanobubbles .....	46
2.2.1	Materials.....	46
2.2.2	Gold Nanorod Synthesis .....	46
2.2.3	Production of Gold Nanoparticle from NRs .....	47
2.2.4	Conversion of GNPs to NRs procedure .....	48
2.2.5	Production of Nanobubble and Semi-shell .....	48
2.2.6	Conjugation of GNRs with triangle Gold Nanodot arrays.....	48
2.2.7	Centrifugation .....	48
2.3	Characterization Methods.....	49
2.3.1	UV-Vis / Near IR Spectroscopy.....	49
2.3.2	Localized Surface Plasmon Resonance (LSPR) Spectroscopy .....	49
2.3.3	Surface Enhanced Raman Spectroscopy (SERS).....	50
2.3.4	Surface Plasmon Resonance Spectroscopy (SPRS).....	51
2.3.5	Atomic Force Microscopy (AFM) .....	52
2.3.6	Scanning Electron Microscopy (SEM) .....	53
<b>3</b>	<b>RESULTS AND DISCUSSION .....</b>	<b>55</b>
3.1	Analysis of Nanoarray Structures with Various Noble Metals and Thicknesses .....	55
3.2	Analysis of Single Layer Nanodot Arrays Conjugated Polymer.....	59
3.3	Nanostructure (Nanosandwiches) Arrays Conjugate with Temperature Responsive Polymers .....	62
3.4	Investigation of Polymer Phase Transition on Nanosandwich Arrays.....	76
3.5	Analyses of Bioaffinity Binding to Nanosandwich Arrays Functionalized with a Mix of Thiol-Terminated Polymer.....	80
3.6	Optical Analysis of Gold Nanorods with Different Aspect Ratio.....	85
3.7	Gold Nanorod Preparation with Nitrogen Gas .....	87
3.8	Gold Nanorod Preparation with Argon Gas .....	90
3.9	Conversion of Gold Nanorods to Semi-shell and Bubbles.....	91
3.10	Conjugation of Gold Nanorods with Nanodots Arrays .....	98
<b>4</b>	<b>CONCLUSION .....</b>	<b>101</b>
<b>5</b>	<b>FUTURE WORK.....</b>	<b>103</b>
	<b>REFERENCES.....</b>	<b>104</b>
	<b>CURRICULUM VITAE.....</b>	<b>122</b>

## ABBREVIATIONS

<b>LSPR</b>	: Localized Surface Plasmon Resonance
<b>SERS</b>	: Surface Enhanced Raman Scattering
<b>NSL</b>	: Nanosphere Lithography
<b>MIM</b>	: Metal / Metal oxide (Insulator) / Metal
<b>UV-VIS-NIR</b>	: Ultraviolet Visible Near-Infrared
<b>AFM</b>	: Atomic Force Microscopy
<b>SEM</b>	: Scanning Electron Microscopy
<b>NPs</b>	: Nanoparticles
<b>NRs</b>	: Nanorods
<b>LSP</b>	: Localized Surface Plasmon
<b>SPP</b>	: Surface Plasmon-Polariton
<b>NIR</b>	: Near-Infrared
<b>SPR</b>	: Surface Plasmon Resonance
<b>BSA</b>	: Bovine Serum Albumin
<b>D-FDTD</b>	: Dispersive Finite-Difference Time Domain
<b>SAM</b>	: Self-Assembled Monolayer
<b>VOCs</b>	: Volatile Organic Compounds
<b>MPA</b>	: 3-mercaptopropionic acid
<b>EF</b>	: Enhancement Factor
<b>IR</b>	: Infrared
<b>PSSERES</b>	: Plasmon-Sampled Surface-Enhanced Raman Excitation Spectroscopy
<b>GNP</b>	: Gold Nanoparticle
<b>CT</b>	: Charge-Transfer
<b>PNIPAM</b>	: Poly(N-isopropylacrylamide)
<b>DI</b>	: Deionized
<b>LCST</b>	: Lower Critical Solution Temperature
<b>CTAB</b>	: Cetyl-trimethylammonium bromide
<b>mPEG-SH</b>	: methoxy-poly(ethylene) glycol
<b>PS</b>	: Polystyrene
<b>SL</b>	: Single Layer
<b>DL</b>	: Double Layer
<b>PPAs</b>	: Periodic Particle Arrays
<b>DDA</b>	: Discrete Dipole Approximation
<b>AR NSL</b>	: Angle-Resolved Nanosphere Lithography
<b>HAuCl<sub>4</sub></b>	: Tetrachloroauric (III) acid
<b>GNR</b>	: Gold Nanorod
<b>AR</b>	: Aspect Ratio
<b>PEG</b>	: Poly(ethylene glycol)
<b>SA</b>	: Streptavidin

<b>PBS</b>	: Phosphate-Buffered Saline
<b>Au</b>	: Gold
<b>Al<sub>2</sub>O<sub>3</sub></b>	: Alumina
<b>HfO<sub>2</sub></b>	: Hafnium Oxide
<b>AgNO<sub>3</sub></b>	: Silver Nitrate
<b>NaBH<sub>4</sub></b>	: Sodium borohyride
<b>N<sub>2</sub></b>	: Nitrogen
<b>Ar</b>	: Argon
<b>H<sub>2</sub></b>	: Hydrogen
<b>SPIP</b>	: Scanning Probe Image Processor
<b>HCP</b>	: Hexagonal Close Packing
<b>PDS</b>	: Pyridyldisulfide
<b>RIU</b>	: Refractive Index Unit
<b>DeBrPP</b>	: Diethyl (3-bromopropyl) phosphonate
<b>ATES</b>	: Allyltriethoxysilane
<b>DT</b>	: Decanethiol

## LIST OF FIGURES

	<u>Page</u>
Figure 1.1 Demonstrate publications versus number of the paper in biosensor field. <sup>1</sup>	3
Figure 1.2 Schematic representation of biosensor. ....	4
Figure 1.3 Illustration of the plasmon oscillation in gold nanoparticles.....	9
Figure 1.4 LSPR spectra of each step in the surface modification of NSLderived Ag nanoparticles to form a biotinylated Ag nanobiosensor and the specific binding of SA. (A) Ag nanoparticles before chemical modification, $\lambda_{\max} = 561.4$ nm. (B) Ag nanoparticles after modification with 1 mM 1:3 11-MUA/1-OT, $\lambda_{\max} = 598.6$ nm.(C) Ag nanoparticles after modification with 1 mM biotin, $\lambda_{\max} = 609.6$ nm. (D) Ag nanoparticles after modification with 100 nM SA, $\lambda_{\max} = 636.6$ nm. All extinction measurements were collected in a N <sub>2</sub> environment. <sup>70a</sup> .....	15
Figure 1.5 (A) The disk-shaped nanosandwich is composed of stacked Au, SiO <sub>2</sub> and Au layers, each typically 10 nm thick. The electromagnetic coupling between the fundamental plasmon modes of the upper and lower Au disks can be fine-tuned by either changing the aspect ratio of one of the nanodisks (left) or by varying the thickness of the dielectric spacer layer (right). (B) SEM image of a sandwich array. The diameter of the lower disk is 110 nm and the inset shows a side view of the structure. (C) extinction spectrum from the nanosandwich (D) Mechanical splitting of the coupled plasmonic system, monitored by extinction spectroscopy and AFM profiling. <sup>92</sup> .....	17
Figure 1.6 Different scattering mode of quantum. <sup>51</sup> .....	20
Figure 1.7 The comparison of different scatterings. <sup>51</sup> .....	24
Figure 1.8 (a) SERS of surfactant-capped gold NRs (25±2 in length and 12±2 in width) in solution (solid line) is compared with surfactants (dashed line) and surfactant capped gold nanospheres (12 nm in size) (dotted line).In SERS of NRs the strongest peak is related to the Au–Br vibration, which is closer to the gold surface.(b) Visible spectra of the NRs, surfactant solution, and gold NSs.It can be seen that NRs show strong enhancement despite the fact that the excitation laser is 1064 nm. <sup>113</sup> .....	26
Figure 1.9 Electron micrograph of hexagonally pack nanoparticles onto silicon substrate.....	31
Figure 1.10 AFM images of SL and DL PPAs of M=Ag on S=glass, Si (111), and Cu (100). (A) Ag SL PPA on glass, 437x437 nm image. (B) Ag DL PPA on glass, 757x757 nm image. (C) Ag SL PPA on Si(111), 515x515 nm image. (D) DL PPA on Si(111), 805x805 nm image. (E) Ag SL PPA on Cu(100), 490x490 nm image. (F) Ag DL PPA on Cu(100), 738x738 nm image. <sup>157</sup> .....	34
Figure 1.11 Typical surface plasmon absorption spectrum of gold nanorods. The strong long wavelength band in the near infrared region around 730 nm is due to the	

longitudinal oscillation of electrons and the weak short wavelength band in the visible region around 520 nm is due to the transverse electronic oscillation.....	38
Figure 1.12 Chains of NRs attached to a derivatized substrate. SEM images of A) networks of NR chains attached to the surface of the SAM, and B) a long chain of GNRs. C) High-resolution SEM image of a portion of a chain, which shows a region (arrowed) that appears to contain more than one SA molecule as binder. D) Negative image of (C). E) AFM image of the end portion of a chain. <sup>209</sup> .....	41
Figure 2.1 Schematic representation procedure for preparation of GNR using.....	47
Figure 2.2 Schematic illustration of LSPR Spectroscopy setup. ....	50
Figure 2.3 Schematic illustration of Raman system.....	51
Figure 2.4 A schematic representing the operation of a SPR device. ....	52
Figure 2.5 Atomic Force Microscope. ....	53
Figure 2.6 Ultra plus high resolution field emission-scanning electron microscope. ....	54
Figure 3.1 Schematic illustration of the general process of the nanosandwich arrays preparation by Nanosphere Lithography (NSL). (A) Spin coating of polystyrene beads, (B) Metals deposition, (C) Lift off, (D) Single hexagonal nanosandwich array. ....	56
Figure 3.2 (A) SEM image of hexagonal close pack array of polystyrene with diameter of 500 nm. The inset in panel A represents the higher magnification AFM image with scan area of 1.5x1.5 $\mu\text{m}$ . (B) SEM image of nanodot arrays. The inset in panel B represents the high resolution AFM image at 800x800 nm. (C) Comparison of LSPR shift spectra of Au nanodot arrays on glass. All spectra were produced from a nanosphere deposition mask (D=500 nm) with a constant diameter of $200 \pm 5$ nm and various height of (1) = 50 nm $\lambda_{\text{max}} = 739.09$ nm (2) = 30 nm $\lambda_{\text{max}} = 763.93$ nm (3) = 20 nm $\lambda_{\text{max}} = 794.67$ nm.....	57
Figure 3.3 The LSPR shift peaks between (A) 50 nm Ag nanodot array (a) with $\lambda_{\text{max}} = 527$ nm and 25 nm Ag nanodot array (b) with $\lambda_{\text{max}} = 569$ nm. (B) The LSPR shift spectra shows the different between 50 nm Ag nanodot array with $\lambda_{\text{max}} = 527$ nm (a) and 20 nm Ag / 20 nm $\text{Al}_2\text{O}_3$ / 20 nm Ag nanosandwich array with $\lambda_{\text{max}} = 633$ nm (b). ....	58
Figure 3.4 Comparison of LSPR shift for 25 nm Ag nanodot array with different polystyrene diameter corresponding to (a) D= 500 nm (b) D=1000 nm. ....	59
Figure 3.5 (A) Tapping mode AFM image of 50 nm Au nanodot arrays on silicon substrate. (B) AFM image of thiol terminated polymer functionalized Au nanodot arrays. (C) Comparison of LSPR shift between (a) 50 nm Au nanodot array $\lambda_{\text{max}} = 729.53$ nm and (b) Au nanodot array after thiol terminated polymer conjugation $\lambda_{\text{max}} = 736.16$ nm on glass substrates. (D) SPR sensogram of thiol terminated polymer on gold coated glass. ....	61
Figure 3.6 Comparison of LSPR shift between 90 nm (blue peak) and 60 nm MIM (red peak) nanosandwiches. ....	62
Figure 3.7 (A) Schematic illustration of the functionalized nanosandwich arrays with thiol terminated polymers to Au layers. (B) Tapping mode AFM images of unfunctionalized and (C) functionalized nanosandwich arrays with thiolated polymers on silicon substrate. Inset images in (B and C) represent the scan area of $1.5\mu\text{m} \times 1.5\mu\text{m}$ . (D) Comparison of LSPR shift between (a) unfunctionalized $\lambda_{\text{max}} = 832.24$ nm and (b) functionalized 20 nm Au / 20 nm $\text{Al}_2\text{O}_3$ / 20 nm Au nanosandwich arrays with thiolated polymers $\lambda_{\text{max}} = 849.66$ nm on glass substrates. ....	64
Figure 3.8 (A) Schematic illustration of the functionalized nanosandwich arrays with phosphate terminated polymer to $\text{Al}_2\text{O}_3$ layer. Tapping mode AFM images of (B)	

unfunctionalized and (C) phosphate terminated polymer functionalized nanosandwich arrays on silicon substrate. Inset images in B and C represent the scan area of  $1.5\mu\text{m}\times 1.5\mu\text{m}$ . (D) Comparison of LSPR shift between (a) unfunctionalized  $\lambda_{\text{max}}= 836.6$  nm and (b) functionalized 20 nm Au / 20 nm  $\text{Al}_2\text{O}_3$  / 20 nm Au nanosandwich arrays with phosphate terminated polymer  $\lambda_{\text{max}}= 843.13$  nm on glass substrates. (E) SPR sensogram of non-specific and specific binding events. .... 67

Figure 3.9 (A) Schematic illustration of the functionalized nanosandwiches with thiol and phosphate terminated polymer to  $\text{Al}_2\text{O}_3$  and Au layers. Tapping mode AFM images of (B) unfunctionalized and (C) functionalized nanosandwich arrays with thiol and phosphate terminated polymers. Inset images in B and C represent the scan area of  $1.5\mu\text{m}\times 1.5\mu\text{m}$ . (D) Comparison of LSPR shift of (a) unfunctionalized  $\lambda_{\text{max}}= 831.37$  nm (b) after functionalization of nanosandwich arrays with phosphate  $\lambda_{\text{max}}=838.78$  nm (c) thiol and phosphate terminated polymers  $\lambda_{\text{max}} = 853.13$  nm. .... 70

Figure 3.10 SEM images of unfunctionalized (A) and functionalized nanosandwich arrays with thiol terminated polymer (B), phosphate terminated polymer (C), thiol and phosphate terminated polymers (D). .... 71

Figure 3.11 Comparison of LSPR shift between (A) unfunctionalized 30 nm Au / 30 nm  $\text{Al}_2\text{O}_3$  / 30 nm Au nanosandwich array (blue peak)  $\lambda_{\text{max}}= 751.06$  nm and after thiol terminated polymer binding to nanosandwich array (red peak)  $\lambda_{\text{max}}= 770.09$  nm (B) unfunctionalized 30 nm Au / 30 nm  $\text{Al}_2\text{O}_3$  / 30 nm Au nanosandwich array (blue peak)  $\lambda_{\text{max}}= 743.23$  nm and after phosphate terminated polymer binding to nanosandwich array (red peak)  $\lambda_{\text{max}}= 748.96$  nm on glass substrates. .... 72

Figure 3.12 Comparison LSPR shift between 30 nm Au / 30 nm  $\text{Al}_2\text{O}_3$  / 30 nm Au nanosandwich arrays (A) unfunctionalized  $\lambda_{\text{max}} = 741.02$  nm. (B) after functionalization of nanosandwich arrays with phosphate terminated polymer  $\lambda_{\text{max}} = 746.31$  nm. (C) thiol and phosphate terminated polymers  $\lambda_{\text{max}} = 749.84$  nm. .... 74

Figure 3.13 (A, B) SEM images of functionalized 30 nm Au / 30 nm  $\text{HfO}_2$  / 30 nm Au nanosandwich arrays with silane terminated polymers. (C) Tapping mode AFM image of functionalized nanosandwich arrays with silane terminated polymers. (D) Comparison of LSPR spectra between unfunctionalized (a)  $\lambda_{\text{max}}= 918.8$  nm and functionalized with silane terminated polymers (b)  $\lambda_{\text{max}}= 928.8$  nm. .... 75

Figure 3.14 (A) Schematic illustration of the functionalized nanosandwich arrays with thiol terminated polymer above the LCST. (B) LSPR results of (a) unfunctionalized and (b) functionalized nanosandwich arrays with thiol terminated polymer at below LCST ( $25^\circ\text{C}$ ) and (c) above LCST ( $45^\circ\text{C}$ ). (C) SPR sensogram of the adsorption and temperature-responsive behaviour of polymer. .... 78

Figure 3.15 The hot water injection on gold substrate as control experiment. .... 79

Figure 3.16 (A) Schematic illustration of mixed SAM functionalized nanosandwiches and streptavidin detection above the LCST. Tapping mode AFM images of (B) Unfunctionalized and (C) 0.1mM 9:1 thiol and terminated polymer/EZ-Link HPDP-Biotin. LSPR measurements of (D) (a) Unfunctionalized nanosandwiches, (b) Nanosandwiches after modification with 0.1 mM 9:1 thiol terminated polymer / EZ-Link HPDP-Biotin, (c) Functionalized nanosandwich arrays after modification with SA ( $2\mu\text{M}$ ) (E) Unfunctionalized nanosandwiches, (b) Nanosandwiches after modification with 0.1 mM 9:1 thiol terminated polymer / EZ-Link HPDP-Biotin, (c) Nanosandwich arrays were obtained by coating 9:1 mixed SAM after heating above the LCST, and (d) Functionalized nanosandwich arrays after modification with SA ( $2\mu\text{M}$ ). .... 82

Figure 3.17 Bioaffinity binding between streptavidin and mixed SAM (polymer+EZ-Link) below and above LCST. (a) DI water injection below LCST, (b) mixed SAM (polymer: EZ-Link, 9:1) injection, (c) SA injection and (d) DI water injection above LCST. Flow rates were, respectively, 100 $\mu\text{L}/\text{min}$ , 20 $\mu\text{L}/\text{min}$ , 20 $\mu\text{L}/\text{min}$ and 100 $\mu\text{L}/\text{min}$ .....	84
Figure 3.18 (A) SEM image of GNRs. (B) Tapping mode AFM image of GNRs. (C) UV-Vis spectra of GNRs prepared with different aspect ratio. ....	86
Figure 3.19 (A) UV-Vis spectrum of GNRs after treatment with $\text{N}_2$ gas. (B) SEM image of GNRs after treatment with $\text{N}_2$ gas. (C) Enlarged image of (B).....	87
Figure 3.20 (A) UV-Vis spectra of GNRs treated by $\text{N}_2$ gas. (B) SERS spectra of the same samples A red and blue. (C) SEM image of the nanoparticles and nanorods corresponding to red curve. (D) SEM image of nanoparticles corresponding to blue curve.....	89
Figure 3.21 (A) UV-Vis spectra of GNPs according to single step synthesis prepared under low and high pressure Ar. (B) SEM image of particles under low pressure. (C) Enlarged image of (B).....	91
Figure 3.22 (A) UV-Vis spectrum of semi-shells, seed solution was prepared under $\text{N}_2$ . (B) SERS spectrum of semi-shell. (C) SEM image of face off semi-shells, (D and E) low and high magnification of face up nanoshell. (F) Model of the semi-shell....	93
Figure 3.23 Control experiments for gas treatment. ....	95
Figure 3.24 (A) UV-Vis spectrum of gold nanobubbles, seed solution was prepared under $\text{N}_2$ gas. (B-D) SEM images of nanobubbles.....	97
Figure 3.25 (A) LSPR spectra of (a) unfunctionalized and (b) functionalized GNRs. (B) SEM image of functionalized GNRs. ....	98
Figure 3.26 (A) Schematic illustration of the binding event of (a) mixed SAM (DT+Ez-Link biotin) , (b) streptavidin (SA) and (c) mixed SAM functionalized GNRs on nanodot arrays. (B) LSPR spectra of the modified nanodot arrays with functionalized GNRs. (C) SEM and (D) AFM images of the modified nanodot arrays with functionalized GNRs.....	100

## NANOSTRUCTURES FOR PLASMONIC BIOSENSORS

### ABSTRACT

This thesis aims to show that nanoparticles in the form of triangle nanostructures/nanosandwiches prepared using natural lithography or in the form of nanorods/nanobubbles prepared by wet chemistry have important optical properties and that the enhanced sensitivity of their surrounding environment can be used as a new class of optical sensors using Localized Surface Plasmon Resonance (LSPR) spectroscopy and Surface Enhanced Raman Scattering (SERS). The content of the thesis can be divided into two main parts: (1) the preparation, characterization and optimization of nanostructures/nanosandwiches for the basic understanding of their optical properties and the development and testing of nanosandwiches as model biosensors; (2) synthesis of gold nanorods and changing the growth process using various gases to produce nanoparticles and nanobubbles. These nanostructures have been also investigated with LSPR/SERS for optical properties and also using microscopies techniques for visualization.

In the first part of the thesis, Nanosphere Lithography (NSL) technique was used to produce patterned arrays of sandwich-like nanostructures. The nanosandwiches were made of triple layers of metal / metal oxide (insulator) / metal (MIM). These new nanosandwich arrays were then functionalized with different model biomolecule species (e.g. streptavidin, single strand adenine oligonucleotide) and temperature-responsive polymer actuators. To the best of our knowledge, these kinds of temperature-responsive nanosandwich arrays functionalized with multiple biorecognition species have not been developed before by any other group. To investigate different transduction mechanisms, the LSPR and SERS of the functionalised nanoarrays were determined as a function of multiple biomolecular binding events using an Ultraviolet Visible Near-Infrared (UV-VIS-NIR) spectrophotometry, Atomic Force Microscopy (AFM), and Scanning Electron Microscopy (SEM).

The second part of the thesis was to develop new synthetic methods for preparation of plasmonically active nanoparticles (NPs) such as nanorods (NRs) and nanobubbles, and to characterize the resulting products. The gold nanorods were bound to nanodots. This system may contribute to future plasmonic devices.



## PLASMONİK BİYOSENSÖRLER İÇİN NANOYAPILAR

### ÖZET

Bu tez, doğal litografi kullanılarak hazırlanmış üçgen nanoyapılar/nanosandviçler veya ıslak kimyayla hazırlanmış nanoçubuklar/nanobaloncuklar şeklindeki nanopartiküllerin önemli optik özellikleri olduğunu ve bunları çevreleyen ortamın geliştirilmiş hassasiyetinin Lokalize Yüzey Plasmon Rezonans (LSPR) ve Yüzey Geliştirilmiş Raman Saçılımı (SERS) teknikleri aracılığıyla optik sensörlerin bir yeni sınıfı olarak kullanabileceğini göstermeyi amaçlar.

Tezin içeriği 2 ana kısma bölünmüştür: (1) nanoyapılar/nanosandviçlerin, optik özelliklerini anlamak ve model biyosensörler olarak geliştirmek ve test etmek için, hazırlanması, karakterizasyonu ve optimizasyonu; (2) altın nanoçubukların sentezi ve nanopartikül ve nanobaloncuk üretimi için çeşitli gazlar kullanarak büyütme işleminin değiştirilmesi. Ayrıca bu nanoyapılar, optik özellikleri için LSPR/SERS ile ve görüntüleme için mikroskop teknikleriyle incelenmiştir.

Tezin ilk kısmında, Nanoküre Litografi (NSL) tekniği sandviç gibi nanoyapıların desenli dizilerini üretmek için kullanılmıştır. Nanosandviçler üçtabakalı metal/metal oksit (yalıtkan)/metalden yapılmıştır. Bu yeni nanosandviç dizileri sıcaklığa duyarlı polimer uyarıcılar ve farklı model biyomolekül türleriyle (örn: streptavidin, tek-şerit adenin oligonükleotidi) fonksiyonelleştirilmiştir. Bilindiği kadarıyla, çoklu biyotanıma özelliğine sahip sıcaklığa duyarlı nanosandviç dizileri herhangi bir başka grup tarafından daha önce geliştirilmemiştir. Farklı transdüksiyon mekanizmalarını araştırmak için, fonksiyonelleştirilmiş nanodizilerin Lokalize Yüzey Plasmon Rezonans ve Yüzey Geliştirilmiş Raman Saçılımı, Ultraviyole-Görünür -Yakın Kızılötesi Spektrofotometresi (UV-Vis-NIR), Atomik Kuvvet Mikroskobu (AFM) ve Taramalı Elektron Mikroskobu (SEM) kullanarak çoklu biyomoleküler bağlanma olaylarının fonksiyonu olarak belirlenmiştir.

Tezin ikinci kısmı nanoçubuklar ve nanobaloncuklar gibi plasmonik olarak aktif nanopartikülleri hazırlamak için yeni sentetik metotları geliştirmek ve sonuçta oluşan ürünleri karakterize etmektir. Altın nanoçubuklar nanonoktalara bağlanmıştır. Bu sistem gelecek plasmonik cihazlara katkı sağlayabilir.

## **1 INTRODUCTION**

This thesis focuses on preparation of nanosandwiches arrays functionalized with different model biomolecules and temperature-responsive polymers for potential biosensor applications via Localized Surface Plasmon Resonance (LSPR) Spectroscopy and Surface Enhanced Raman Scattering (SERS). It also develops synthetic methods for preparation of nanorods (NRs) and their conversion to nanoparticles (NPs) and nanobubbles. Accordingly, the first chapter gives introductory information on biosensors, LSPR, SERS, nanolithographic techniques and NRs. Chapter 2 describes the experimental methods used in the thesis. Chapter 3 gives the results of the experiments performed throughout the thesis and their discussions.

### **1.1 What is a Biosensor?**

Biosensors are devices that permit rapid analysis of matters. They are mostly applying for detection and monitoring of biological, chemical and toxic agents. Number of feature in nanomaterials make them suitable for sensor applications, these include, high surface area, high reactivity, easy dispersability and rapid fabrication. Biosensors technology are the growing fast, which combines biological, chemical, and physical sciences together with engineering for broad range of applications.<sup>2</sup> The biosensor term have a various meaning with respect to the research field. However, biosensor describes as a combination of views.<sup>3</sup> The biosensor term first introduced in the late 1970s.<sup>4</sup> But the first “biosensor” was discovered by Clark in 1956<sup>5</sup> who is well known inventor of Clark electrode. Then these issues were investigated and improved by Clark and Lyons in 1962<sup>6</sup> as enzyme electrode. Then the work was expanded to developed functional enzyme electrodes for glucose by Updike and

Hicks.<sup>7</sup> Guilbault and Montalvo<sup>8</sup> were detailed a urea sensor based on a potentiometric enzyme electrode.

Clark's ideas commercialized in 1975 on glucose analyser based on the amperometric detection of hydrogen peroxide and supported by Yellow Springs Instrument Company (Ohio). This was the first of biosensor-based analyser device to be built by companies around the world. The biosensors which have thermal transducers was introduced in 1974, together with the thermal enzyme probes<sup>9</sup> and enzyme thermistors<sup>10</sup>. According to Divis study, microbial electrodes was used for the measurement of alcohol with help of bacteria. A fibre-optic sensor, which term is optode have excellent performance for in vivo measurement to develop optical biosensor. The carbon dioxide or oxygen based sensors were invented by Lubbers and Opitz<sup>11</sup> in 1975. Shichiri et al.<sup>12</sup> was introduced the in vivo application of glucose biosensors in 1982. The piezoelectric or potentiometric transducer had been investigated since the early 70's. Liedberg et al.<sup>13</sup> described the use of surface plasmon resonance to monitor affinity reactions in real time. The BIAcore is one of strong compant based on surface plasmon resonance technology which launched in 1990.

The research in biosensors have progressed for many years and huge number of publication reported in literature. Histogram in Figure 1.1 illustrate the research on biosensors field and clearly shows the popularity of field in last 10 years.

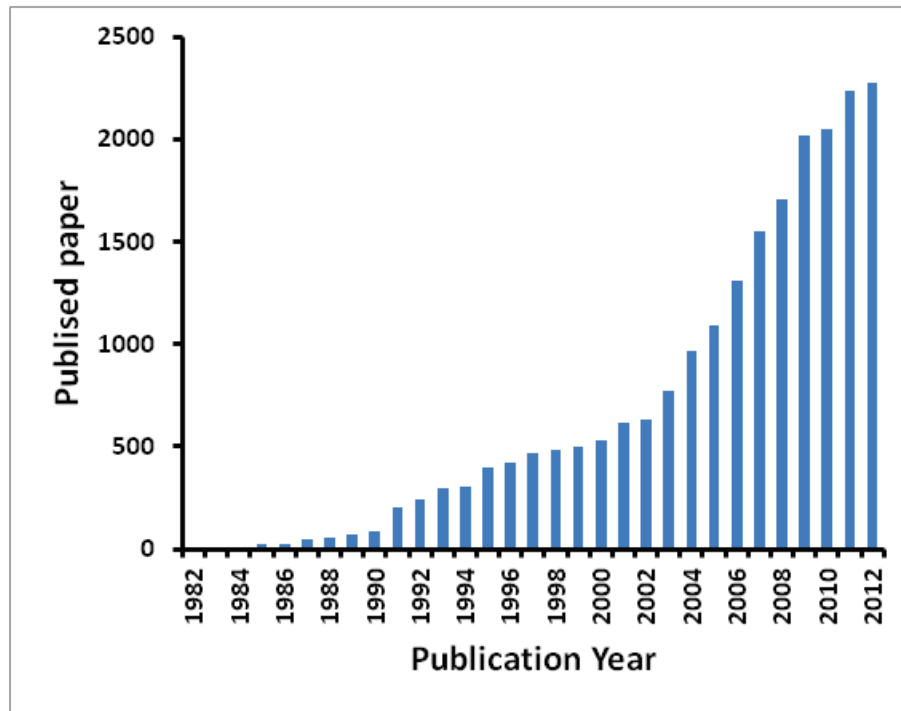


**Figure 1.1** Demonstrate publications versus number of the paper in biosensor field.<sup>1</sup>

### 1.1.1 The principle of Biorecognition system

A biosensor is composed of two parts, a bioreceptor and a transducer. The bioreceptor means a biomolecule that recognizes the target. The transducer converts the biorecognition event into a signal by measuring the changes in the reaction. A biosensor occurred that two components are combined in one single sensor. This combination measures the analyte without any reagents and specialized laboratory skills.<sup>14</sup>

The biosensor working principle is based on selective biorecognition and can be defined as conversion of chemical information to electrical information. This system involves the following procedure (Figure 1.2). Analyte diffuses from bulk solution to the bioreceptor immobilized sensor and react selectively and efficiently with the bioreceptor. This reaction leads to a change in optical, electronic properties or etc. depending on the transducer model. The change in biosensor surface is converted into electrical signal, which is amplified, processed and displayed by transducer.

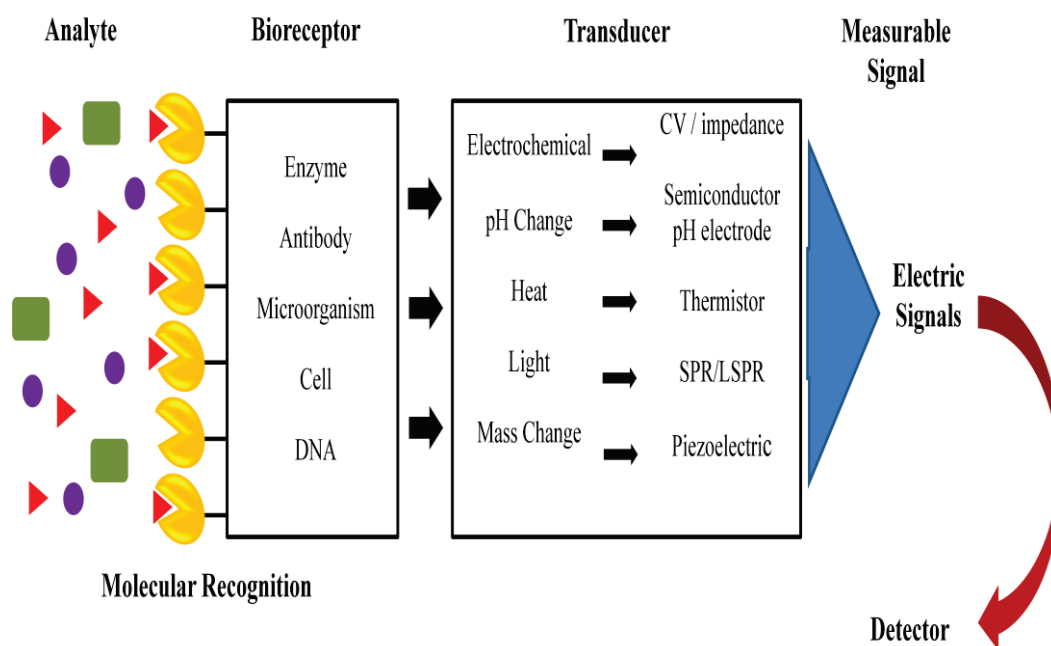


**Figure 1.2** Schematic representation of biosensor.

In general term, components of biosensor can be described as; Bioreceptor: Enzymes, antibodies, cell receptor, nucleic acid, tissue etc. can be used as a bioreceptor and selectively recognizes the analyte which is target molecule for receptor. Transducer: Interaction between analyte and bioreceptor produces a physical change close to the transducer surface. Various transducers such as an electrochemical, calorimetric, optical, piezoelectric are available in literature.<sup>14a</sup>

### 1.1.2 Types of Biosensors

Biosensors is classified according to working principle of transducer and demonstrate as follow: <sup>15</sup>

#### 1.1.2.1 Electrochemical Biosensors

Electrochemical biosensors are the most used to a large extent. The first idea about biosensor introduced by Clark and Lyons based on enzyme electrode. Yellow Springs Instrument Company produced Clark 's work as the first glucose biosensor

in 1975.<sup>16</sup> Then, owing to high sensitivity, selectivity, ability, many kind of electrochemical biosensors have been improved.

#### **1.1.2.2 Calorimetric Biosensors**

Calorimetric biosensors probe the amount of change in heat during a biochemical reaction.<sup>17</sup> In general, thermistor is used to find out the modification of temperature in the solution. The recorded peak height is proportional to the enthalpy change with respect to a substrate concentration.

#### **1.1.2.3 Optical Biosensors**

This detection method is based on the changes in absorbance, fluorescence, luminescence, reflectance, light scattering, or refractive index. In addition to these detections method, the two most use protocols are fluorescence - based detection and label - free detection.<sup>18</sup> Optical biosensors have been used in healthcare, biomedical research, environmental monitoring, homeland security, and the military<sup>19</sup>.

#### **1.1.2.4 Piezoelectric Biosensors**

A piezoelectric biosensor is an analytical device, which uses the piezoelectric effect to probe pressure, acceleration, strain or force by converting them to an electrical charge. The working principle is based on to measurement of the mass changes on a piezoelectric crystal. Piezoelectricity is described as an materials that generate mechanical movement in response to electric potential.<sup>20</sup>

### **1.1.3 Biosensor Characteristics**

Biosensors are qualified with following parameters:<sup>14a</sup>

1. *Sensitivity* is response of the sensor to analyte concentration's per unit change
2. *Selectivity* is the ability of the sensor to respond only to the target analyte.

3. *Range* is the concentration range over which is working interval of sensor. Sometimes it is called as dynamic range or linearity.
4. *Response time* is the time requirement to indicate most of the sensor final response in analyte concentration.
5. *Reproducibility* is the accuracy of the sensor's obtained result.
6. *Detection limit* is the lowest concentration of the analyte for a measurable response (approximately in this study is  $10^{-5}$  M).
7. *Life time* is the time period of the sensor, which is used without significant deterioration in performance characteristics.
8. *Stability* defines the change in its baseline or sensitivity over a fixed period of time

In addition to these parameters, a biosensor should be cheap, small and portable. Furthermore, biosensors should be biocompatible, nontoxic, nonantigenic and stable under ambient conditions.<sup>15</sup>

The major key points in improvement of biosensor design involve a proper bioreceptor or a recognition molecule, suitable immobilization method, transducer to convert binding reaction into measurable signal, measurement range, linearity, enhancement and sensitivity are crucial factors to design a biosensor. And finally packaging of the biosensor into a complete device. From all the selections mentioned above, one needs information about biochemistry, biology, chemistry and physics, and finally needs knowledge of kinetics and mass transfer.<sup>14a</sup>

#### **1.1.4 Applications of Biosensor**

Biosensors have various applications ranging from detection of industrial toxins and food contamination, medical diagnostics, military etc. For instance, in agriculture and food industry, viral,<sup>21</sup> fungal<sup>22</sup> and bacterial diseases<sup>23</sup> detection. The amount of sugar monitored in soft drink detected by Barrodo et al.<sup>24</sup> . Mascini et al. designed a biosensor to determine the freshness of meat.<sup>25</sup> There are many studies in literature about environment monitoring.<sup>26</sup> The pollution level in the environment including air,<sup>27</sup> land<sup>28</sup> and water<sup>29</sup> monitored. By the way, the quality of water

through tests for pollutants,<sup>30</sup> chemical residues,<sup>31</sup> pesticides,<sup>32</sup> herbicides,<sup>33</sup> toxins<sup>34</sup> and microbes<sup>35</sup> examined in water reservoirs.

In fermentation industry, biosensor used for monitoring the cultured micro-organisms products such as drugs, hormones, vaccines, single cell proteins etc.<sup>21, 36</sup> Recently, the biosensors have been popular in military and defense industry.<sup>37</sup> Detection of toxic gases<sup>38</sup> and chemical warfare, such as mustard<sup>39</sup> and nerve gas<sup>40</sup> analyzed with portable biosensor.

### **1.1.5 Literature Review**

Recently, great numbers of research have been reported on optical biosensor for detection of biological molecules. Fan et al.<sup>18a</sup> illustrated label-free optical detection together with a number of detection methods such as RI, optical absorption, and Raman spectroscopic detection. Shin et al. demonstrated a novel concept in which enzyme-catalyzed precipitation was introduced on gold nanodots after immuno-reaction of antigen and its antibody to enhanced sensitive detection based on optical sensor or LSPR.<sup>41</sup> Lee group illustrated notable nanostructures for plasmonic sensing and explained relative physical models for nano-scale biosensor.<sup>42</sup> Van Duyne et al. showed the gold nanoparticles conjugated antibodies to provide LSPR enhancement.<sup>43</sup>



## 1.2 Introduction to Localized Surface Plasmon Resonance (LSPR)

Nano-materials are an important and interesting field of research due to various properties such as optical, magnetic, catalytic, and mechanical, which is not found in them bulk form. These materials allow to the development of novel devices with exciting application that previously unavailable. Development of optical sensors as nanotechnology tool in the last two decades have been found with the great extend applications in biotechnology,<sup>44</sup> health care,<sup>45</sup> drug monitoring,<sup>46</sup> food allergens detection, environmental monitoring, bio/chemical war agents and security.<sup>47</sup> In this study, we will investigate two types of optical sensors namely Localized Surface Plasmon Resonance (LSPR) and Surface-Enhanced Raman Spectroscopy (SERS) for various nanostructure materials measurement.<sup>48</sup>

The scatter light from nanoparticles is an important research area today for a variety of applications. In health sciences nanoparticles are used for drug monitoring and delivery. They are also used in solar cells in energy sector. The sum of absorption and scattering of light in nanoparticles causes the loss in intensity of light which namely is extinction. The electric field of incident light with metallic nanoparticles creates oscillation from collective electron cloud. This oscillation is called dipole plasmon resonance of the nanoparticles.<sup>49</sup> Generally plasmons can be defined as collective oscillation of free electron density in regard to the positive ions at metal surface which play an important role in the optical properties of metallic nanoparticles. The formation of standing wave from oscillation on a nanoparticles is generally referred to a localized surface plasmon (LSP) while the oscillation in the form of propagating along an interface is called surface plasmon-polariton (SPP) see Figure 1.3<sup>50</sup>

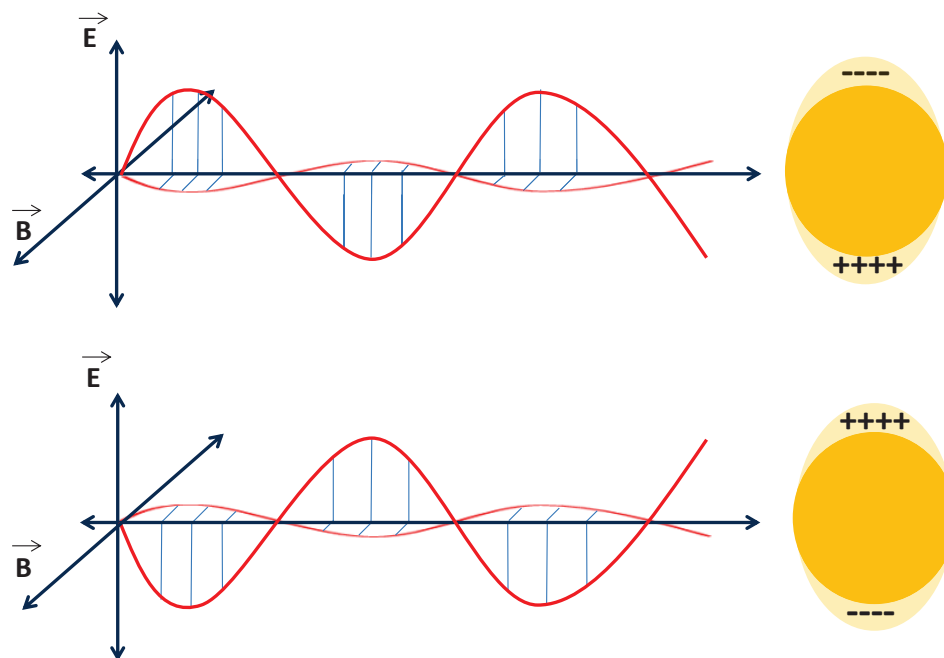


**Figure 1.3** Illustration of the plasmon oscillation in gold nanoparticles.

Optical sensors such as Surface Plasmon Resonance (SPR), LSPR and SERS have become popular bioassay techniques as they are convenient and label-free detection systems compared to conventional systems, which need to label with fluorescent dyes. Recently, LSPR spectroscopy progresses have made it excellent and sensitive tool, for detecting biological molecule interactions.<sup>51</sup>

### 1.2.1 Biosensor based on Localized Surface Plasmon Resonance

LSPR-based nanobiosensors are deliberated one of the most powerful techniques in the nano-biotechnology and biosensor areas. LSPR obtain the specific characteristics metalized nanostructured materials, such as highly esteemed metal nanoparticles, which can be excited by electromagnetic radiation with incident photons with the collective oscillations of conduction electrons at a specific wavelength. LSPR based biosensors has become popular for sensing due the advantages the technique provides such as high sensitivity of refractive index changes, label free detection, real-time measurements, reproducibility using nanostructures substrates, and low cost techniques. These advantages demonstrate

that nanobiosensors can be applied in a wide range of fields, such as medical, food safety, environmental monitoring, and drug screening.<sup>52</sup>

### 1.2.2 Theory behind Localized Surface Plasmon Resonance

The excitation of LSP by light results in localized electromagnetic field enhancement at resonance frequency. For a centuries wonderful color change in stained glass window that occur from strong absorption and scattering of light from noble metallic nanoparticles has attracted the interest of researchers around the world. This aimed the scientist deeply understand the relationship between the metallic particles with light, which can demonstrate the color changes in suspension is depend to the properties of materials such as composition, size, shape, and local dielectric environment. The optical characteristic of these noble nanoparticles can be applied as materials for SERS,<sup>53</sup> optical filters,<sup>54</sup> plasmonic devices,<sup>55</sup> and nanobiosensors.<sup>56</sup>

Metallic nanoparticles such as gold and silver exhibit a strong optical extinction at visible and near-infrared (NIR) wavelengths and generate LSPR phenomenon which is sensitive to the surrounding medium.<sup>57</sup> The intense and strong signals in all surface-enhanced spectroscopies are due to LSPR excitation with selective absorption wavelength. Which contains large molar extinction coefficients around  $3 \times 10^{11} \text{ M}^{-1} \text{ cm}^{-1}$ ,<sup>58</sup> (resonant Rayleigh scattering) resonant scattering<sup>59</sup> with high efficiency<sup>60</sup> and the enhanced local electromagnetic fields close the surface of metallic particles. The Mie theory approximation of the extinction of a metallic nanoparticles in the long wavelength is the convenient approach for modeling optical properties of the nanoparticles (Equation 1.1).<sup>61</sup>

$$E(\lambda) = \frac{24\pi N_A a^3 \varepsilon^{3/2}}{\lambda \cdot \ln(10)} \left[ \frac{\varepsilon_i}{(\varepsilon_r + \chi \varepsilon_m)^2 + \varepsilon_i^2} \right] \quad (1.1)$$

$E(\lambda)$  is the sum of the absorption and scattering,  $N_A$  and  $a$  is the areal density and radius of metallic nanoparticles, respectively,  $\varepsilon_m$  is the dielectric constant of the medium surrounding the metallic nanosphere,  $\lambda$  is the wavelength of the absorbing

radiation,  $\epsilon_i$  and  $\epsilon_r$  is the imaginary and real part of the nanoparticle's dielectric function, respectively, and  $\chi$  is the aspect ratio of the nanoparticle.<sup>61</sup>

It is clearly known that the LSPR spectrum of a separate metallic nanoparticle surrounded in an external dielectric medium will depend on the radius  $a$ , material ( $\epsilon_i$  and  $\epsilon_r$ ), and the environment's dielectric constant ( $\epsilon_m$ ) of the metallic nanoparticles. In addition, when the nanoparticles are not spherical, the extinction spectrum will depend on the nanoparticle's in-plane diameter, out-of-plane height, and shape ( $\chi$ ). The values for  $\chi$  increase from 2-17 with respect to aspect ratio of metallic nanoparticles. The samples were prepared in this study contain nanoparticles that are supported on a silicon substrate, therefore the LSPR results were depended on interparticle spacing and substrate dielectric constant.<sup>56e</sup>

In Equation 1.2 the location of the extinction maximum,  $\lambda_{max}$ , of gold and silver nanoparticles is highly dependent on the dielectric properties of the surrounding environment and that wavelength shifts in the extinction maximum of nanoparticles can be depend on the molecular conformation around them.<sup>51</sup> To obtain optical signals based on LSPR extinction shifts, there are different sensing mechanisms for metallic nanoparticles that provide the transduction of macromolecular. These mechanisms are: (1) resonant Rayleigh scattering from nanoparticle labels in a manner analogous to fluorescent dye labels,<sup>62</sup> (2) nanoparticle aggregation,<sup>63</sup> (3) surface charge of nanoparticle,<sup>64</sup> and (4) local refractive index changes.<sup>65</sup>

$$\Delta\lambda_{max} = m\Delta n \left[ 1 - \exp\left(\frac{-2d}{L}\right) \right] \quad (1.2)$$

Here  $m$  is the bulk refractive-index response of the nanoparticle(s);  $\Delta n$  is the change in refractive index induced by the adsorbate;  $d$  is the effective adsorbate layer thickness;  $L$  is the characteristic decay length of the local electromagnetic field surrounding the plasmonic nanostructures. This relationship is the basis of LSPR wavelength-shift sensing experiments. The effect of LSPR can thus be employed to monitor surface binding events.<sup>51, 66</sup>

The first LSPR as biosensing was reported by Englebienne et al., in 1998.<sup>67</sup> Englebienne investigated the changes in local refractive index by biomolecules adsorption near the nanoparticle surface using LSPR measurement. An ideal biosensor is the one that has sensitivity the target analyte. New methods are developed to increase the sensitivity of the biosensors which also increase the  $\lambda_{\max}$  shift from the same amount of analyte. The  $\lambda_{\max}$  shifts of LSPR are dependent on the metallic nanoparticle size and the sensitivity of the biomolecules conjugated particles. Mathematically  $\lambda_{\max}$  shifts of LSPR can be described in Equation 1.3 which showing the relationship between sensitivity, size morphology and composition of metallic nanoparticles.

$$\Delta\lambda_{max} = m\Delta n \quad (1.3)$$

Where  $n$  is the refractive index. The shift is also proportional to the adsorbate molecule mass.<sup>56a, 68</sup> Recently, various methods developed to probe or detect large shift from metallic nanoparticles and its conjugation with biomolecules.<sup>69</sup> Another way to increase the  $\lambda_{\max}$  shift is to use plasmonic labels using gold nanoparticles.<sup>70</sup>

### 1.2.3 Similarities between SPR and LSPR Sensors

SPR sensors, which are formed of copper, gold, or silver planar films, have been used to examine of analyte-surface binding interactions at or near a metal surface.<sup>56e</sup> The LSPR-based nanosensor is corresponding to that of flat surface, propagating SPR sensors. For approximately two decades, SPR sensors, with planar films such as copper, gold, or silver, have been used as refractive index based sensors to probe the kinetics and equilibrium binding constants for many biomolecule interactions including protein:protein, protein:DNA, and protein:vesicle interactions in real time with high sensitivity.<sup>71</sup>

Sensors based on SPR spectroscopy have many advantages such as: (1) adsorption processes can be monitored in real time with high sensitivity of  $10^{-1} - 10^3$  s time scale for measurement of binding kinetics,<sup>72</sup> (2) the method is surface sensitive and probe changes in refractive index within a hundreds nanometer of the

sensor surface, (3) Multiple detection modes such as angle shift, wavelength shift and imaging, (4) lateral spatial resolution on the order of 10  $\mu\text{m}$  for using the SPR imaging mode of detection,<sup>73</sup> (5) label free detection system, and (6) commercially available. Both SPR and LSPR are sensitive to refractive index changes.<sup>56e</sup>

The two main differences between the SPR and LSPR sensors are the refractive index sensitivities and the characteristic electromagnetic field decay lengths. The refractive index sensitivity of SPR sensors is large ( $\sim 2 \times 10^6 \text{ nm/RIU}$ )<sup>74</sup> in comparison to LSPR nanosensor ( $\sim 2 \times 10^2 \text{ nm/RIU}$ )<sup>64a</sup> This means the LSPR nanosensor would be 10,000 times less sensitive than the SPR sensor. But the characteristic electromagnetic field decay length,  $l_d$ , enhanced the LSPR nanosensor sensitivity.<sup>56a</sup> These results of LSPR nanosensors show that the decay length,  $l_d$ , is  $\sim 5\text{-}15 \text{ nm}$  or  $\sim 1\text{-}3\%$  of the light's wavelength depends on the nanostructures morphology and size. On the other hand, this value is  $200\text{-}300 \text{ nm}$  decay length or  $\sim 15\text{-}25\%$  of the light's wavelength for the SPR sensor.<sup>74</sup> The aforementioned parameters are present the differences between two system of SPR and LSPR.

Experimentally, SPR sensing requires at least an area of  $10 \mu\text{m} \times 10 \mu\text{m}$  spot size. This spot size for LSPR sensing, can be minimized to a large number of individual sensing elements, as an example  $1 \times 10^{10}$  nanoparticles for a  $2 \text{ mm}$  spot size with sphere size of  $400 \text{ nm}$  down to a single nanoparticle with an in-plane width of  $\sim 20 \text{ nm}$  using single nanoparticle techniques.<sup>62c</sup> The nanoparticle has capability of deliver the similar information as the SPR, because of that the pixel size can be minimized to the sub  $100 \text{ nm}$ . The other differences between two systems are temperature control. In LSPR, because of the lower refractive index sensitivity, the system no temperature control needed whereas the SPR sensor (with large refractive index sensitivity) requires temperature control. The major difference between the two systems of LSPR and SPR sensors is the cost. Considerably in planar SPR sensors, Equation 1.2 quantitatively shows an adsorbent's affect on the sensor. But the use of Equation 1.2 in LSPR measurements, show the response for adsorbate layers.<sup>56a</sup>

#### 1.2.4 Literature Review

Many researchers begun to investigate alternative strategies for the design and development of optical biosensors and chemosensors based on the optical properties of metal nanoparticles.<sup>63a, 64a, 65a</sup>

Label-free sensing technologies based on LSPR have used various types and shapes of metallic nano-structures for biosensor applications.<sup>62c, 75</sup> However, the sensitivity of detection by LSPR is lower for larger molecules than smaller molecules. This is due to penetration depth of LSP field from nanostructures to surrounding environment which is around 20-30 nm.<sup>76</sup> Numbers of papers have been published on the application of the LSPR technique in biotechnology. These publications are on the detection of streptavidin,<sup>70a</sup> anti-biotin,<sup>77</sup> concanavalin,<sup>78</sup> Alzheimer disease bio-markers,<sup>79</sup> and other bio-recognition events.<sup>80</sup> Other applications of LSPR are on chemical detection of molecules in liquid phase such as organophosphorous pesticides,<sup>81</sup> hydrogen peroxide<sup>82</sup> and ammonia<sup>83</sup>. The LSPR is capable to probe gases molecules including octane, pentanol, by using noble nanoparticles.<sup>84</sup>

Beside biological application of LSPR many researchers have investigated on performance of LSPR on the substrate dielectric. Van Duyne et al. have investigated and demonstrate that the metallic nanoparticles show structural changes when exposed to different solvents which effect the LSPR extinction peak.<sup>85</sup> The comparison effect of metallic substrate, semiconductors and dielectric on nanoparticle optical properties with particle positioned at various heights relative to the substrate surface have illustrated by Pinchuk and co-workers.<sup>86</sup> These both investigations of Van Duyne and Kreibig demonstrated that plasmon resonances are red-shifted due to interactions with the substrate and amount of the red-shift that determined by the dielectric constant of the substrate and also by the inter particles distance. In another study Hanarp et al. reported that the extinction peak in LSPR as function of refractive index is more shifted when the disk like particles was larger or the aspect ratio increased.<sup>87</sup>

Van Duyne and co-workers were one of the first groups to investigate biological sensors based on metal nanoparticles using LSPR and SERS. Van Duyne and Amanda J. Haes studied that the triangular silver nanoparticles fabricated by natural lithography<sup>88</sup> with highly sensitivity are the best candidate for selective nanoscale affinity biosensors. It will be illustrated that these biosensors based on localized surface plasmon function in a way totally similar to their SPR counterparts by converting small changes in refractive index near the noble metal surface into a measurable wavelength shift response. The biotin-streptavidin system with its acutely high binding affinity is an excellent example for biosensors based on LSPR.<sup>70a</sup>

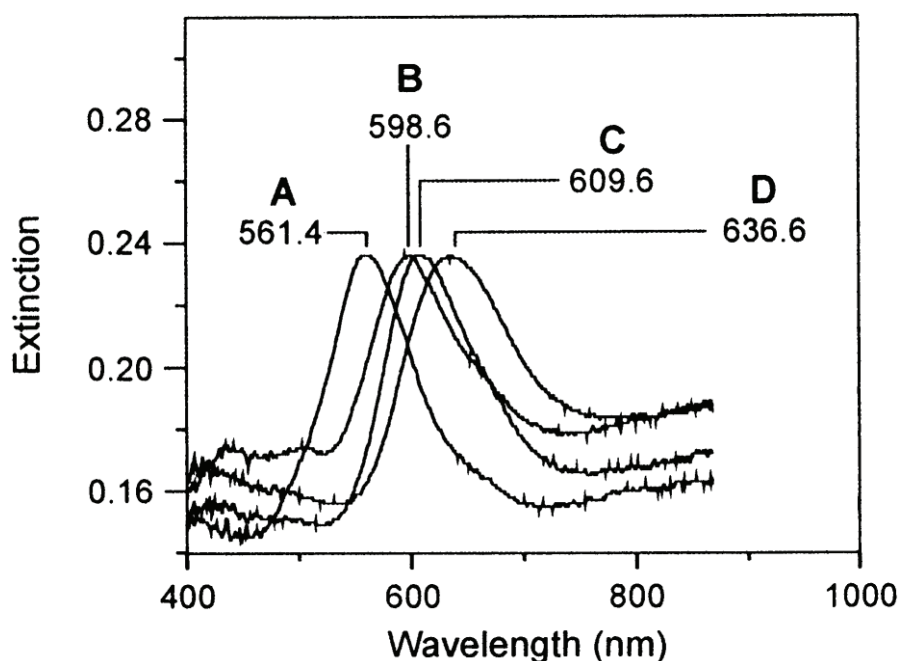


**Figure 1.4** LSPR spectra of each step in the surface modification of NSLderived Ag nanoparticles to form a biotinylated Ag nanobiosensor and the specific binding of SA. (A) Ag nanoparticles before chemical modification,  $\lambda_{max}$  = 561.4 nm. (B) Ag nanoparticles after modification with 1 mM 1:3 11-MUA/1-OT,  $\lambda_{max}$  = 598.6 nm. (C) Ag nanoparticles after modification with 1 mM biotin,  $\lambda_{max}$  = 609.6 nm. (D) Ag nanoparticles after modification with 100 nM SA,  $\lambda_{max}$  = 636.6 nm. All extinction measurements were collected in a  $N_2$  environment.<sup>70a</sup>

Van Duyne group also showed that the silver nanoparticles that are coated by  $Al_2O_3$  using atomic layer deposition can probe the long and short-range LSPR distances of silver nanoparticles.<sup>68b</sup> Another study of Van Duyne group also investigated the influence of a dielectric substrate on the LSPR extinction of silver



nanoparticles, particularly a nanocube.<sup>89</sup> Van duyne group also illustrated the plasmonic properties of nanowell structures with thin Ag overlayer. The effect of internanowell distance, mass thickness, nanowell depth and the dielectric environment have been investigated by LSPR measurement in more detail.<sup>90</sup>

Zhou and colleagues demonstrated the array of nanoholes fabricated on glass substrate using natural lithography. The LSPR sensitivity of nanoholes to local refractive index is measured and probed the bovine serum albumin (BSA) binding and biotin-streptavidin to gold nanoholes.<sup>91</sup>

Not only noble-metallic nanoparticles but also compositions of noble-metal–dielectric nanostructures play an importance role for the development of functional materials, such as optoelectronic devices or biomedical sensors. Their singularity properties and functionality rely on LSPR. Dmitriev et al. illustrated the design and properties of metal – oxide nanosandwiches on solid support. These nanosandwiches composed of three layers- two noble metal (gold) that are separated by oxide ( $\text{SiO}_2$ ) or dielectric spacer. The optical properties of these nanostructures detected by LSPR and elucidated by electrodynamic simulations based on the dispersive finite-difference time-domain method (D-FDTD).<sup>92</sup>

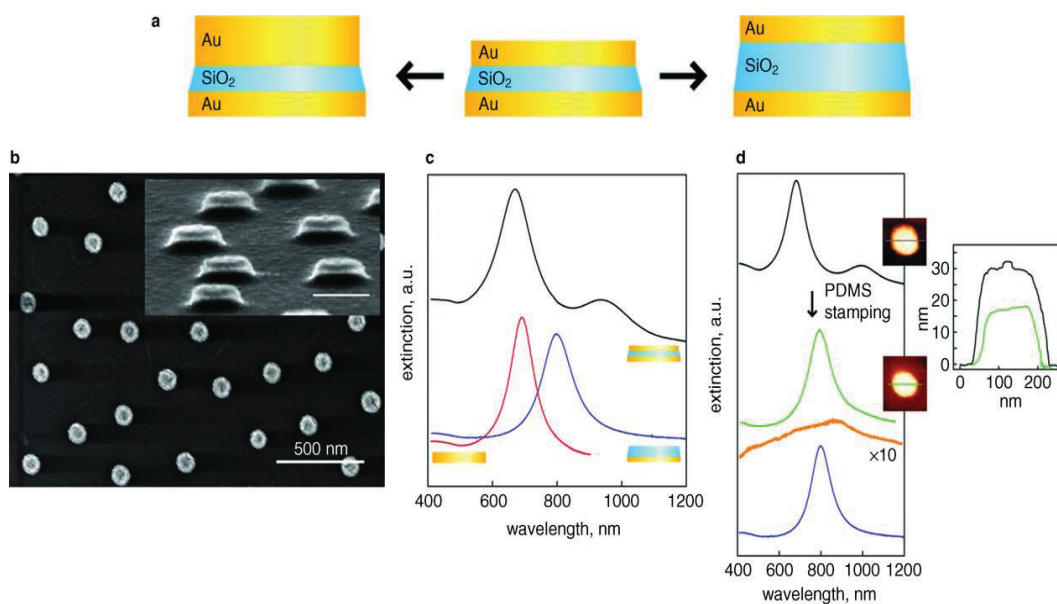


**Figure 1.5** (A) The disk-shaped nanosandwich is composed of stacked Au, SiO<sub>2</sub> and Au layers, each typically 10 nm thick. The electromagnetic coupling between the fundamental plasmon modes of the upper and lower Au disks can be fine-tuned by either changing the aspect ratio of one of the nanodisks (left) or by varying the thickness of the dielectric spacer layer (right). (B) SEM image of a sandwich array. The diameter of the lower disk is 110 nm and the inset shows a side view of the structure. (C) extinction spectrum from the nanosandwich (D) Mechanical splitting of the coupled plasmonic system, monitored by extinction spectroscopy and AFM profiling.<sup>92</sup>

In the report by Hatsuzawa et al., LSPR-based optical enzyme biosensor fabricated using stimuli-responsive hydrogel conjugate silver nanoparticles.<sup>93</sup> Lu and colleagues demonstrate that for enhancement of the volatile organic compounds (VOCs) to increase selectivity and sensitivity of LSPR sensors with surface modification using self-assemble techniques.<sup>84d</sup> They illustrate also the responses of the LSPR spectrum of unmodified, benzene thiol, 3-mercaptopropanoic acid (MPA) and 4-pyridine thiol conjugate silver nanoparticles and compared with those of not organic functional groups. The thiolated self-assembled monolayers (SAM), refractive index and affinity of functional group are examined. An article have been published by Ma et al. to demonstrate the silver triangle nanoprisms array function as vapor sensors using LSPR measurement.<sup>94</sup> They investigated the differences between ethanol and four other vapors (acetone, benzene, propanol and hexane). Felidj group addressed the optical properties of hybrid based stimuli-responsive brushes grafted as plasmonic device that can detected using LSPR.<sup>95</sup>

### 1.3 Introduction to Surface Enhanced Raman Scattering (SERS)

There is nowadays a general consensus that the huge intensification of the Raman signal observed in SERS is mainly originated by the giant electromagnetic enhancement induced by LSPR of nanometric noble metal particles or clusters.<sup>96</sup> Due to its unique capabilities, SERS has been widely used to study the adsorption of many organic molecules on some metal colloids, mainly Ag, Cu, and Au. Its high sensitivity allows an accurate structural study of many molecules at very low bulk concentrations. This property has been used to obtain very detailed information of adsorbates such as the mechanism and geometry of the adsorption or which functional groups are in close contact with the metal.<sup>97</sup>

SERS is mainly originated by the huge electromagnetic enhancement produced by LSPR of noble metallic nanoparticles. Surface-Enhanced Raman Scattering or spectroscopy is a surface-sensitive technique that extends Raman spectroscopy by decreasing its detection limit to molecular monolayer or even a single molecule on rough metal surfaces. In 1974, when researcher tried to do Raman on the electrode they accidentally discovered the surface enhanced Raman scattering. Due to its unique capabilities, SERS has been widely used to investigate the adsorption of many organic molecules on some metal nanoparticles, mainly Ag, Cu, and Au. SERS is an attractive tool for applications such as surface catalyzed reactions, biomolecule and cell characterization. The difficulties of development of plasmonic materials at large area which shows both a high enhancement factor and reproducibility of the signal lead to limitation broad uses of SERS.<sup>98</sup>

#### 1.3.1 Raman scattering: definition

Raman scattering is a powerful light scattering technique used to identify the internal structure of molecules and crystals by interaction of laser light with a known frequency and polarization to electron cloud of the bond molecules in the sample.<sup>57a</sup> When the electron cannot travel from ground state to the lowest electronic excited state due to low energy of laser light, they move to intermediate state. The electron cannot stay long in the intermediate state and will immediately go back to the ground

state than the wavelength of the scattering light is the same as light source. This scattered light is called Rayleigh scattering. Raman effect exist, when a small fraction of the light which scattered at frequencies different from the frequency of the incident photons. Raman scattering can occur with the changes in vibrational, rotational or electronic energy of a molecule. This differences of photons energy is equal to the energy among vibration levels of the scattering molecules.<sup>57b</sup>

Raman scattering happens when the polarizability changes and depends on how tightly the electrons bound to nuclei. This binding in symmetric stretch is different between the minimum and maximum internuclear distances. The changes in polarizability during vibration led the scatters Raman light. The electrons in the asymmetric stretch are more easily polarized in the bond that expands but they can less polarized in the compresses bond.<sup>63a</sup> The vibrational energy depends on molecular structure and environment. Some factors such as atomic mass, bond order, molecular substituents, molecular geometry and hydrogen bonding all affect the vibrational energy. Therefore, vibrational Raman spectroscopy is not limited to intramolecular vibrations. Crystal lattice vibrations and other motions of extended solids are Raman-active.<sup>57b</sup>

### **1.3.2 Stokes and anti-Stokes scattering**

Raman scattering can be divided in two types. When the emitted energy is less than the incident photon, the process is called Stokes scattering. The opposite is called the anti-Stokes scattering.<sup>51</sup> This is illustrated in the Figure 1.6.

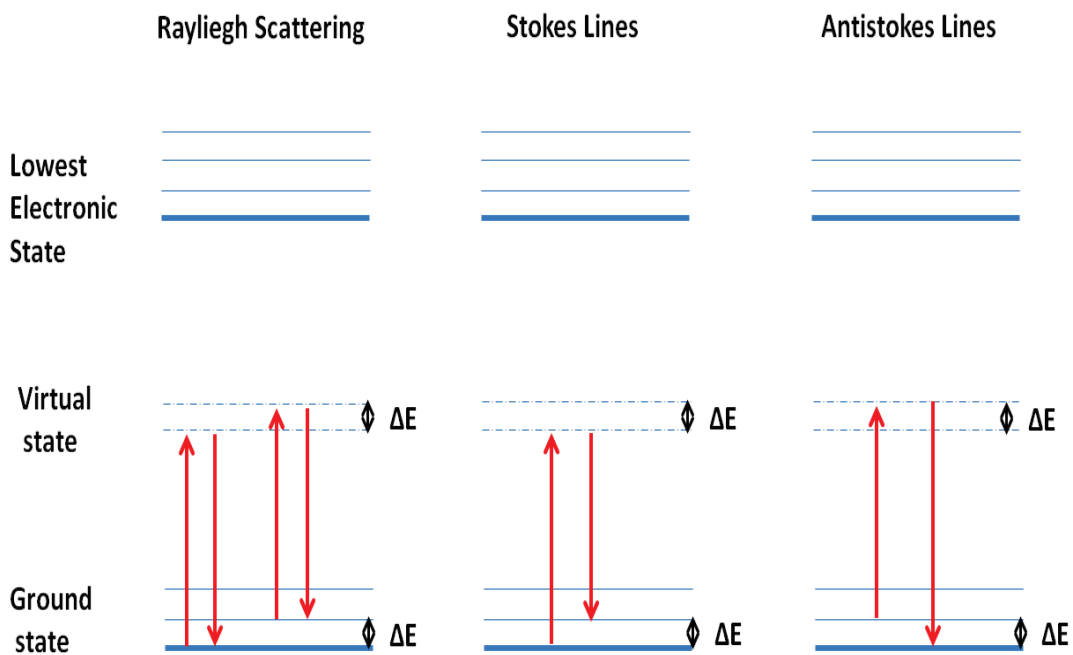


**Figure 1.6** Different scattering mode of quantum.<sup>51</sup>

The energy difference between the incident and scattered photons is represented by the arrows of different lengths. Mathematically,  $\nu$  or Raman shift in wavenumbers ( $\text{cm}^{-1}$ ), is calculated according to the following Equation 1.4:

$$\nu = \frac{1}{\lambda_{\text{incident}}} + \frac{1}{\lambda_{\text{scattered}}} \quad (1.4)$$

in which  $\lambda_{\text{incident}}$  and  $\lambda_{\text{scattered}}$  are the wavelengths of the incident and Raman scattered photons, respectively.<sup>57b</sup>

The Raman scattering suggests that the red-shifted (Stokes component) and blue-shifted re-radiation (anti-Stokes component) are equal. Experimentally, the Stokes component is often observed alone and only when the molecular vibrational frequency is small a weaker anti-Stokes component can be observed. This reveals that we have to be more careful with the theoretical description. When the molecule is in its vibrational ground state, it is incapable of parting the vibrational energy quanta to the anti-Stokes re-radiation. Consequently, the anti-Stokes component can only occur when the molecules are already in an elevated vibrational energy state.

Thus, the scattered intensity of the Stokes component is expected to be proportional to the ground-state population and the intensity of the anti-Stokes component to the population of the excited state.<sup>51, 63b</sup>

### **1.3.3 Raman signal enhancement**

One of the disadvantages of Raman spectroscopy is its low sensitivity as a tool in surface sciences. SERS is a surface sensitive technique that enhances Raman scattering of molecules adsorbed on rough metal surfaces. The mechanism of the enhancement effect of SERS is still not clear. There are two hypotheses on SERS functionality. The electromagnetic hypothesis which relies upon the excitation of localized surface plasmons. The second one is chemical rationalizes the effect through the formation of charge-transfer complexes. The second hypothesis can only be applied for molecules bond to the surface.<sup>51</sup>

### **1.3.4 Electromagnetic theory**

When the intensity of Raman signal of adsorbate increases an electric field enhancement produced. The strikes incident light on the surface can excite localized surface plasmons. The field enhancement is greatest when the plasmon frequency is in resonance with the radiation. The scattering occur, when the plasmon oscillations are perpendicular to the surface and if they are in-plane with the surface, no scattering will occur. For this reason roughened surfaces such as nanoparticles arrangement or pattern are typically employed in SERS experiments. These surfaces can provide an area on which the localized collective oscillations can take place.<sup>99</sup> Both the incident laser light and the Raman signal are close to resonance with the plasmon frequency if the Raman signal slightly shifted from the incident light. If the frequency shift is large, both the incident laser light and the Raman signal are not on resonance with the plasmon frequency, so the enhancement for both stage are not high.<sup>100</sup>

The surface metal is crucial for plasmon resonance frequency. Noble metals are chosen for SERS experiments because their plasmon resonance frequencies fall

within visible and near-infrared radiation (NIR) and to achieve maximum enhancement.<sup>51, 101</sup>

### 1.3.5 Chemical theory

While the electromagnetic theory of enhancement can be applied regardless of the molecule being studied, it does not fully explain the magnitude of the enhancement observed in many systems. Many molecules with a single pair of electrons that bind to the surface, have many different mechanism of enhancement, which does not involve surface plasmons. This chemical mechanism involves charge transfer between the chemisorbed species and the metal surface.<sup>102</sup> New electronic states which arise from chemisorption act as intermediate states in Raman scattering. Consequently, charge transfer excitations can happen at a lower energy state compared to the intramolecular excitations of the adsorbate. It is not uncommon that the highest occupied and lowest unoccupied molecular orbital of the adsorbate are symmetrically disposed in energy with respect to the Fermi level of the metal and lead to excitation energy reach to half.<sup>51</sup>

### 1.3.6 SERS spectrum

SERS provides the same information as traditional Raman spectroscopy with a greatly enhanced signal. The only differences in SERS spectra and traditional Raman is the number of modes. The modes observed in any spectroscopic experiment are carried out by the symmetry of the molecules and are usually summarized by selection rules. When molecules are bond to a surface, the symmetry of the system can change and lose the centre of symmetry. This loss eliminates the requirements of the mutual exclusion rule, which dictates that modes can only be either Raman or infrared active. Modes appear in both the infrared spectrum and SERS spectrum.<sup>99</sup> The orientation of adsorption to the surface can also be obtained from the SERS spectrum.<sup>51, 103</sup>

### 1.3.7 Enhancement factor (EF)

In SERS spectrum, the increase in signal is due to an increase in the apparent cross-section of the molecules adsorbed on the surface. This leads to the concept of the SERS enhancement factor (EF).

The most widely used definition for the average SERS EF is:

$$EF = \frac{I_{SERS}/N_{surf}}{I_{RS}/N_{vol}} \quad (1.5)$$

$N_{Vol}$  is the average number of molecules in the scattering volume (V) for the Raman (non-SERS) measurement,  $N_{surf}$  is the number of molecules contributing to the SERS signal,  $I_{SERS}$  and  $I_{RS}$  are the intensities of the scattering band of interest in the SERS and normal Raman scattering spectra, respectively.

A more rigorous formula was found:

$$EF = \frac{I_{SERS}/(\mu_M \mu_S A_M)}{I_{RS}/(C_{RS} H_{eff})} \quad (1.6)$$

where  $I_{RS}$  is the intensity of the Raman signal,  $I_{SERS}$  is the intensity of the Raman signal under sers conditions,  $C_{RS}$  [M] is the concentration of the solution used for the non sers measurement,  $H_{eff}$  [m] is the effective height of the scattering volume,  $\mu_M$  [m<sup>-2</sup>] is the surface density of the individual nanostructures producing the enhancement,  $\mu_S$  [m<sup>-2</sup>] is the surface density of molecules on the metal and  $A_M$  [m<sup>2</sup>] represent the surface area of the metallic nanoparticles.<sup>104</sup>



### 1.3.8 Similarities between Raman, Fluorescence and Infrared (IR) Spectroscopy

Raman and IR spectroscopies both detect the vibrational energies of molecules with different selection rules. IR spectroscopy needs changes in the dipole moment when the molecule vibrates, while Raman spectroscopy needs polarization changes.<sup>64c</sup> For this reason molecules can only be either Raman or infrared active. Fluorescence involves the relaxation of the vibration, but Raman is sensitive to vibrational modes change. The sensitivity of Raman is more than fluorescence spectroscopy and namely called the fingerprint of molecules. Figure 1.7 illustrates the quantum description of Raman, fluorescence and IR and their spectrum accordingly. The cross section of Raman is much smaller than fluorescence and led to big disadvantage of Raman and be problem of not using Raman for a long time. After the invention of Surface-Enhanced Raman Scattering, surface Surface-Enhancement Rescued Spectroscopy.<sup>51, 57b</sup>

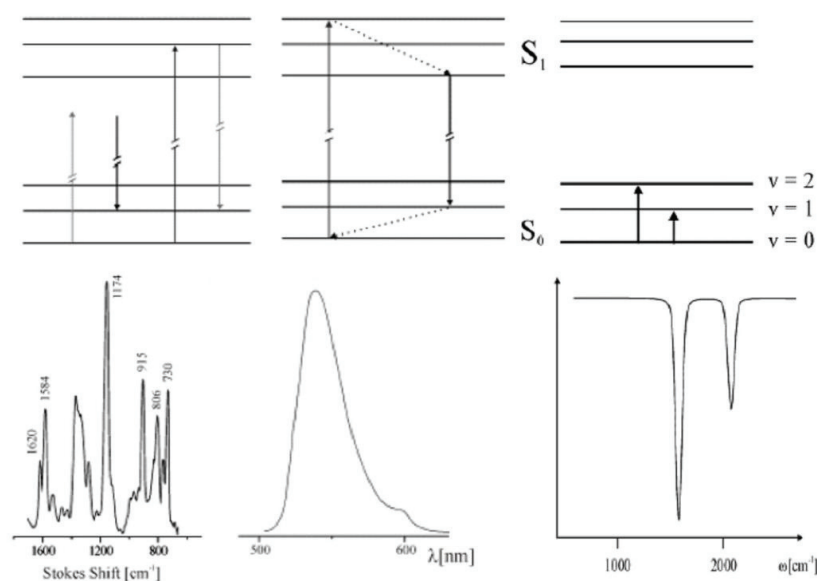


**Figure 1.7** The comparison of different scatterings.<sup>51</sup>

### 1.3.9 Literature Review

As mentioned above the first scattering was observed by Sir C. V. Raman which led to his 1931 Nobel prize in physics.<sup>105</sup> In 1974 for the first time,

Fleischmann et al. illustrate that the enhanced Raman intensities of pyridine on silver electrode is due to adsorbates on rough silver surface related to adsorbates amount on the increased area of the roughened surface.<sup>106</sup> Van Duyne and Jeanmaire<sup>107</sup> and Creighton and Albrecht<sup>108</sup> reported that the Fleischmann work could not be due to increasing of adsorbate which guide to SERS. In 1985, Raman surface enhancement accepted that have a sources with both chemical and electromagnetic mechanism.<sup>109</sup>

Many scientific reviews summarize SERS studies on biological molecules in the 1980s and early 1990s.<sup>110</sup> As an example, Van Duyne group presented the first step toward a glucose biosensor using SERS.<sup>111</sup> The stability and reproducibility of most SERS signals are not perfect. Van Duyne et al. have focused also on this problem by developing and characterizing a metal film over nanosphere electrode which solve these imperfections. The work illustrated that the metal film substrate, offers novel stability and reproducibility for electrochemical SERS experiments.<sup>112</sup>

El-Sayed and his co-workers demonstrate the first example of colloidal GNRs as SERS substrate in aqueous solution and on solid substrate.<sup>113</sup> In another work by Van Duyne and Christy L. Haynes, SERS properties of silver triangle prepared by natural lithography systematically investigated for the first time in the literature.<sup>53d</sup> In addition, it illustrated the need of correlating nanoparticle structure and LSPR spectroscopic datas in order to effectively implement SERS on patterned surfaces that have narrow ( $\sim 100$  nm) LSPR line widths. Plasmon-Sampled Surface-Enhanced Raman Excitation Spectroscopy (PSSERES) used to explain the relationship between the LSPR extinction maximum ( $\lambda_{\text{max}}$ ) and the SERS enhancement factor (EF). The functionality of the excitation wavelength, molecular adsorbate, vibrational band, and molecule-localized resonance or nonresonance excitation of PS-SERES was performed.

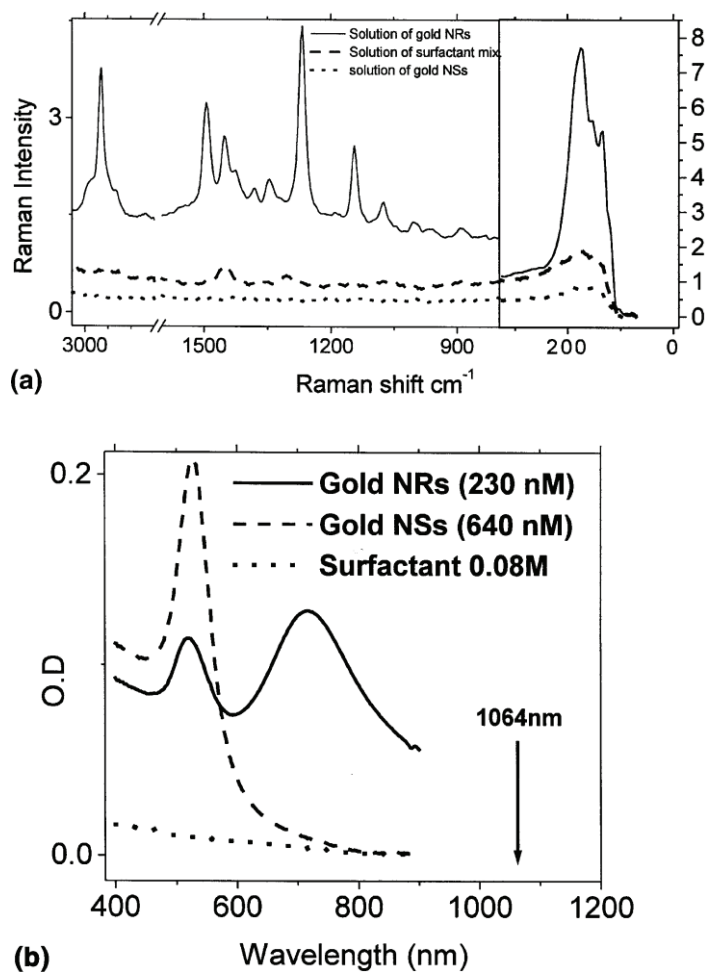


**Figure 1.8** (a) SERS of surfactant-capped gold NRs ( $25 \pm 2$  in length and  $12 \pm 2$  in width) in solution (solid line) is compared with surfactants (dashed line) and surfactant capped gold nanospheres (12 nm in size) (dotted line). In SERS of NRs the strongest peak is related to the Au–Br vibration, which is closer to the gold surface. (b) Visible spectra of the NRs, surfactant solution, and gold NSs. It can be seen that NRs show strong enhancement despite the fact that the excitation laser is 1064 nm.<sup>113</sup>

Xu and colleagues have showed mathematically the electromagnetic enhancements of  $10^{10}$  are present between two nanoparticles with inter-distance of 1 nm.<sup>114</sup> From this calculation authors demonstrated that aggregates nanoparticles are better substrates for SERS applications instead of individual nanoparticles due to large enhancements can be produced at particle junctions of aggregates.<sup>115</sup> Several studies have indicated that enhancement of the SERS dramatically increased by gold and silver nanoparticles.<sup>116</sup> The report by Zhang proved the SERS activity of aggregation of gold nanoparticle system has unique surface properties near IR absorption.<sup>117</sup> Additionally, Olivo et al. investigated the improving film stability and

SERS performance using an electrostatically charged glass slide as the supporting substrate.<sup>118</sup>

Van Duyne group in another study developed a sensors based on anthrax and glucose and probed by Surface-Enhanced Raman Scattering.<sup>119</sup> Ag nanotriangle assembly on glass substrate was prepared and used as SERS sensors. The Ag triangle substrates have been optimized for near-infrared (NIR) laser excitations by tuning the extinction maximum of their LSPR. In a recent study of Astilean group,<sup>120</sup> they showed that periodic arrays gold films deposited on top of highly ordered nanosphere to attempt the SERS potential from visible to NIR excitation. They also optimized the SERS activity of gold films for different excitation wavelengths (532, 633, and 830 nm) depending on the film thickness by quantitative and comparative assessment of the exhibited Raman enhancement.<sup>121</sup> Gold nanoparticle (GNP) based label-free SERS probe for ultrasensitive and selective detection of Trinitrotoluene demonstrated by Ray et al. for detection of various explosive application.<sup>122</sup>

To understand the SERS performance, nanoparticles with control structure and assembly introduce in recent years. Many novel nanostructures have been explored, including nanowire bundles,<sup>123</sup> nanoprisms,<sup>124</sup> nanoshells,<sup>125</sup> and nanoparticle.<sup>53a</sup> GNP aggregates in aqueous solution also provide an ideal platform for studying SERS.<sup>126</sup> The conjugate of thiol compounds with GNPs induces the nanoparticles has reduction in electrostatic repulsion. The distance between GNPs with molecules surrounding them satisfies the condition for SERS via the electromagnetic enhancement. Later, we can modify these nanoparticles by varying experimental conditions such as the size and surface functionality of the GNPs, the pH of the solution for SERS performance.<sup>126-127</sup> Yoon reported that charge-transfer (CT) enhancement in GNP contributed in SERS detection. This slow appearance of the CT provides an crucial clue to the difficult structural evolution of GNP aggregates.<sup>128</sup>

In another SERS study, Mangeney et al.<sup>129</sup> illustrated designing of a stimuable device made of gold nanoparticles conjugated to a gold flat film through an stimuli response polymer (poly(*N*isopropylacrylamide) (PNIPAM)) brush layer, that can thermally modulate the distance between the NPs and the substrate. Indeed,

temperature responsive polymer undergoes a reversible, inverse phase transition at a lower critical solution temperature (LCST) of about 32 °C in deionized (DI) water.<sup>130</sup> Below the LCST, PNIPAM is swollen and the chains are in an extended conformational mode and SERS spectra illustrated no coupling between gold nanoparticles and gold surface when the interparticles distance is larger. Above the LCST, PNIPAM is in a hydrophobically collapsed conformational mode. This mode leads the higher SERS spectra due to strong interaction regime.

Astilean and Boca demonstrated a method to replace cetyltrimethylammonium bromide (CTAB) with thiolated methoxy-poly(ethylene) glycol (mPEG-SH) polymer reduced GNRs toxicity for using as targeting agent in biological application. SERS measurements of isolated mPEG-SH-conjugated GNRs was detected.<sup>131</sup> Highly-order penta-branched various gold nanostructures such as rod, wire, and platelike particles was investigated by Zubarev and co-worker. In this study application of these gold particles with periodic starfruitlike morphology was shown by SERS.<sup>132</sup>

## 1.4 Nano-Lithography

The field of nanotechnology investigates miniaturized device characteristics to improve efficiency and low cost in various industries such as microelectronics, communications, and data storage industries. Recently, developments in nanotechnology have made the fabrication of nanostructures possible in the sub-nanometers regime with new features. The ideal nanofabrication technique should be inexpensive, flexible in size, shape, and spacing parameters, and massively parallel.<sup>133</sup>

“Bottom-up” and “Top-down” are two main procedures for nanofabrication. The “bottom-up” approach describes the manipulation of atoms, molecules and their assembly into bigger structures. This can be achieved by microscopes and natural self-assembly properties of molecules.<sup>134</sup>

The nanopatterns have been used in different areas to improve efficiency such as electrical, magnetic,<sup>135</sup> optical,<sup>57b, 136</sup> catalytic,<sup>137</sup> thermodynamic,<sup>138</sup> electrochemical,<sup>139</sup> electrical transport<sup>140</sup> and biological or physical properties. These properties provide benefit to acquire new functional materials and advanced devices. As an example, nanostructures with optical properties are used as filters,<sup>141</sup> substrates for surface-enhanced spectroscopies,<sup>142</sup> biosensors,<sup>143</sup> bio-probes, chemical sensors,<sup>144</sup> and optical devices.<sup>57c, 145</sup>

Lithography is a process to create patterns on a substrate and to form defines structures. Several nanolithographic techniques are used to create nanostructures with various features<sup>133, 146</sup> and are classified based on the method or the tool used. These lithographical techniques are Photolithography (optical, UV, EUV), E-beam/ Ion-beam/ Neutral Atomic Beam Lithography, X-ray Lithography, Interference Lithography, Scanning probe, Nanoimprint, Shadow mask and Natural/ Nanosphere Lithography. These nanostructure fabrication using lithography techniques is fast approaching but limit to capability and expensive process.<sup>147</sup> Among these lithography techniques, nanosphere lithography (NSL), is an inexpensive, material specific and high-output nanostructure fabrication process which can produce a 2-D array of periodic structures.<sup>88, 148</sup>

### 1.4.1 Nanosphere Lithography

For a lithographic colloidal mask preparation variety of submicrometer particles can be used in various materials with dimensions, and the surface charges. These colloidal particles can be synthesized in variety of materials, such as polymers,<sup>149</sup> noble metals, semiconductors or metal–polymer conjugates<sup>150</sup>. The polystyrene (PS) nanoparticles are frequently used for NSL<sup>151</sup> since they are monodispersed with a wide range of surface chemistries and charges. For a diameter smaller than 100 nm, silica nanoparticles are used, due to their low size dispersion.<sup>152</sup> For generation of nanopattern suitable colloidal particle with surface charge and size are important.

The colloidal mask is usually self-assembled on a planar base substrate that is patterned.<sup>153</sup> The wettability and surface charge properties help the formation of an ordered colloidal template due to the influence the solvent evaporation process and substrate–particle interaction. The materials such as conductive,<sup>151a</sup> insulating,<sup>154</sup> optically transparent,<sup>65a, 70a</sup> can be used as the substrate for colloidal mask. The glass or silicon<sup>151-152, 155</sup> are most common used substrates covered with thin metal layers,<sup>151a, 152</sup> metal oxides,<sup>156</sup> or with various types of polymers.<sup>152, 155</sup> Colloidal nanoparticles are electrostatically self-assembled in two dimension on the substrate.<sup>153</sup> The colloidal particles assembled on the substrate with different forces such as electrostatic particle–particle, particle–substrate interactions, hydrodynamic interactions, and diffusion to hexagonally pack the particles onto substrate (Figure 1.9).

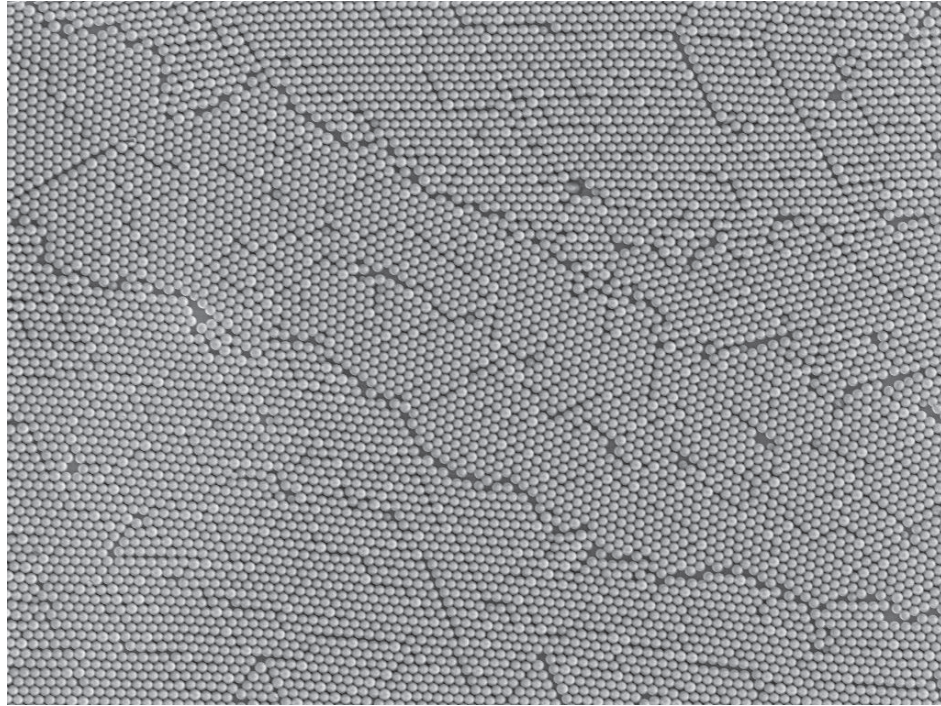


**Figure 1.9** Electron micrograph of hexagonally pack nanoparticles onto silicon substrate.

A number of methods exist for the formation of self-organized nanospheres such as spin coating,<sup>157</sup> drop coating,<sup>57c</sup> and thermoelectrically-cooled angle coating methods<sup>158</sup> in order to form a 2D colloidal crystal deposition mask. Each of these methods are briefly explained as follows, and describe the strengths and weaknesses.<sup>134</sup>

#### **1.4.1.1 Evaporation methods**

Evaporation methods are based on solvent deposited on a substrate with very low evaporation in the particle suspension. The particles begin to self-organize in very small areas and cause multilayer structures.<sup>158-159</sup>

#### **1.4.1.2 Electrostatic deposition**

Electrostatic deposition is based on electrostatic attraction forces and method requires oppositely charged among substrate surface and particles in an electrolytic



solution.<sup>156, 160</sup> The adsorption process is parallel but the spheres don't pack in the manner periodic structures.

#### **1.4.1.3 Dip-coating**

In dip coating the substrate is removed vertically from a sphere suspension with a constant velocity. As opposed to evaporation methods it is appropriate for large-area approximately tens of square millimeters can be coated.<sup>161</sup>

#### **1.4.1.4 Langmuir-Blodgett coating**

This method describes transfer of nanosphere from a liquid-gas interface onto a substrate surface by controlled vertical removal of the substrate. Some parameters such as differential surface tension or surface pressure of the monolayer is controlled via a feedback system.<sup>162</sup>

#### **1.4.1.5 Self-assembly on pre-patterned substrates**

Self-assembly on pre-patterned substrates provide controlled mesoscopic scale and formed in two steps; lithographic methods and self-assembled nanoparticle monolayers. A well composed monolayer of spheres is due to interactions between spheres and the previously functionalized areas. The first lithographic step causes to raise the processing time and cost.<sup>163</sup>

#### **1.4.1.6 Electrophoretic deposition**

In this deposition method, electrical currents use for the deposition and self-assembly of two- and three-dimensional colloidal crystals and limited for conductive substrate.<sup>164</sup>

#### 1.4.1.7 Spin-coating

Spin-coating is generally used in lithography with coating photoresist. Latex suspensions which have suitable viscosity and density can be used to make a thin layer. First the substrate is placed on the rotary stage and the suspension is dropped on the substrate, the spinning motion of the stage makes the liquid flow away. Other significant key-factors are the surface properties of the substrate and the spinning rate except that viscosity and density of the liquid. The mechanism of arrangement is likely to assembly of latex spheres.<sup>157, 159b, 165</sup>

#### 1.4.2 Literature Review

The NSL has other names in literature: “colloidal lithography” or “natural lithography” that become one of the techniques in nanotechnology field for patterning surfaces at nano-scale range.

In 1981, Fischer and Zingsheim introduced ‘natural lithography’ using “naturally”-assembled polystyrene latex nanospheres as a mask for contact imaging with visible light.<sup>166</sup> In 1982, Deckman and Dunsmuir demonstrated the use of a self-assembled nanosphere monolayer as a material deposition and at the same time as an etch mask. These authors used the term “natural lithography” to describe this process. The same group investigated various fabrication parameters and possible applications of this approach using always a single layer (SL) of nanospheres as the mask.<sup>160, 167</sup> Deckman’s “natural lithography” is an inexpensive, parallel, “bench-top” technique that can be used to fabricate Ag nanostructures for Surface-Enhanced Raman Spectroscopy (SERS).<sup>168</sup>

Finally, Van Duyne and Hulteen reported a work extending the SL methodology by (1) developing a double layer (DL) nanosphere mask, (2) performing atomic force microscopy (AFM) studies of SL and DL periodic particle arrays (PPAs) of Ag on mica, and (3) fabricating defect-free SL and DL PPAs of Ag on mica with areas of 10-100  $\mu\text{m}^2$  that were large enough to permit microprobe studies of nanoparticle optical properties. The process was renamed as “Nanosphere

Lithography” (NSL).<sup>157</sup> They also demonstrated that the versatility of NSL with respect to choice of substrate material  $S$  and deposition material  $M$ .

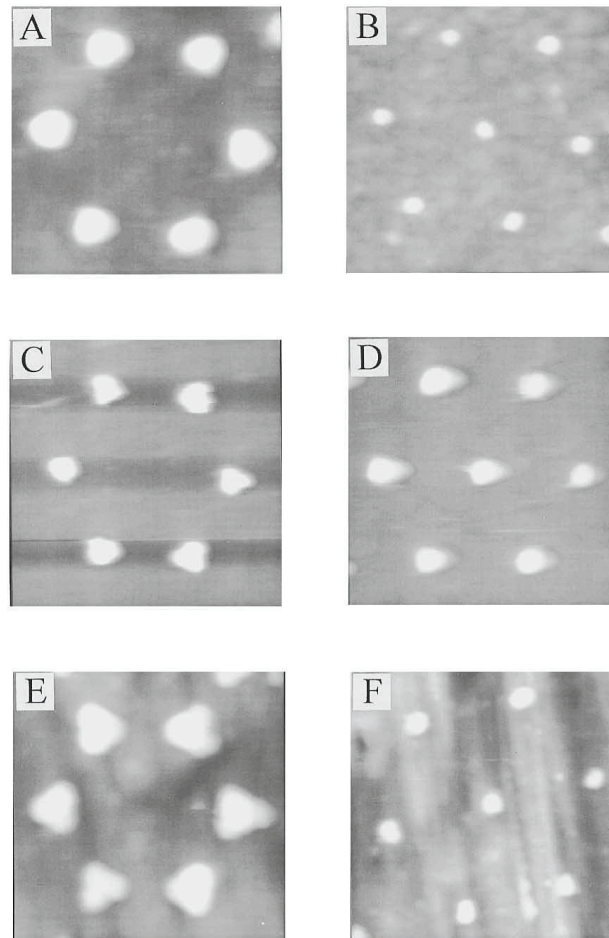


**Figure 1.10** AFM images of SL and DL PPAs of  $M=Ag$  on  $S=$ glass, Si (111), and Cu (100). (A) Ag SL PPA on glass, 437x437 nm image. (B) Ag DL PPA on glass, 757x757 nm image. (C) Ag SL PPA on Si(111), 515x515 nm image. (D) DL PPA on Si(111), 805x805 nm image. (E) Ag SL PPA on Cu(100), 490x490 nm image. (F) Ag DL PPA on Cu(100), 738x738 nm image.<sup>157</sup>

Many groups are improved this techniques to make a better quality colloidal masks. Van Duyne groups optimized natural lithography and became a popular. Van Duyne et al. has been shown that by using discrete dipole approximation (DDA) it is possible to obtain excellent agreement between the experimentally measured extinction spectrum of tetrahedral-shaped nanosized silver particles and the results of electrodynamic theory.<sup>159a</sup> In another study of Van Duyne and coworkers, quantitative nanofabrication of size-tunable periodic particle arrays was performed

via nanosphere lithography by selecting an appropriate nanosphere diameter and deposition mass thickness. Additionally, the sizes of small feature prepared by nanosphere lithography are close to those produced by the standard nanofabrication techniques (i.e., EBL, IBL, and XRL).<sup>57c</sup>

NSL has been widely used as an inexpensive (less than \$1 per sample) nanofabrication technique. It is inherently parallel and high-throughput. It can also be applied to general materials to investigate the size-dependent magnetic, electrochemical, optical, thermodynamic, and catalytic properties of materials.<sup>88</sup> Angle-Resolved Nanosphere Lithography (AR NSL) was used also by Van Duyne and co-workers to modify the size, shape, and location of nanoparticles while maintaining the strengths of conventional NSL mentioned above.<sup>133</sup> In another study of Van Duyne and colleagues,<sup>58</sup> fabrication of size-tunable Ag nanoparticles was performed using NSL.<sup>57c, 157</sup>

Large (a few  $\text{cm}^2$ ) monolayered masks could be directly applied onto any kind of surface through a self-assembly on a liquid- gas interface. This technique<sup>169</sup> provided large sizes of defect-free areas of prepared masks, a very quick preparation process (in comparison to drying-based methods) and a high level of hexagonal structure orientation. In addition, nanosphere lithography was used to prepare 2D arrays of perfectly ordered magnetic nanoparticles at large scale. The preparation method was modified to enable the self-assembly of latex particles on water surface.

In a work by Zareie et al., NSL was used to lay down an array of triangular Au/Al<sub>2</sub>O<sub>3</sub>/Au nanocapacitors on the (100) surface of *n*-doped silicon.<sup>170</sup> Another study of Zareie and coworkers showed different than the usual application of NSL technique which produces regular arrays of triangular structures, remarkably hexagonal ring-shaped structures of zinc oxide were fabricated by using can NSL and metal/metal oxide sputtering.<sup>171</sup>

A combination of colloidal self-assembly, preheating, and oxygen reactive ion etching techniques<sup>172</sup> were used to fabricate controllable nonclose-packed non-spherical PS particle arrays with long-range order. In this report, NSL was used to fabricate large uniform area of gold nanoholes in  $\text{cm}^2$  scale on glass substrate, which was in contrast to the smaller area of nanoparticles obtained by closely packed NSL.

The LSPR sensitivity of nanoholes towards local refractive index was measured. BSA binding was then detected. Separately, biotin-streptavidin immunoassay to gold nanoholes was performed.<sup>173</sup>

Colson and colleagues demonstrated the influence of each parameter on the degree of ordering of the nanospheres layers. Therefore, it does not aim at giving new insights in colloidal scale forces or transport effects in fluids.<sup>174</sup> Nagayama and co-workers<sup>159b, 175</sup> described the mechanism and stages of the process of colloidal particle ordering into 2D hexagonal close-packed array. The authors investigated of interactions and forces between colloidal nanospheres, leading to the formation of arrays on a solid substrate or in thin films of liquids. The mechanistic principles of 3D colloidal crystal growth were investigated by Scriven and coworkers using evaporation-induced convective steering.<sup>176</sup>

Ring-stain deposits formed in drying drops containing dispersed solids were investigated by Deegan et al.<sup>177</sup> The pattern of ring-stain deposition was ascribed to a form of capillary flow in which pinning of the contact line of the drying drop ensures that liquid evaporating from the edge is replenished by liquid from the interior. Theoretical description of self-assembly mechanisms have been reported in various literature including publications by Zhao et al.<sup>178</sup> and Regh et al.<sup>179</sup>

## 1.5 Nanorods Overview

Noble metals nanoparticles have received a great deal of interest for their optical and plasmonic properties. Their optical properties depending on size and structure have brought a great potential in nanoelectronics, nano-biosensors and plasmonics applications. In 5th century before christ (B.C.) the synthesis of GNP or colloidal gold was used as a method of staining glass.<sup>180</sup> In 1857 Faraday recognize that the brilliant color of these glasses is due to the presence of the gold particles in the pigment solution.<sup>181</sup> He demonstrated the formation of red solutions of colloidal gold in a two-phase system. Various methods for the synthesis of gold particles were reported in 20th century.<sup>182</sup> In 1951 J. Turkevich introduced simple method for preparation of colloidal gold using citrate reduction of Tetrachloroauric (III) acid ( $\text{HAuCl}_4$ ) in water which this method used for a long time.<sup>182b</sup>

With the evolution of nanotechnology, gold nanoparticles as building blocks in practical nanotechnology play an important role.<sup>183</sup> The progress in synthesis of nanoparticles and the influence of the particles size on the physical, chemical and optical properties of the material have been previously studied.<sup>184</sup> The rods, wires and core-shell structures of noble metals in particular gold which are not spherical shape have been extensively investigated.<sup>184</sup> Among these particles, NRs are the most popular research area due to their easy synthesis, control over the aspect ratio and potential application in biological sensing and plasmonic.<sup>185</sup>

Nanorod have two separate absorption bands which is due to transverse and longitudinal structures of the rod while the spherical gold nanoparticles has only a single strong band as illustrated in Figure 1.11. These absorption bands happen when the incident photon frequency is resonant with the collective oscillation of the free electron cloud of the particle, and is known as “LSPR”.<sup>186</sup>

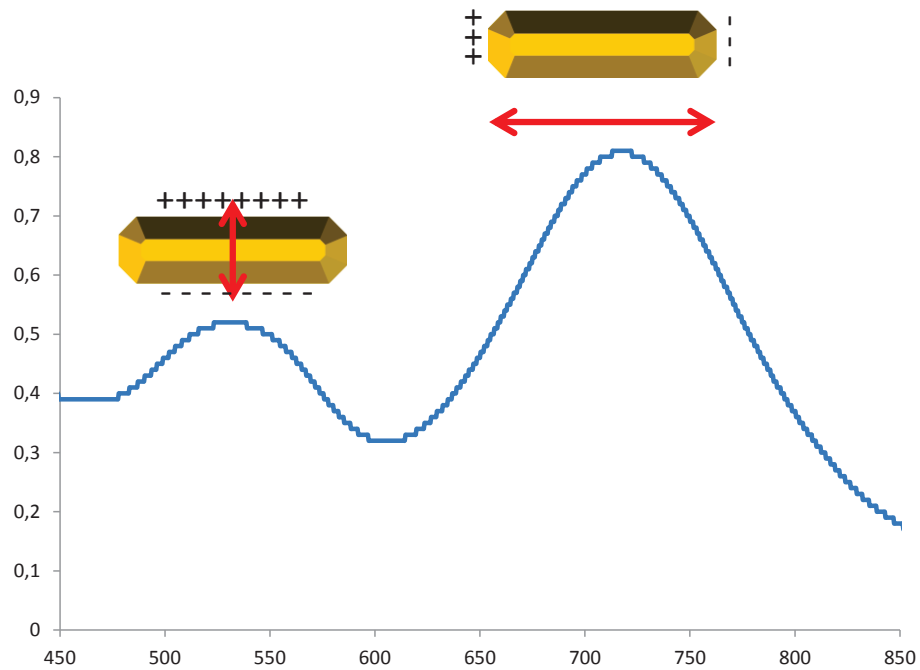


**Figure 1.11** Typical surface plasmon absorption spectrum of gold nanorods. The strong long wavelength band in the near infrared region around 730 nm is due to the longitudinal oscillation of electrons and the weak short wavelength band in the visible region around 520 nm is due to the transverse electronic oscillation.

The optical property of GNPs is dependent on size, environment surrounding, and the shape of the nanoparticles. The aspect ratio in GNRs is the value of the longitude divided by the width and lead to energy separation between the resonance frequencies of the long and short bands by increasing the aspect ratio.<sup>187</sup> For an example, if someone aims for an aspect ratio (AR) of '4'. This could be achieved by a nanorod feature in the range of 80 nm longitude, and 20 nm diameter, giving an AR of '4'.<sup>186b</sup>

$$\text{Aspect Ratio} = \frac{\text{Length of major axis}}{\text{Width of rod diameter}} = \frac{80 \text{ nm}}{20 \text{ nm}} = 4$$

GNRs show different color depending on the aspect ratio which allows the gold nanorods to be used in optical applications.<sup>188</sup> One of these applications is in the biological area. For example NRs bind to specific cells with higher affinity and one

can observe the conjugated cell using a simple optical microscope due to the enhanced scattering cross section.<sup>189</sup> This is how for the diagnosis of diseases such as cancer GNRs can be use as the biosensor. NRs with high enhancement of the longitudinal plasmon resonance<sup>190</sup> can enhanced fluorescence over bulk metal and beneficially can be use in sensory field. With increasing the intensity of the surface plasmon resonance absorption the enhancement of the surface enhanced Raman scattering of molecules adsorbed on GNRs<sup>113</sup> occur which make GNRs a excellent candidate for future of nanoelectronics. The uses of GNRs in various applications have been increased. With increasing of applications of GNRs, the mechanisms of the morphology and geometry still is obscure and also the reproducibility of the synthesis is poor.<sup>185</sup>

In the wet chemistry the NPs, structures are determined both by the kinetic and thermodynamic factors. In most cases, the growth process of GNRs which contains different structures illustrates the thermodynamic energy and kinetics effect.<sup>191</sup> When this kinetic energy is very strong, it leads in special types of particle morphologies such as rods, needles, platelets, and dendrites.<sup>185</sup>

### 1.5.1 Literature Review

GNRs with aberrant optical properties have become a favorite in variety of research area. El-Sayed et al. reported the effect of temperature on GNRs encapsulated in micelles<sup>192</sup> with an average aspect ratio of 3.3.<sup>193</sup>

Esumi et al. were used the photochemical reduction in the presence of cetyltrimethylammonium chloride to developed gold nanostructures.<sup>194</sup> This approach illustrated the capability of anisotropic growth in precipitation reactions; the resulting threadlike gold nanostructures with poor morphology. Murphy's group introduced a seed mediated approach in which GNPs are used as seeds to grow GNRs.<sup>195</sup> El-Sayed and coworkers showed that the efficiency of the reaction as well as the control of NR anisotropy can be increase using Ag(I) during rod formation.<sup>196</sup>

In particular, GNRs growth mechanism can be analyse by the presence of the CTAB, which conducted by Murphy and co-workers,<sup>195</sup> has become very popular.



Murphy's group also illustrated that the shape of GNRs depends on the changes of the surfactant. They examined C<sub>16</sub>TAB with different length and tail groups and demonstrated these length changes are critical for production of GNRs.<sup>197</sup>

In another study, Wei and Zamborini<sup>198</sup> described the investigation of the GNRs growth using seed mediated method under liquid AFM which is motivated by work of Murphy and co-workers. They synthesized GNRs with controlled AR in aqueous solutions using seed-mediated growth method.<sup>195</sup> Murphy et al. method was later extended synthetically to the growth of NRs on the surfaces.<sup>199</sup>

Nikoobakht and El-Sayed<sup>200</sup> produced GNRs with different aspect ratio in solution by changing the amount of silver nitrate for a given amount of gold. They showed that the GNRs with high yield depended on surfactant-stabilized Au seeds. Later Murphy's group extended this study to produce a very high yield of short GNRs with average lengths of 20 to 100 nm. They also investigated that the various reaction parameters can directly effect on NRs dimension. They reported also the ascorbic acid play important role in aspect ratios of GNRs.<sup>201</sup>

Zweifel and Wei<sup>202</sup> demonstrated that increase in the amount of Na<sub>2</sub>S in growth solution can directly reduce the optical drift in GNRs. The sulfide treatment gives an additional ameliorates by the dielectric function at the surface of nanorod which leads the plasmon resonances shifting toward longer wavelengths. The NRs after treatment with sulfide are stable at room temperature.

Jana for the first time developed a new method for synthesis of GNRs in which seed solution is not necessary. He demonstrated a mixture of strong and weak reducing agents is introduced into the micellar solution of a metal salt, where the strong reducing agent initiates nucleation and the weak reducing agent helps the nanoparticles to grow.<sup>203</sup>

Different approaches such as electrochemical,<sup>192</sup> photochemical,<sup>204</sup> and seed-mediated methods<sup>200</sup> have been used to grow GNRs. In one study, it was reported that addition of NaOH in which increase the pH of solution is crucial for formation nanorods with high aspect ratio in seed mediated method.<sup>205</sup> In another study by

Yang Wu et al. illustrated the addition of nitric acid to seed mediated solution lead to monodispersity and higher aspect ratio of GNRs.<sup>206</sup>

Jana et al. demonstrated that CTAB micelles break down at high temperature and NRs cannot produce that is why they indicated that GNRs only form at temperatures below 50 °C.<sup>203</sup> Pe´rez-Juste et al. also reported the same hypothesis that temperatures of reaction must be close to room temperature for higher NR yields.<sup>207</sup> Zijlstra et al. reported that the temperature of the GNRs solution can increase up to 90°C in seedless method without breakdown the micelles formation.<sup>208</sup>

The concept of functional nanoscale devices based on plasmonic circuitry recently has been reported. Methods to obtain end-to-end self-assembly of metallic nanorods in suspension have been reported, while methods to stick GNRs on derivatized have also been demonstrated. Zareie et al.<sup>209</sup> illustrated the protocol originally due to Caswell et al.<sup>210</sup> in which GNRs can be assemble end-to-end, into long chains attached on top of a mixed self-assembled monolayer that has been functionalized with streptavidin (SA).

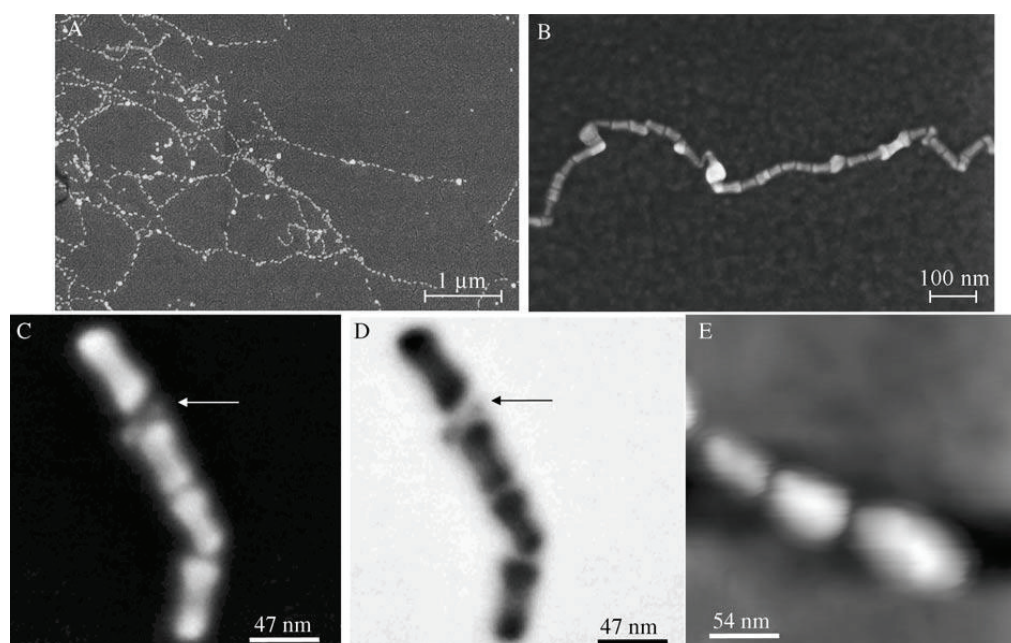


**Figure 1.12** Chains of NRs attached to a derivatized substrate. SEM images of A) networks of NR chains attached to the surface of the SAM, and B) a long chain of GNRs. C) High-resolution SEM image of a portion of a chain, which shows a region (arrowed) that appears to contain more than one SA molecule as binder. D) Negative image of (C). E) AFM image of the end portion of a chain.<sup>209</sup>

Many researches on application of GNRs in biology and health sciences have been mooted. Green et al.<sup>211</sup> reported a comparison of the Liao and Hafner<sup>212</sup> protocol for PEGylating antibody-GNRs conjugates resulting in a 33.9% improvement in the conjugation efficiency of GNRs to tumor-targeted antibodies.

## 2 EXPERIMENTAL AND METHODS

The method is described in two sections:

### 2.1 Method for Nanosandwiches

#### 2.1.1 Materials

Polystyrene nanospheres with diameters of 1000 nm, 500 nm, 200 nm (10 wt % solution in water, Sigma) and 400 nm (4 wt % solution in water, Interfacial Dynamics) were received as a suspension. Absolute Ethanol, Dichloromethane, methanol, Hydrogen Peroxide (30%), Sulphuric Acid, Ammonium Hydroxide (32%) were from Merck. Triton X-100, Phosphate-Buffered Saline (PBS, pH=7.4) and Streptavidine were purchased from Sigma. EZ-Link HPDP-Biotin (99%) was from Pierce. Silicon (p-type; 100, Silicon Inc.) was used as received. Glass substrates, No. 2 Fisherbrand (18 x 18 mm) cover slips were purchased from Fisher Scientific. Deionized (DI) water ( $18.2 \text{ M}\Omega\text{cm}^{-1}$ ) in the experiment was purified (Thermo Scientific) by treatment in a reverse osmosis. Cr (Plated Tungsten Rods), Ag,  $\text{Al}_2\text{O}_3$  (99.99%) and  $\text{HfO}_2$  (99.99%) were purchased from Kurt J. Lesker Company and Au (99.99%) was acquired from jewelry store.

All polymers in this thesis were synthesized by Dr. Volga Bulmus laboratory from İzmir Institute of Technology (IYTE). The polymers are described in detail elsewhere.<sup>213</sup>

### 2.1.2 Substrate preparation

Glass and silicon substrates were immersed in a piranha solution (3:1 30% H<sub>2</sub>SO<sub>4</sub>: H<sub>2</sub>O<sub>2</sub> **CAUTION**) at 65°C for 0.5h. Substrates were cooled down at room temperature, the glass substrates were rinsed thoroughly with DI water as to generate the surface hydrophilic and then sonicated for 60 minutes in 5:1:1 H<sub>2</sub>O:NH<sub>4</sub>OH:30% H<sub>2</sub>O<sub>2</sub>. The substrates were rinsed repeatedly with copious amounts of water and the remains were stored in water till they were used. Finally, they were dried under a stream of nitrogen gas and placed in drying oven at 75°C for 30 min for further treatment of the surfaces from wettability.

### 2.1.3 Nanosphere Lithography

Aqueous suspensions of polystyrene spheres were diluted to a solution of the surfactant Triton X-100 in methanol (1:400 vol/vol) to serve the solutions in wetting the substrate and pack better before spin-coating. The dilution factors were adjusted to the nanosphere sizes. In order to fabricate Nanosphere Lithography (NSL) masks, self-assembled nanospheres were created as a form of hexagonal close-packed monolayer. Suspension was hold in sonication and applied vortex before use. Then, 10  $\mu$ L of the resultant suspension was dropped onto the substrate and then spun at 2000 rpm for 40 sec<sup>171</sup> or three step method<sup>214</sup> according to size of nanosphere. Spin coating was performed on a Laurell spin coater.

### 2.1.4 Metal deposition

The substrates were fixed in the vacuum deposition chamber with the base pressure of  $\approx 8 \times 10^{-6}$  Torr, which was evacuated for a minimum of 4 h. Single Au layer and multilayer structures of Au / Al<sub>2</sub>O<sub>3</sub> / Au were deposited over the nanosphere mask by using NANOVAK thermal evaporator for the Au and RF magnetron sputtering for the Al<sub>2</sub>O<sub>3</sub> (Alumina). As an other sample, for preparing multilayer structures of Au / HfO<sub>2</sub> / Au, HfO<sub>2</sub> (Hafnium Oxide) was only deposited in Vaksis deposition chamber equipped with a DC/RF magnetron sputter system, while sputtering was carried out in presence of flowing Ar, at a pressure of 20 mTorr.

Deposition rate and film thickness were monitored with a quartz crystal microbalance. The thickness of each layer was changed between 20 and 50 nm. After metal deposition, the each specimens were hold in dichloromethane by sonicating for 2-5 min in comparison with the thickness of coated metal to remove the nanosphere and then the samples were thoroughly rinsed with  $\text{CH}_2\text{Cl}_2$  and dried under a stream of nitrogen ( $\text{N}_2$ ) gas.

### **2.1.5 Nanostructure functionalization with Temperature Responsive Polymers**

In order to bind specific polymers to Au /  $\text{Al}_2\text{O}_3$  / Au nanosandwich arrays, sample was incubated in 0.01 mM thiol terminated polymer (which is specific to Au layer) solution in ethanol for 24 - 48 hours. After incubation, the sample was thoroughly rinsed with ethanol to remove all physisorbed molecules and dried by flowing  $\text{N}_2$  gas. The same procedure was repeated with phosphate terminated polymer (0.01 mM) for modification of  $\text{Al}_2\text{O}_3$  layer. For modification of Au /  $\text{HfO}_2$  / Au nanosandwich array, the nanosandwich array was incubated in silane terminated polymer solution in ethanol (0.01 mM) for 24-48 hours. The same rinsing and drying process was repeated. All experiment was performed in glove box.

### **2.1.6 Biorecognition of Nanosandwich arrays for LSPR Biosensor**

The unfunctionalized Au /  $\text{Al}_2\text{O}_3$  / Au nanosandwich arrays were incubated in 0.1 mM mixed SAM (containing thiol terminated polymer and EZ-Link HPDP-Biotin at a mol ratio of 9:1) for 24 h. The mixed SAM coated nanosandwich array was washed with ethanol and dried, then heated above the LCST (45°C). The nanosandwich arrays having the collapsed state of the polymer was incubated with SA (2  $\mu\text{M}$ ) in PBS for 30 min. Finally, the substrate was washed with PBS and dried under ambient condition.

## 2.2 Method for Nanorods (NRs), Nanoparticles (NPs) and Nanobubbles

### 2.2.1 Materials

All chemicals were purchased from various suppliers with  $\geq 99\%$  purity and used as-received. Hexadecyltrimethylammonium bromide (CTAB) and 1-Decanethiol – Sigma Aldrich, Tetrachloroauric (III) acid and Silver Nitrate ( $\text{AgNO}_3$ ) – Alfa Aesar, Sodium borohydride granular ( $\text{NaBH}_4$ ) – Aldrich, L-ascorbic acid – Fluka.

Silicon (p-type; 100, Silicon Inc.) was used as received. DI water ( $18.2 \text{ M}\Omega\text{cm}^{-1}$ ) treated through reverse osmosis (Thermo Scientific) was used for preparing all solutions.

### 2.2.2 Gold Nanorod Synthesis

In this work, gold nanorods (GNRs) were synthesized by two well-known methods as described below.

#### 2.2.2.1 Seed Mediated Synthesis<sup>215</sup>

The experimental procedure of seed mediated method illustrated in Figure 2.1.

##### **Synthesis of Seed Solution**

An aqueous sodium borohydride (0.01 M, 0.6 ml) was added to a 10 ml aqueous solution containing CTAB (0.1 M, 9.75 ml) and  $\text{HAuCl}_4$  (0.01 M, 0.25 ml). After addition, solution was stirred for 2 min.

##### **Synthesis of Growth Solution**

CTAB (0.1 M, 9.5 ml) was mixed with  $\text{AgNO}_3$  (0.01 M, 75  $\mu\text{l}$ ),  $\text{HAuCl}_4$  (0.01 M, 0.5 ml) and ascorbic acid (0.1 M, 55  $\mu\text{l}$ ), respectively. Then, 12  $\mu\text{l}$  of seed solution was added to this mixture. The growth solution was stored overnight at room temperature for rod formation.

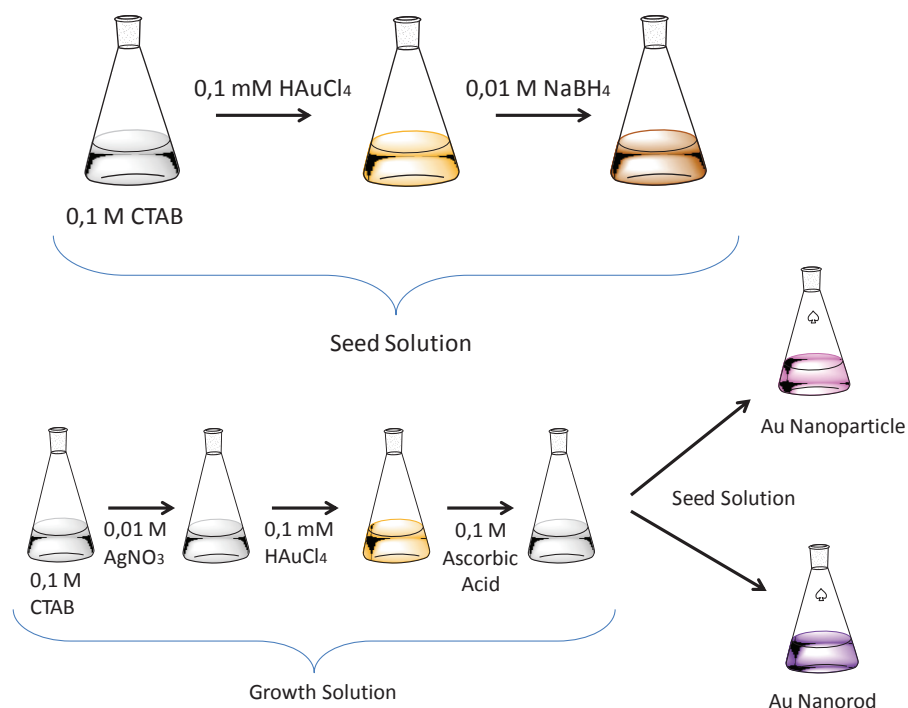


**Figure 2.1** Schematic representation procedure for preparation of GNR using seed mediated synthesis.

### 2.2.2.2 Single Step Synthesis

In this method we synthesized the GNRs according to Jana<sup>203</sup>; HAuCl<sub>4</sub> (2 mM, 5 ml) , CTAB (0.2 M, 5 ml) , AgNO<sub>3</sub> (0.0084 M, 250 μl) , Ascorbic acid (0.084 M, 250 μl) and NaBH<sub>4</sub> (0.001 M, 100 μl) were mixed in vials.

### 2.2.3 Production of Gold Nanoparticle from NRs

Gold nanoparticles (GNPs) were prepared according to the abovementioned methods (procedure described in Section 2.2.2) with introducing the various gases such as N<sub>2</sub>, Argon (Ar) and Hydrogen (H<sub>2</sub>) with different flow velocities and time exposed. First we flow the gas into the seed solution only and complete the synthesis according the above methods (seed mediated). The next experiments carried out by flow the gas to both growth and seed solutions. This experiment repeated for seedless synthesis as well.



#### **2.2.4 Conversion of GNPs to NRs procedure**

In order to acquire the GNR through nanoparticles from single step method we replaced the NPs with H<sub>2</sub>AuCl<sub>4</sub> in the seed solution. In parallel experiment, NPs were used as seed solution. While all the seed mediated methods remained same for complete nanorods production.

#### **2.2.5 Production of Nanobubble and Semi-shell**

Nanobubbles and semi-shells were obtained in compliance with seed mediated method. In this part of the experiment we flow the N<sub>2</sub> gas to seed solution.

#### **2.2.6 Conjugation of GNRs with triangle Gold Nanodot arrays**

To achieve high concentration gold nanorods, GNRs procedure was prepared by Green et al.<sup>211</sup> The unfunctionalized Au nanodot arrays described in Section 2.1 were incubated in 0.1 mM mixed SAM (containing decanethiol (DT) and EZ-Link HPDP- Biotin at a mol ratio of 9:1) for 24 h. The mixed SAM coated nanodot array was washed with ethanol and dried, then was incubated with SA in PBS for 24 h and was washed with PBS and dried under ambient condition. As prepared GNRs suspension was mixed with DT and EZ-Link HPDP-Biotin at a mol ratio of 9:1 for overnight. The SA binding functionalized nanodot arrays was incubated in the mixed SAM coated GNRs suspension. Finally, the substrate was washed and dried, respectively.

#### **2.2.7 Centrifugation**

Gold nanostructures were separated from the undesired structures and excess surfactant by centrifugation (WiseSpin CF-10) twice at 10000-13500 rpm for 20 min two times with respect to nanostructures dimension (till most of the surfactant was removed). In each cycle, UV-Vis measurements were performed after precipitates redispersed in DI water and also for the supernatants.

## **2.3 Characterization Methods**

### **2.3.1 UV-Vis / Near IR Spectroscopy**

UV-Vis measurements were carried out in a home-built instrument made by Nanodev Ltd. (Bilkent, Cyberpark) using an Ocean Optics USB2000+VIS/NIR spectrometer (350-1100 nm). All absorbance spectra were collected in quartz cuvette.

### **2.3.2 Localized Surface Plasmon Resonance (LSPR) Spectroscopy**

The schematic presentation of the home-made LSPR Spectroscopy setup, which was manufactured by Nanodev Ltd. ( Bilkent, Cyberpark ), is illustrated in the Figure 2.2. Extinction measurements were collected via Ocean Optics HR2000 spectrometer fiber optically coupled to a light microscope with unpolarized white light by a tungsten-halogen lamp. In this study, all spectra were recorded in standard transmission geometry-mode. The beam is passed through the sample with a 40X (NA=0.65) or 100X microscope objective (NA=1.25). The microscope objective collects the light, whereas the transmitted light is focused into a 400 $\mu$ m core diameter optical fiber cable and directed into the spectrometer ranged from 450 nm to 1100 nm. The probe-light spot diameter was approximately 4 mm. The LSPR spectra were monitored associated with data processing software (SpectraSuite, Ocean Optics Inc.), included boxcar smoothing and the average of 10 different points with 1000 ms integration time. All data presented have been smoothed. The LSPR spectra were collected from 10 different points of the sample in the ambient conditions.

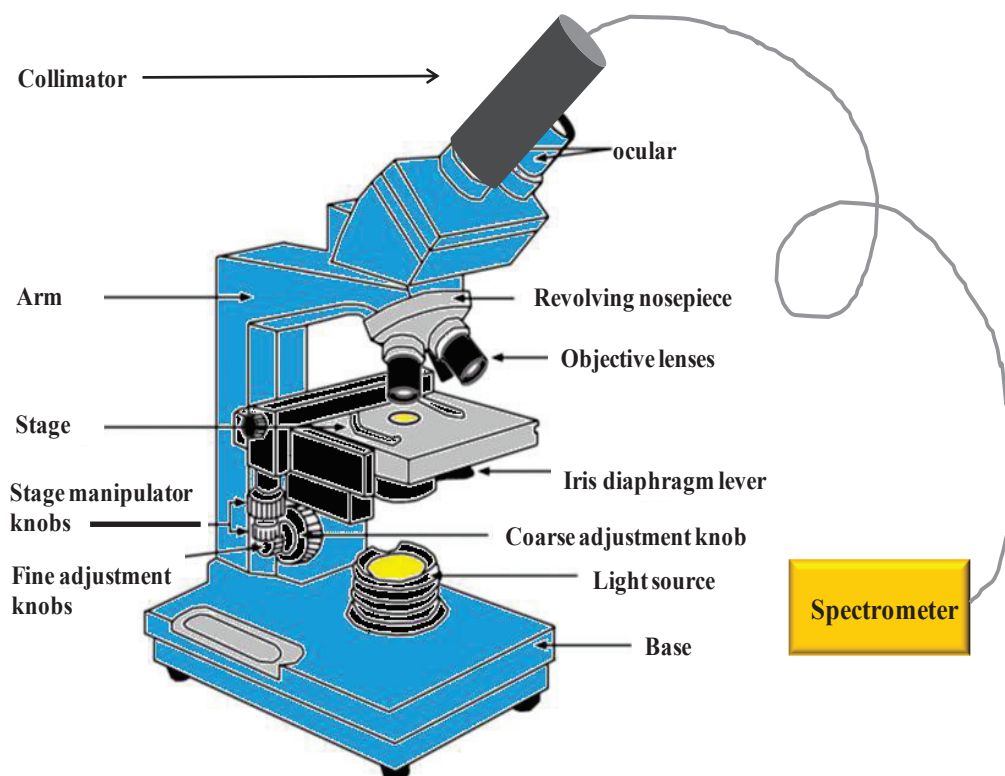


**Figure 2.2** Schematic illustration of LSPR Spectroscopy setup.

### 2.3.3 Surface Enhanced Raman Spectroscopy (SERS)

The schematic presentation of the home-made RAMAN system, which was manufactured by Nanodev Ltd. (Bilkent, Cyberpark), is shown in the Figure 2.3. In system, excitation light source is a continuous wavelength diode-pumped solid state laser at 532 nm and have a laser power with 15 mW. Laser irradiation was coupled with 100  $\mu\text{m}$  core diameter fiber and appropriate highpass, lowpass, notch filters (Thorlabs) was placed in the beam path. We have used HR2000 Spectrometer from Ocean Optics as the Raman detector, it is equipped with 2048 pixel Linear CCD arrays. The spectral response of this spectrometer is ranging from 0 to 4000  $\text{cm}^{-1}$ . The signal of the SERS was obtained with 40X objective in 180° backscattering geometry, integrating time of each measurement was 1second. The Raman spectrum was collected with Ocean Optics data acquisition SpectraSuite spectroscopy software. The SERS spectra were collected from 10 different points of the sample in the ambient conditions.

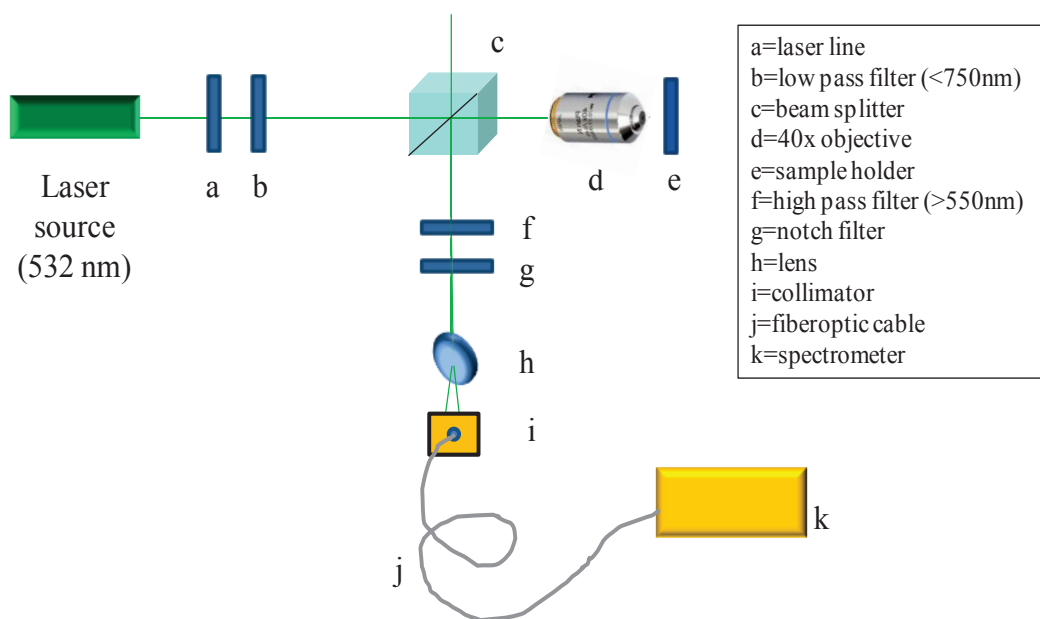


**Figure 2.3** Schematic illustration of Raman system.

### 2.3.4 Surface Plasmon Resonance Spectroscopy (SPRS)

Surface Plasmon Resonance Spectroscopy is based on monitoring the adsorption of biomolecules from liquid on to solid surface (such as gold and silver). The principle is based on the excitation of surface propagating electromagnetic waves called surface plasmons which will interact with any species which are present on the surface. The schematic presentation of the home-made SPR system, which was manufactured by Nanodev Ltd (Bilkent, Cyberpark), is illustrated in the Figure 2.4. SRPS involves a polarised laser light beam with 705 nm wavelength that passed through a prism which a gold coated glass attached to its surface using index matching liquid. The light is reflected off the gold-glass interface due to total internal reflection which in the process generates evanescent waves. The evanescent waves interact with the gold atoms and excite surface plasmons which are basically strong electromagnetic waves present on the surface of the metal. At this point, there is almost complete attenuation of the specular signal intensity producing a dip for that specific incidence angle which is referred to as the SPR angle. When species are

adsorbed onto the gold surface, the angle shifts slightly which is directly proportional to the amount of the specific analyte present on the gold.<sup>216</sup>

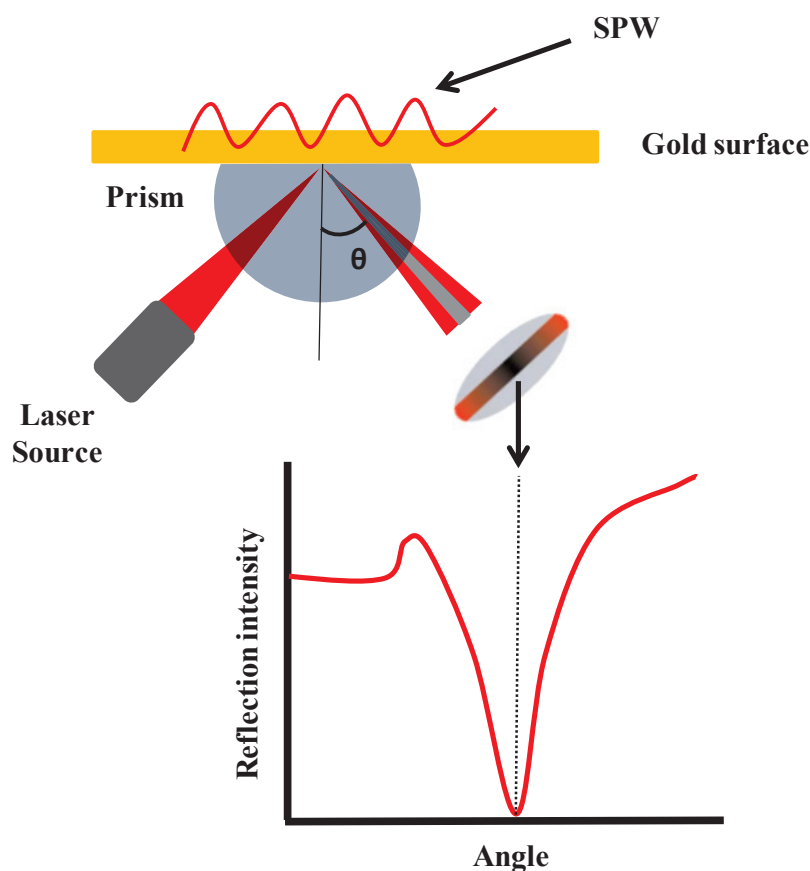


**Figure 2.4** A schematic representing the operation of a SPR device.

### 2.3.5 Atomic Force Microscopy (AFM)

A Nanomagnetism Instrument Multimode Scanning Probe Microscope (Figure 2.5) operating in tapping mode at the room temperature in air was used to obtain topographic data. All imaging operations were conducted with 512 x 512 data acquisitions at a various scan speed. Oxide-sharpened silicon nitride tips with integrated cantilever with a nominal spring constant of 42 N/m were used. These tips have resonance frequencies between 204 and 497 kHz and an effective radius of curvature at the tip of less than 7 nm. AFM images were manipulated by using Scanning Probe Image Processor (SPIP) software.

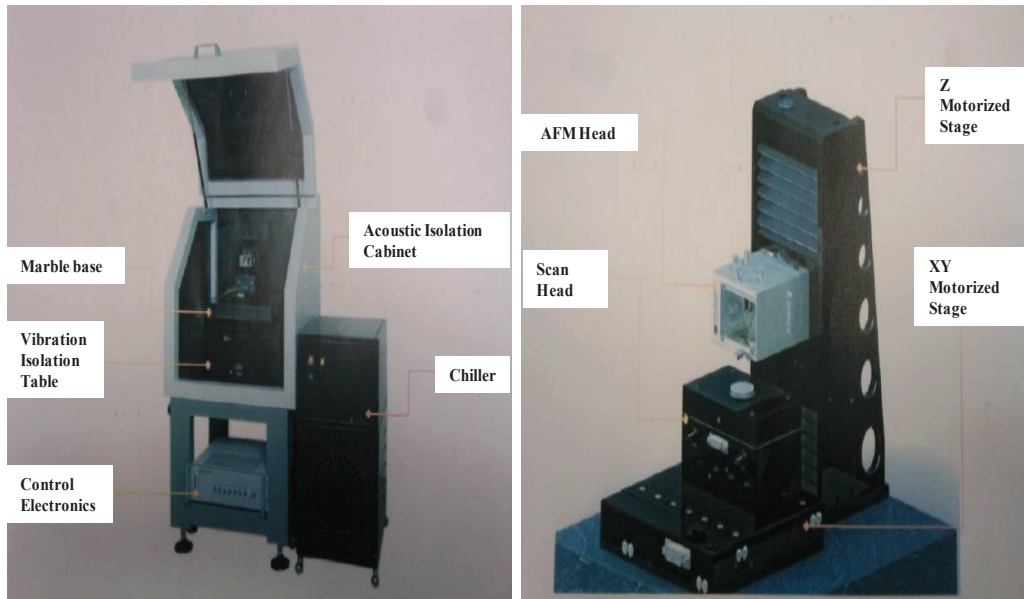


**Figure 2.5** Atomic Force Microscope.

### **2.3.6 Scanning Electron Microscopy (SEM)**

SEM images were obtained ( Prof. Dr. Müjdat Çağlar, Electric and Electronics Department, Anadolu University, Eskisehir ) using a Zeiss Ultra Plus High Resolution FE-SEM ( Figure 2.6 ) equipped with an in-lens secondary-electron detector at operating range 2-20 KV depends on samples charging. Samples were dropped onto silicon substrates and dried in a desiccator.



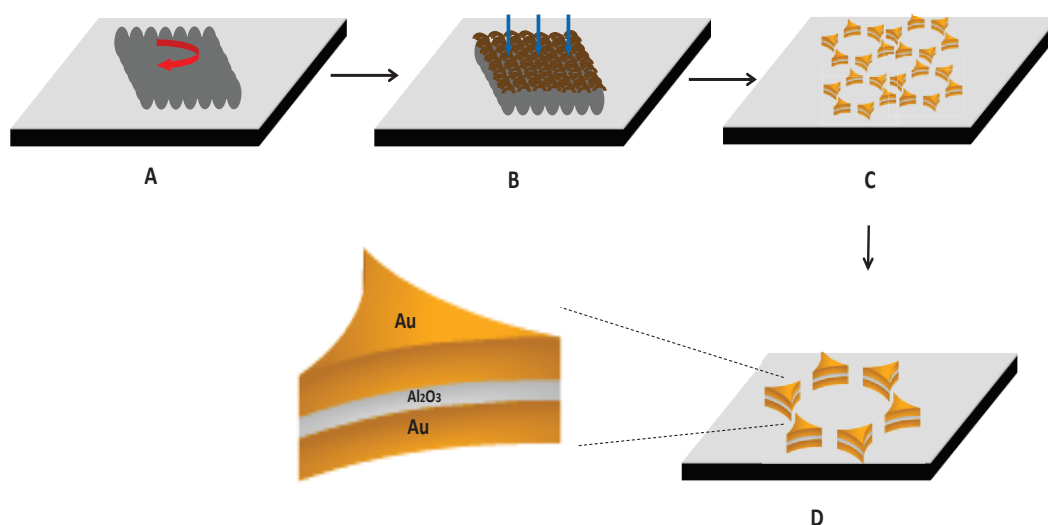
**Figure 2.6** Ultra plus high resolution field emission-scanning electron microscope

### **3 RESULTS AND DISCUSSION**

#### **3.1 Analysis of Nanoarray Structures with Various Noble Metals and Thicknesses**

The nanostructures with single or multilayers before and after treatment with polymeric materials and biological macromolecules were initially analyzed using different techniques. The principle of nanostructure preparation by nanosphere lithography is illustrated and explained in Figure 3.1. The templating sphere is polystyrene, with a diameter in the 200 to 1000 nm range. The nanoparticle arrays are subsequently used as a mask for deposition of the noble metals and inorganic compounds such as Au, Ag, Al<sub>2</sub>O<sub>3</sub> and HfO<sub>2</sub> in this study. The first step involves spin coating of polystyrene nanoparticles solution onto a cleaned glass and silicon substrates (Figure 3.1A). The nanoparticles exhibit hexagonal close packings (HCP) across significant areas of the surfaces. Next, noble metals or inorganic compounds were deposited onto the mask using physical vapor deposition techniques. The material deposited both onto the triangular voids of the HCP array as well as the top of the latex spheres. Lift off of the polystyrene nanoparticles by sonication and thoroughly rinsing in dichloromethane yielded pattern of triangular structures with sizes from 200 nm to 400 nm.





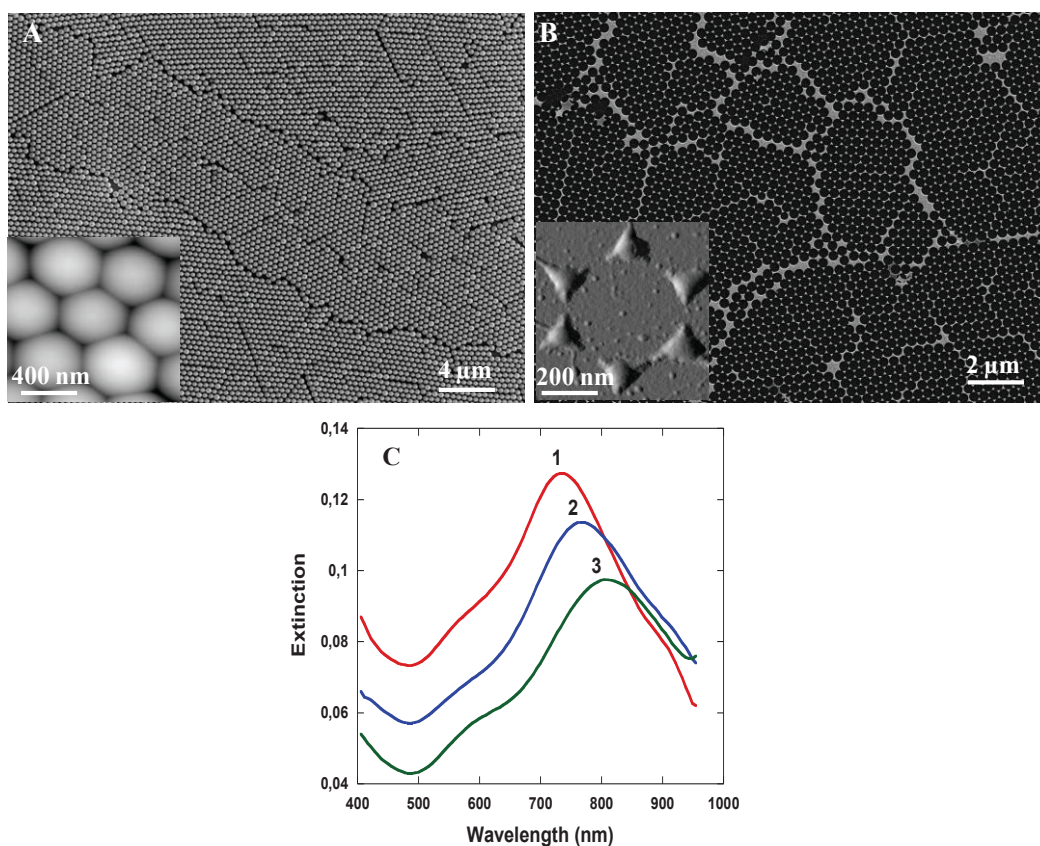
**Figure 3.1** Schematic illustration of the general process of the nanosandwich arrays preparation by Nanosphere Lithography (NSL). (A) Spin coating of polystyrene beads, (B) Metals deposition, (C) Lift off, (D) Single hexagonal nanosandwich array.

Figure 3.2A and 3.2B show Scanning Electron Microscope (SEM) images of large domains of defect-free packing of polystyrene before and after lift-off. A line profile on AFM (Atomic Force Microscopy) image (Figure 3.2A inset) shows the size of polystyrene to be 500 nm. A line profile from AFM image (Figure 3.2B inset) after liftoff shows that triangular structures is  $\sim 50$  nm in height ( line profile is not shown ), which is in agreement with 50 nm of gold as measured by a quartz crystal microbalance during the deposition process.

A series of Localized Surface Plasmon Resonance (LSPR) extinction spectra demonstrate the wavelength tunability, which depends on controlling the in-plane diameter and out-of-plane height of the component nanoparticles, independently. The chemical composition of the nanoparticles, the substrate, and the surrounding medium are held constant.

The changes of LSPR  $\lambda_{\max}$  with respect to nanoparticle height can be illustrated by comparing the LSPR spectra in Figure 3.2C. The spectra of nanoparticles with identical shapes and values of the diameter but different height of 50, 30 and 20 nm depict a red shift of LSPR  $\lambda_{\max}$  of 739.09 nm (Figure 3.2C-1), 763.93 nm (Figure 3.2C-2) and 794.67 nm, (Figure 3.2C-3), respectively. As the

height is decreased, the LSPR shift increases. This shift is due to the increase in magnitude of electromagnetic fields of shorter height nanoparticles.<sup>56a</sup>



**Figure 3.2** (A) SEM image of hexagonal close pack array of polystyrene with diameter of 500 nm. The inset in panel A represents the higher magnification AFM image with scan area of  $1.5 \times 1.5 \mu\text{m}$ . (B) SEM image of nanodot arrays. The inset in panel B represents the high resolution AFM image at  $800 \times 800 \text{ nm}$ . (C) Comparison of LSPR shift spectra of Au nanodot arrays on glass. All spectra were produced from a nanosphere deposition mask ( $D=500 \text{ nm}$ ) with a constant diameter of  $200 \pm 5 \text{ nm}$  and various height of (1) = 50 nm  $\lambda_{\text{max}} = 739.09 \text{ nm}$  (2) = 30 nm  $\lambda_{\text{max}} = 763.93 \text{ nm}$  (3) = 20 nm  $\lambda_{\text{max}} = 794.67 \text{ nm}$ .

The control experiments to verify our LSPR results include investigation of the silver (Ag) nanodots and its metal/insulator/metal (MIM) forms with LSPR. The LSPR  $\lambda_{\text{max}}$  change of Ag nanoparticle with the change in the height and layer components is shown in Figure 3.3. The spectra indicate the red shift due to the varied height and different metal-insulator-metal layers. Figure 3.3A shows Ag nanodots with two different heights from 50 (red peak) to 25 nm (blue peak), leading to a red shift of  $\lambda_{\text{max}}$  from 527 to 569 nm. This shift is due to higher magnitude of

electromagnetic fields of nanoparticles of shorter height compared to the ones of larger height.<sup>56a</sup>

As the height of nanostructures gets thinner, the extinction decreases with respect to the absorption of incident light, as expected. Figure 3.3B shows the LSPR  $\lambda_{\max}$  of single layer nanodots compared with metal-insulator-metal (MIM) sandwiches. The LSPR of the Ag nanodots and MIM results in a 106 nm red shift. The LSPR  $\lambda_{\max}$  of 50 nm Ag nanodots was 527 nm, while the LSPR  $\lambda_{\max}$  of 60 nm MIM nanosandwiches (20/20/20 nm of Ag/Al<sub>2</sub>O<sub>3</sub>/Ag) was 633 nm. Ag nanodots that generate these peaks have identical shapes and diameters but vary in height and composition of nanostructures.

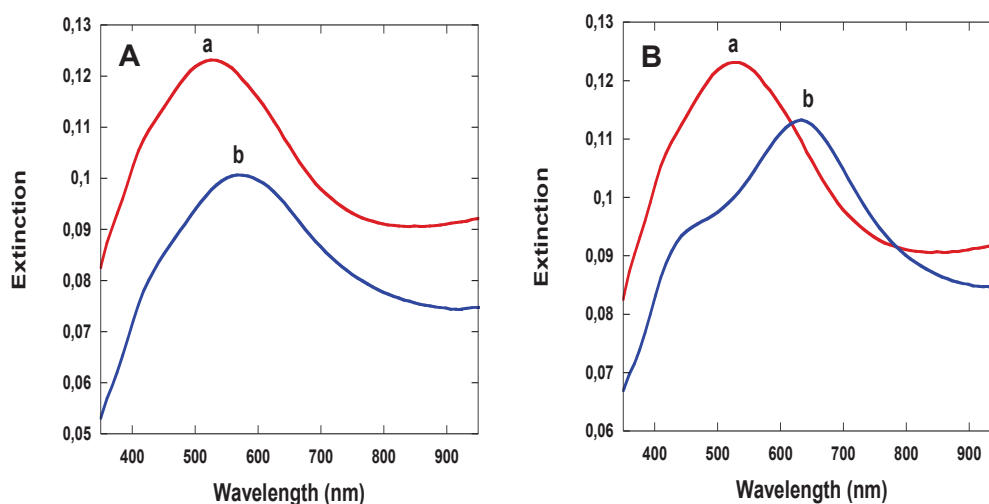


**Figure 3.3** The LSPR shift peaks between (A) 50 nm Ag nanodot array (a) with  $\lambda_{\max}=527$  nm and 25 nm Ag nanodot array (b) with  $\lambda_{\max}=569$  nm. (B) The LSPR shift spectra shows the different between 50 nm Ag nanodot array with  $\lambda_{\max}=527$  nm (a) and 20 nm Ag / 20 nm Al<sub>2</sub>O<sub>3</sub> / 20 nm Ag nanosandwich array with  $\lambda_{\max}=633$  nm (b).

Not only the height of nanostructures changes the LSPR spectra but also their lengths have significant effect in LSPR spectra. All the nanostructure arrays in this study were prepared using 500 nm diameter nanosphere mask. However, we also examined the larger particles with diameter of 1  $\mu\text{m}$  to investigate the changes in LSPR measurement with particle size. The effect of changing nanoparticle diameter for a constant composition, shape and height is shown in Figure 3.4. These

nanostructures have identical shapes and constant out-of-plane height but different in-plane diameter from 200 to 400 nm. Increasing the size of the PS nanosphere mask shifted the UV-Vis extinction into the infrared region, as expected. A 311 nm red shift can be seen in Figure 3.4. From the LSPR measurements we could clearly observe that when nanosphere diameter increased, the size of triangle nanodots increased, which led to the LSPR shift to higher wavelength. This shift is due to higher magnitude of electromagnetic fields of wider nanoparticles compared to the ones of narrower nanoparticles.<sup>56a</sup>

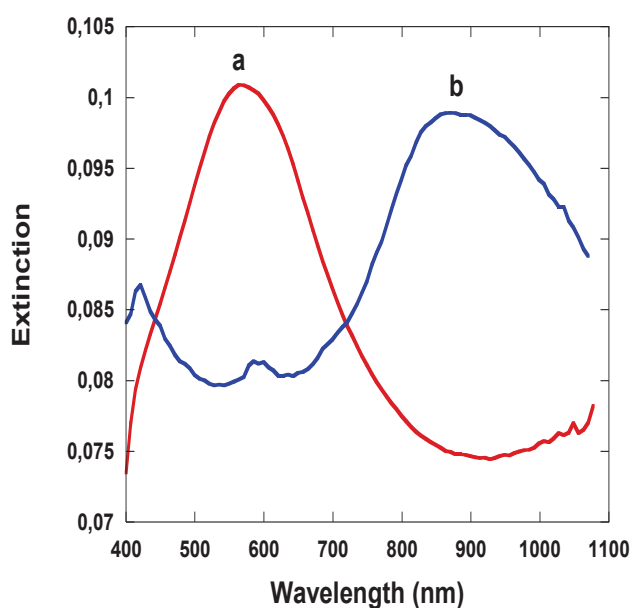


**Figure 3.4** Comparison of LSPR shift for 25 nm Ag nanodot array with different polystyrene diameter corresponding to (a)  $D= 500$  nm (b)  $D=1000$  nm.

### 3.2 Analysis of Single Layer Nanodot Arrays Conjugated Polymer

The nanodot arrays before and after conjugation with polymer were analyzed using AFM. The corresponding tapping mode AFM images are shown in Figure 3.5. Figure 3.5A displays an AFM image of typical gold nanodot arrays on a glass / Si substrate. The Au nanotriangles have in-plane widths of  $\sim 200$  nm and out-of-plane heights of  $\sim 50$  nm as determined by line profiles from AFM images. Figure 3.5B shows the surface morphology of the same nanodots after treatment with thiolated

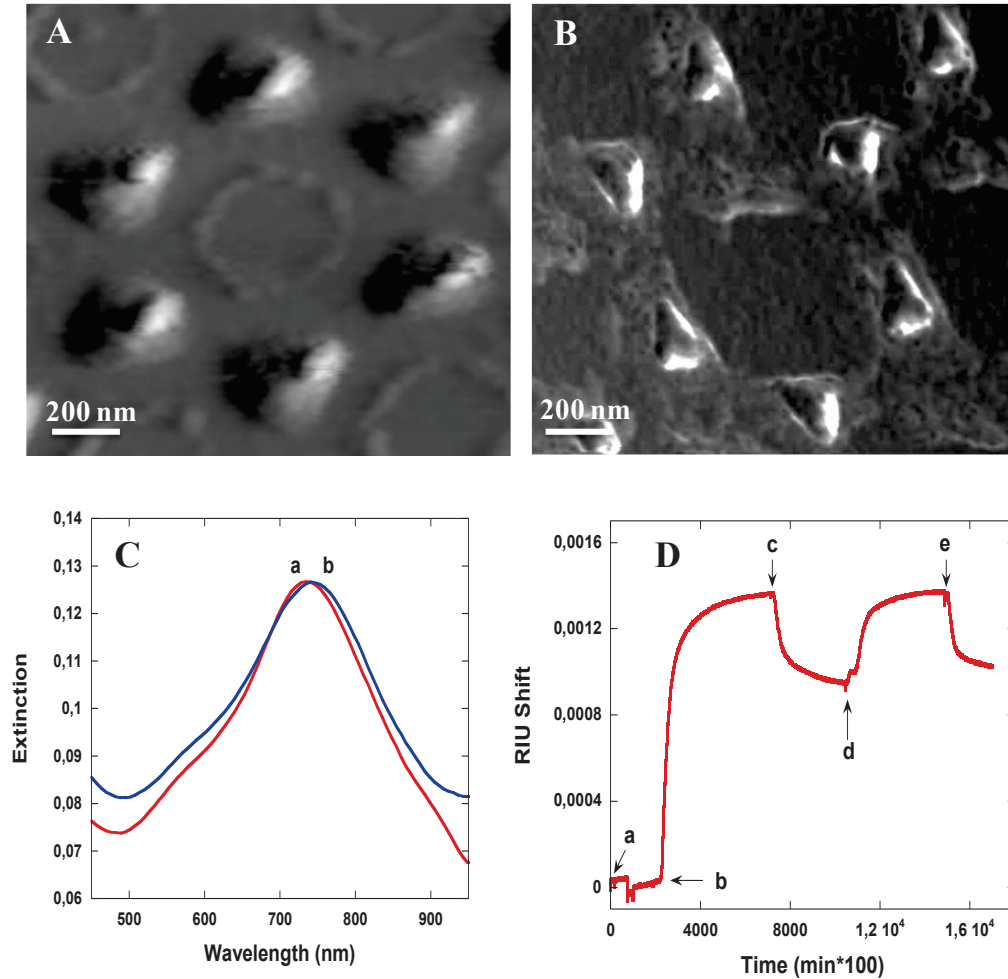
polymer solution, pyridyldisulfide (PDS)-functionalized poly(MEO<sub>2</sub>MA) (M<sub>n</sub> of 3200 g/mol). This image clearly shows that the polymer molecules are completely bound to the side and top of the nanodots.

Figure 3.5C displays LSPR extinction spectra of triangular Au nanodot arrays on glass substrates with an in-plane diameter of 200 nm and out-of-plane height of 50 nm before and after polymer functionalization. The LSPR  $\lambda_{\text{max}}$  of the unfunctionalized Au nanodots was measured to be 729.53 nm and after conjugation with polymers shifted to 736.16 nm. A 6.3 nm red shift indicates the binding of the polymer to the Au nanodot surfaces. Both the LSPR spectra and AFM images have demonstrated well the specific binding of the PDS-functionalized polymer to the nanodots on silicon and glass substrate.

Surface Plasmon Resonance (SPR) technique was used to verify the surface coverage and binding affinity of PDS-functionalized polymer onto the gold surface. In this experiment water was used: 1) to establish an initial steady baseline and 2) to remove loosely bound molecules after each flow regime. The amount of wavelength shift (nm) correlates to the amount of polymer attached on the surface. Figure 3.5D shows polymer adsorption on a clean gold sensor. A sharp increase in the SPR wavelength is observed upon introducing polymer solution to the sensor (b), corresponding to an increase in polymer adsorption by the sensor surface. The decline in SPR wavelength during the water rinse is due to the removal of the unbound polymers (c and e). The second injection (d) of polymer over the sensor surface leads to the second sharp increase in the SPR wavelength as a result of the more polymer binding. Introduction of sample solutions in all two flow regions leads to a sharp increase in SPR wavelength, indicating the binding of respective molecules on the gold sensor. The difference in SPR wavelength between the initial baseline and the baseline after each water rinse reflects the amount of bindings at each step.

The net refractive index unit (RIU) shift was measured and used to calculate the thickness of thiol-terminated polymer on the Au surface. The thickness was found to be 3,56 nm, in good agreement with theoretical calculations and values reported in literature.<sup>74</sup> SPR measurements of the adsorption of polymer solution

onto a bare gold (Au) surface showed a surface coverage of  $275.6 \text{ ng/cm}^2$  ( $\sim 1.6 \cdot 10^{14}$  PDS-polymer / $\text{cm}^2$ )



**Figure 3.5** (A) Tapping mode AFM image of 50 nm Au nanodot arrays on silicon substrate. (B) AFM image of thiol terminated polymer functionalized Au nanodot arrays. (C) Comparison of LSPR shift between (a) 50 nm Au nanodot array  $\lambda_{\text{max}}=729.53 \text{ nm}$  and (b) Au nanodot array after thiol terminated polymer conjugation  $\lambda_{\text{max}}=736.16 \text{ nm}$  on glass substrates. (D) SPR sensogram of thiol terminated polymer on gold coated glass.

### 3.3 Nanostructure (Nanosandwiches) Arrays Conjugate with Temperature Responsive Polymers

In order to improve our LSPR system performance, we started nanostructure with various shape and size for a sensitive and fine-tuned LSPR spectrum. To do this, we run a series of experiments on nanostructure arrays with different thickness layers for LSPR measurements.

Before the surface functionalization with polymers, the thickness of nanostructure was controlled in this section. We investigated two height dependent nanostructures of 20 nm Au / 20 nm Al<sub>2</sub>O<sub>3</sub> / 20 nm Au and 30 nm Au / 30 nm Al<sub>2</sub>O<sub>3</sub> / 30 nm Au. Figure 3.6 shows the LSPR spectra of nanosandwich arrays with different thicknesses. First sample consists of 30 nm MIM on glass substrate (blue peak) and second sample is 20 nm MIM (red peak). The LSPR  $\lambda_{\max}$  of the red peak is located at 743.23 nm and blue peak is measured to be 831.37 nm. A 88.14 nm red shift is due to the decrease in height. As the samples get thinner, the extinction of incident light decreases, as seen in Figure 3.3A.

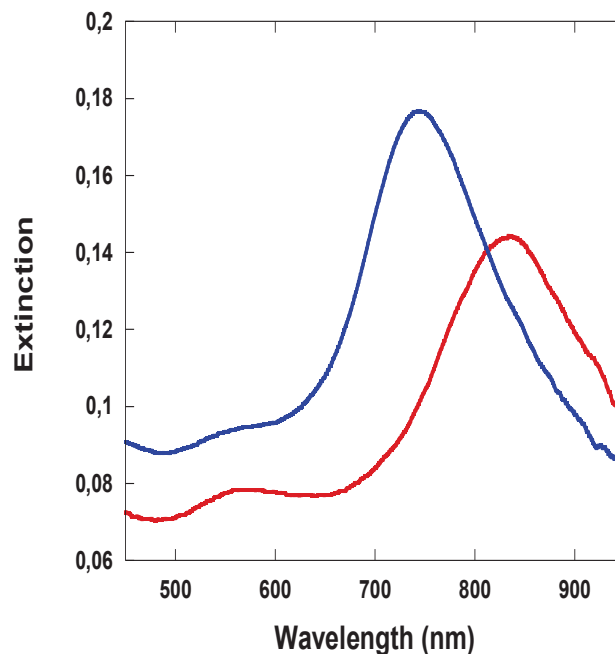


**Figure 3.6** Comparison of LSPR shift between 90 nm (blue peak) and 60 nm MIM (red peak) nanosandwiches.

The conjugation of polymeric and biological molecules to nanostructure (nanosandwiches) arrays is illustrated in this section of thesis. The thiolated polymer was conjugated to the gold layers of nanosandwiches and the optical properties and morphology of these nanostructures were then investigated by LSPR and AFM, respectively (Figure 3.7). Figure 3.7A shows the schematic representation of thiolated polymer binding onto Au layers. The AFM images of nanosandwich array (Au / Al<sub>2</sub>O<sub>3</sub> / Au) can be seen in Figure 3.7B and 3.7C. Figure 3.7B shows unfunctionalized nanosandwich arrays. The average nanosandwich height was measured to be 55 nm. Remarkably, rings can be seen in the surrounding of unfunctionalized nanosandwiches arrays, which is formed from the re-emission of Al<sub>2</sub>O<sub>3</sub> from the center layer of triangular arrays. After incubation with thiol terminated polymers, the average nanosandwich height was measured to be 58 nm (Figure 3.7C). The variation suggests the polymer binding on nanosandwich arrays. The binding of the thiol terminated polymers results from the formation of S-Au covalent bond. In addition, binding of polymers to the gold layer results in the triangles to adopt a more rounded shape.



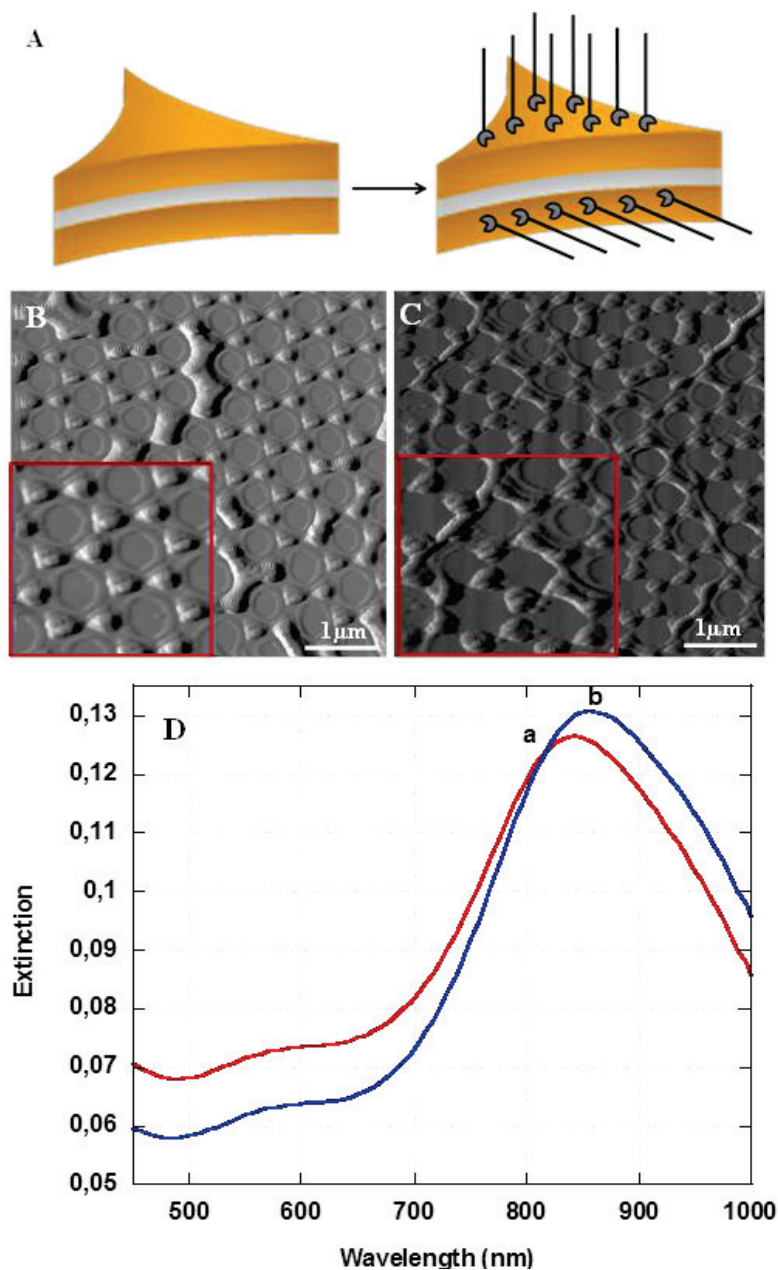


**Figure 3.7** (A) Schematic illustration of the functionalized nanosandwich arrays with thiol terminated polymers to Au layers. (B) Tapping mode AFM images of unfunctionalized and (C) functionalized nanosandwich arrays with thiolated polymers on silicon substrate. Inset images in (B and C) represent the scan area of  $1.5\mu\text{m} \times 1.5\mu\text{m}$ . (D) Comparison of LSPR shift between (a) unfunctionalized  $\lambda_{\text{max}} = 832.24 \text{ nm}$  and (b) functionalized  $20 \text{ nm Au} / 20 \text{ nm Al}_2\text{O}_3 / 20 \text{ nm Au}$  nanosandwich arrays with thiolated polymers  $\lambda_{\text{max}} = 849.66 \text{ nm}$  on glass substrates.

The functionalisation of 20 nm Au / 20 nm Al<sub>2</sub>O<sub>3</sub> / 20 nm Au nanosandwiches with thiol or phosphate terminated polymers were also analyzed by LSPR measurements. The LSPR results are presented in Figure 3.7D. The LSPR  $\lambda_{\text{max}}$  of the unfunctionalized nanosandwich arrays was measured to be 832.24 nm (a). The LSPR  $\lambda_{\text{max}}$  of the nanosandwich arrays modified with the thiol terminated polymers was measured to be 849.66 nm (b) corresponding to a 17.42 nm red-shift.

Schematic illustration of the functionalized nanosandwich arrays with phosphate terminated polymer to Al<sub>2</sub>O<sub>3</sub> layer can be seen in Figure 3.8A. Figure 3.8B and 3.8C depict the comparison of unfunctionalized and phosphate terminated polymer functionalized nanosandwich arrays, respectively. The presence of Al<sub>2</sub>O<sub>3</sub> near the edge and surface of the nanosandwiches can be observed in Figure 3.8C. Moreover, inset image of Figure 3.8C shows that native aluminium oxide (Al<sub>2</sub>O<sub>3</sub>) layers were formed and phosphate terminated polymers were bound to Al<sub>2</sub>O<sub>3</sub> layer near the nanodot array. During the experiments it was noted that wetting properties of Al metal changed the deposition conditions.<sup>217</sup>

In Figure 3.8D, the LSPR  $\lambda_{\text{max}}$  of the unfunctionalized nanosandwich arrays was measured to be 836.6 nm (red peak). The LSPR  $\lambda_{\text{max}}$  of the nanosandwich arrays modified with the phosphate terminated polymers was measured to be 843.13 nm (blue peak) corresponding to a red-shift of 6.53 nm. The LSPR shift observed with the thiolated polymer modified nanosandwich arrays (17.42 nm in Figure 3.7D) was much larger than that of the phosphate terminated polymer functionalized nanosandwich arrays (6.53 nm). This difference is due to the smaller surface area of Al<sub>2</sub>O<sub>3</sub> layer compared to the surface area of Au layers on nanosandwich arrays which leads to the binding of less amount of phosphate-terminated polymer. These conclusions are also parallel with Figure 3.7D. In comparison to the obtained results, the accuracy of data has been proven.

The selectivity of gold-thiol binding was shown by SPR analysis (Figure 3.8E). Three different samples were injected to the Au chip surface; diethyl (3-bromopropyl) phosphonate (DeBrPP), allyltriethoxysilane (ATES) and thiolated polymer. The adsorption was monitored by SPR. The SPR response was obtained only with thiol terminated polymer adsorption, whereas DeBrPP and ATES did not give any response in SPR sensograms. As it can be seen in Figure 3.8E, (a) is the point at which 200  $\mu\text{l}/\text{min}$  deionized (DI) water was injected for 10 min, at (b) 100  $\mu\text{l}/\text{min}$  DeBrPP was injected for 30 min, which was followed by (c) injection of 100  $\mu\text{l}/\text{min}$  ATES for 30 min.

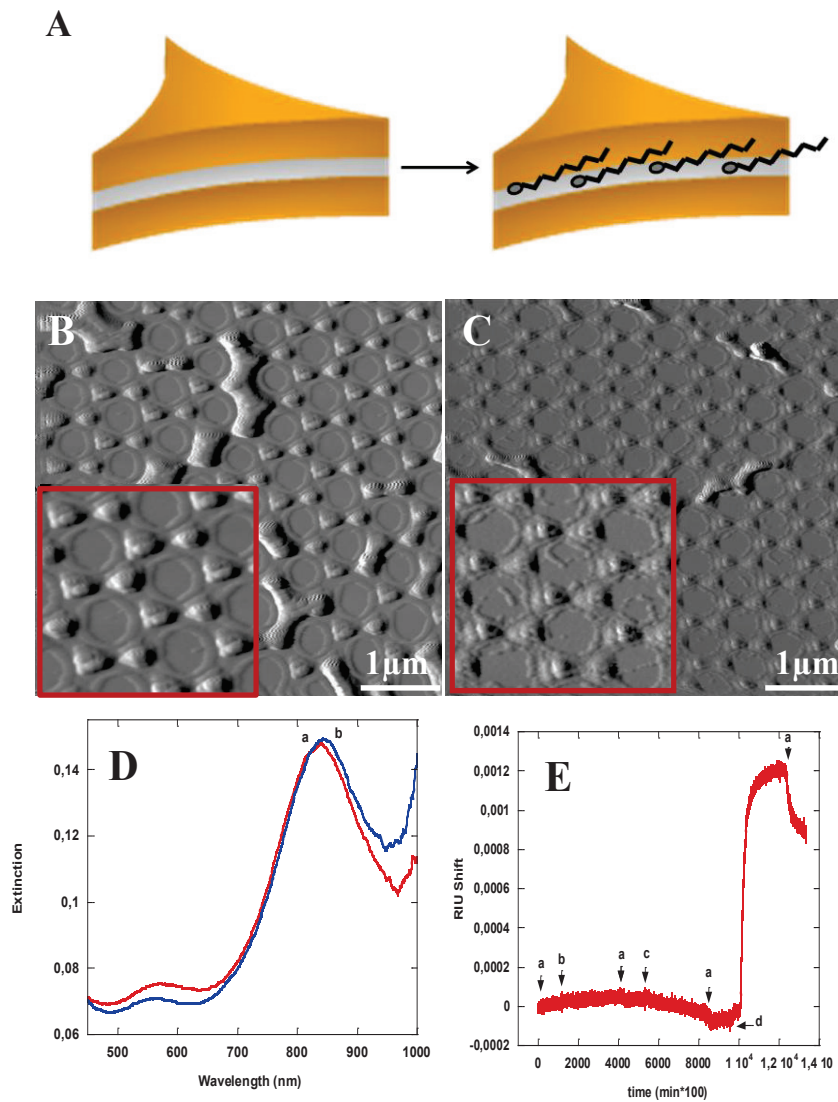
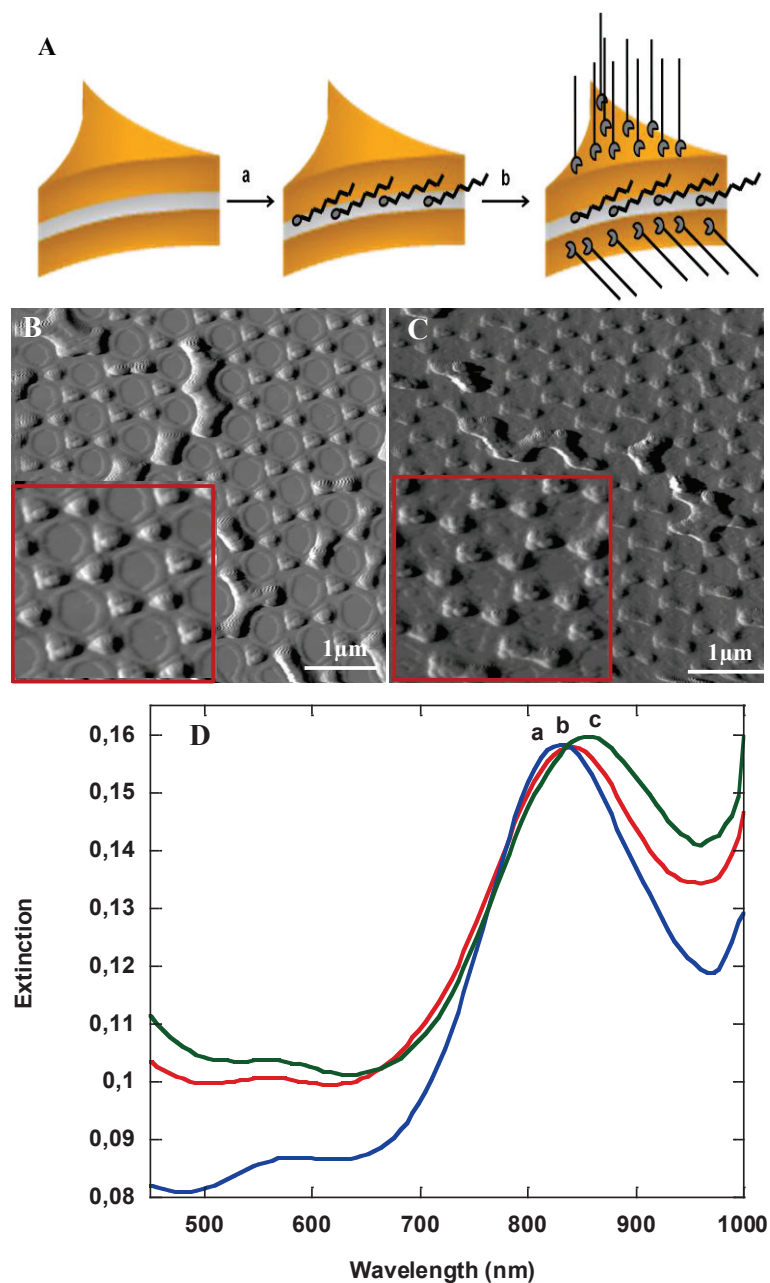


**Figure 3.8** (A) Schematic illustration of the functionalized nanosandwich arrays with phosphate terminated polymer to Al<sub>2</sub>O<sub>3</sub> layer. Tapping mode AFM images of (B) unfunctionalized and (C) phosphate terminated polymer functionalized nanosandwich arrays on silicon substrate. Inset images in B and C represent the scan area of 1.5 μm x 1.5 μm. (D) Comparison of LSPR shift between (a) unfunctionalized  $\lambda_{\max} = 836.6$  nm and (b) functionalized 20 nm Au / 20 nm Al<sub>2</sub>O<sub>3</sub> / 20 nm Au nanosandwich arrays with phosphate terminated polymer  $\lambda_{\max} = 843.13$  nm on glass substrates. (E) SPR sensogram of non-specific and specific binding events.

Figure 3.9A (a-b) shows schematically the binding process of both phosphate and thiol terminated polymers on nanosandwich arrays. First, the phosphate terminated polymer was bound to  $\text{Al}_2\text{O}_3$  layer and then thiol terminated polymer was attached to Au layers. In addition to individual binding of polymers in Figures 3.7C and 3.8C, the functionalization of all layers of nanosandwich arrays with both polymers is shown in Figure 3.9C. The binding of thiol and phosphate terminated polymers to Au and  $\text{Al}_2\text{O}_3$  layers, respectively, is specific to metal and occurs through chemical bonding.

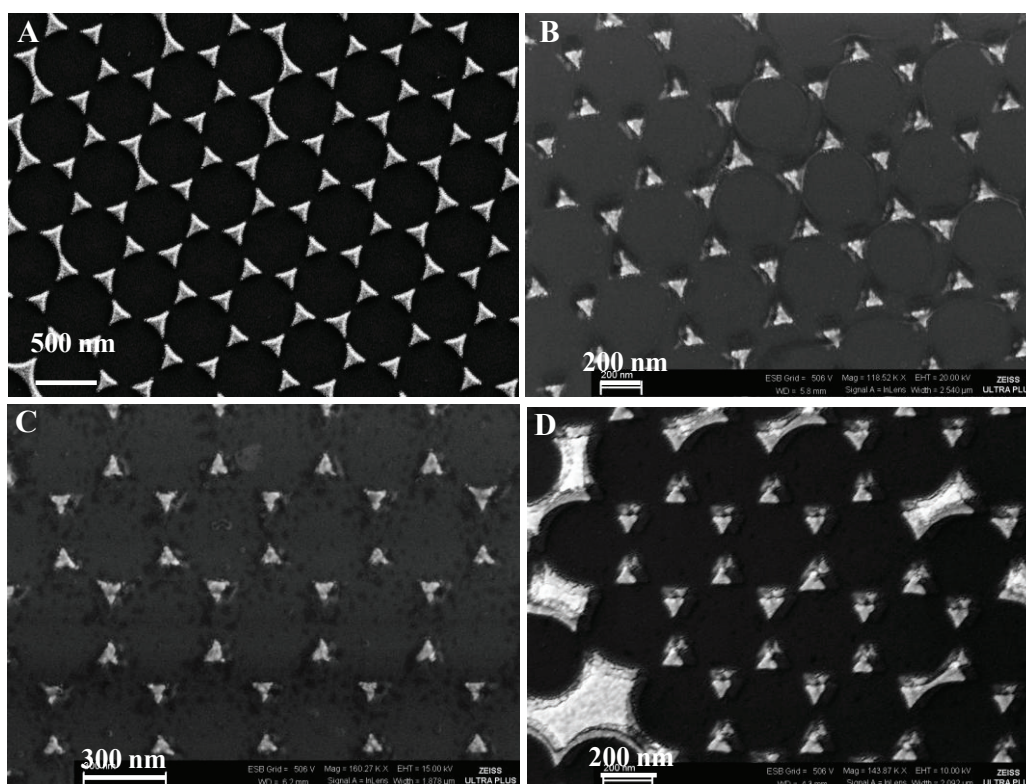
Figure 3.9D shows the LSPR  $\lambda_{\text{max}}$  of the nanosandwich arrays after having each layer functionalized with polymer. The LSPR  $\lambda_{\text{max}}$  of the unfunctionalized nanosandwich arrays was measured to be 831.37 nm (a). In order to carry out the specific binding of phosphate-terminated polymer to  $\text{Al}_2\text{O}_3$  layer, the sample was incubated with the respective polymer solution for 24 hours. After gently rinsing with absolute ethanol and drying under nitrogen ( $\text{N}_2$ ) stream, the LSPR  $\lambda_{\text{max}}$  was measured to be 838.78 nm (b). The LSPR  $\lambda_{\text{max}}$  change corresponded to a 7.41 nm red-shift compared with unfunctionalized nanosandwich arrays, indicating efficient polymer adsorption, was in good agreement with the result presented in Figure 3.8D. Next, the array sample was incubated with the thiol terminated polymer solution for 24 hours to allow the binding of the polymer to the bottom and top Au layers of the nanosandwiches. After gently rinsing and drying, the LSPR  $\lambda_{\text{max}}$  of the nanosandwich arrays was measured to be 853.13 nm corresponding to a 14.35 nm red-shift (c). The results indicate that the functionalization of nanosandwich layers individually with polymers exhibited a larger extinction shift in comparison to the functionalisation of all layers. This result may be attributed to alterations in the nanosandwich arrays surrounding local dielectric environment as well as the steric hindrance effects of polymers chains bound. Moreover, dipole and quadrupole peaks are located approximately at 831.37 nm and 555 nm, respectively. Upon exposure to polymers, the dipole peak shifts to 853.13 nm as quadrupole peak remains constant (Figure 3.9D).

In addition to the interpretation of Figure 3.7D and 3.8D, the functionalisation of individual layer of the nanosandwich arrays exhibit a larger extinction shift in comparison to the the functionalisation of all layers. This result can be attributed to alteration in the nanosandwiches local dielectric environment and surrounding refractive index. These results is in good agreement with theoretical studies. According to this studies the electromagnetic field strength at the nanotriangle surface is more intense which is due to larger LSPR shifts and having larger electromagnetic field too.<sup>218</sup>



**Figure 3.9** (A) Schematic illustration of the functionalized nanosandwiches with thiol and phosphate terminated polymer to Al<sub>2</sub>O<sub>3</sub> and Au layers. Tapping mode AFM images of (B) unfunctionalized and (C) functionalized nanosandwich arrays with thiol and phosphate terminated polymers. Inset images in B and C represent the scan area of 1.5 μm x 1.5 μm. (D) Comparison of LSPR shift of (a) unfunctionalized  $\lambda_{\max} = 831.37$  nm (b) after functionalization of nanosandwich arrays with phosphate  $\lambda_{\max} = 838.78$  nm (c) thiol and phosphate terminated polymers  $\lambda_{\max} = 853.13$  nm.

From above mentioned results the adsorbate-induced local refractive index changes with respect to the charge-transfer interactions at the surfaces of nanodots lead to wavelength shifts in LSPR instead of electromagnetic coupling of the nanodots. The signal transduction mechanism in this nanosensor is a reliably measured wavelength shift rather than an intensity change as in many previously reported nanoparticle-based sensors. In addition to these inferences, an electrodynamic study demonstrated that the more redshifted plasmon resonances gave larger peak shifts, it can be seen in our study, as well.<sup>218</sup>



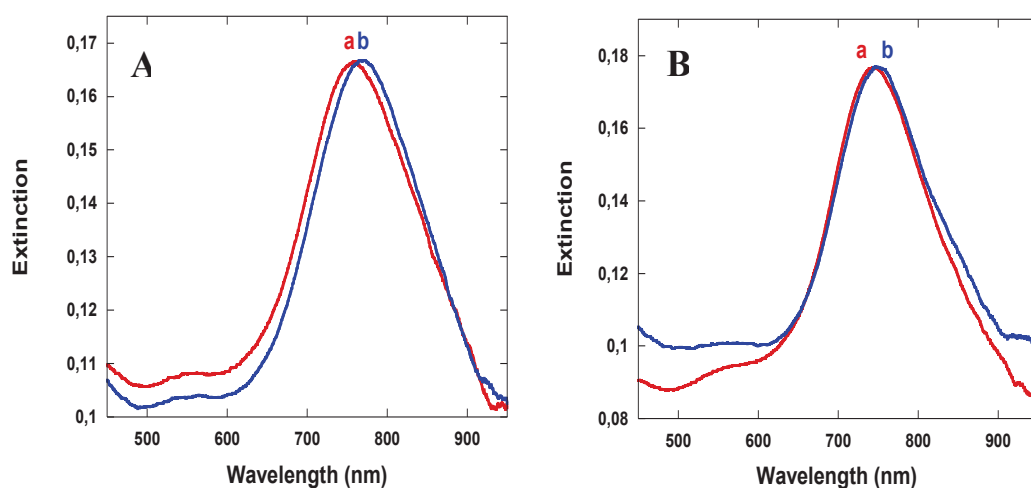
**Figure 3.10** SEM images of unfunctionalized (A) and functionalized nanosandwich arrays with thiol terminated polymer (B), phosphate terminated polymer (C), thiol and phosphate terminated polymers (D).

Figure 3.10 shows the electron micrograph results of Au/Al<sub>2</sub>O<sub>3</sub>/Au (before and after functionalized with polymers) experiments. Figure 3.10A is the sample that not interacted with polymers, the height and sizes of the dots indicated no absorption



or no binding. Figure 3.10B reveals that the phosphate terminated polymer bound to  $\text{Al}_2\text{O}_3$  as can be observed in SEM image. The only problem with the SEM images is the effect of the beam on the polymers and so we tried to use low KV to get proper images. Figure 3.10C shows that the thiolated polymer completely bound to the nanodots as seen in SEM image. Finally, the binding events of all polymers to nanodots were investigated by SEM image as shown in Figure 3.10D. These SEM images were in good agreement with LSPR.

In addition to these experiments, other nanosandwich arrays, which is composed of 30 nm Au / 30 nm  $\text{Al}_2\text{O}_3$  / 30 nm Au, were functionalized with polymers (thiol and phosphate terminated) to demonstrate accuracy of the results.



**Figure 3.11** Comparison of LSPR shift between (A) unfunctionalized 30 nm Au / 30 nm  $\text{Al}_2\text{O}_3$  / 30 nm Au nanosandwich array (blue peak)  $\lambda_{\text{max}} = 751.06$  nm and after thiol terminated polymer binding to nanosandwich array (red peak)  $\lambda_{\text{max}} = 770.09$  nm (B) unfunctionalized 30 nm Au / 30 nm  $\text{Al}_2\text{O}_3$  / 30 nm Au nanosandwich array (blue peak)  $\lambda_{\text{max}} = 743.23$  nm and after phosphate terminated polymer binding to nanosandwich array (red peak)  $\lambda_{\text{max}} = 748.96$  nm on glass substrates.

Similar to Figure 3.7 and 3.8, the 30 nm Au / 30 nm  $\text{Al}_2\text{O}_3$  / 30 nm Au nanosandwich arrays were functionalized with thiol and phosphate-terminated

polymers, individually. In Figure 3.11A, the LSPR  $\lambda_{\max}$  of the unfunctionalized nanosandwich array was measured to be 751.06 nm (as shown in blue peak). The nanosandwich arrays were then modified with the thiol terminated polymer and the LSPR  $\lambda_{\max}$  was measured to be 770.09 nm corresponding to 19.03 nm red-shift (as shown in red peak). This shift value is different than the one observed in Figure 3.5 due to alteration in the nanosandwich array local dielectric environment and component of multilayer in contrast with single layer.

In the same manner, in Figure 3.11B, the LSPR  $\lambda_{\max}$  of the unfunctionalized multilayer nanosandwich array was measured to be 743.23 nm (as shown in blue peak). The nanosandwich arrays were then modified with the phosphate terminated polymer and the LSPR  $\lambda_{\max}$  was measured to be 748.96 nm corresponding to 5.73 nm red-shift (as shown in red peak). The LSPR shift induced from thiol terminated polymer was larger than that induced by phosphate terminated polymer on nanosandwich arrays. This was attributed to the smaller area of  $\text{Al}_2\text{O}_3$  layer at which the phosphate terminated polymer bound when compared to the area of Au layers where thiol terminated polymer attached to.

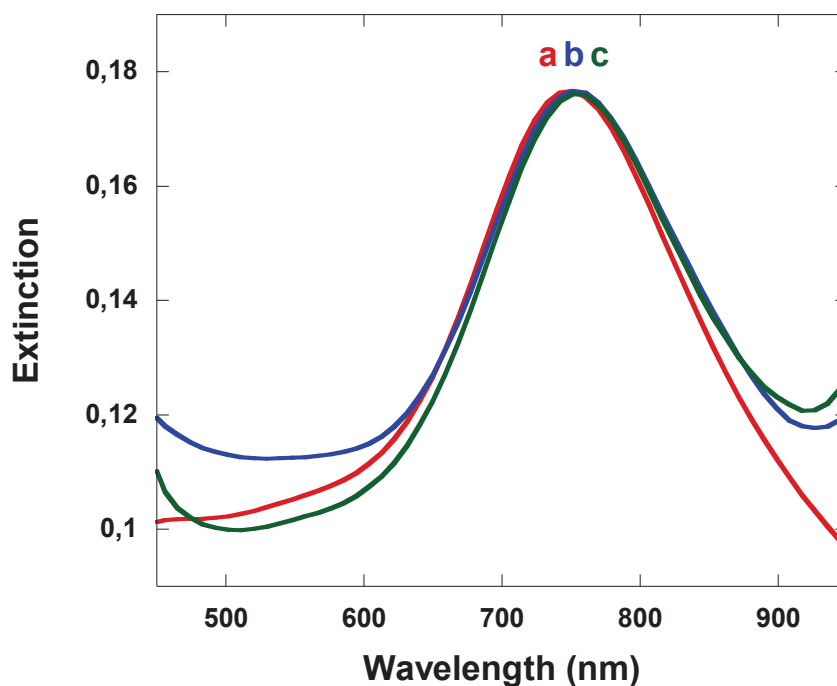


**Figure 3.12** Comparison LSPR shift between 30 nm Au / 30 nm Al<sub>2</sub>O<sub>3</sub> / 30 nm Au nanosandwich arrays (A) unfunctionalized  $\lambda_{\max} = 741.02$  nm. (B) after functionalization of nanosandwich arrays with phosphate terminated polymer  $\lambda_{\max} = 746.31$  nm. (C) thiol and phosphate terminated polymers  $\lambda_{\max} = 749.84$  nm.

In Figure 3.12, the LSPR  $\lambda_{\max}$  of the MIM nanosandwich arrays were recorded after each surface functionalization step. First, the LSPR  $\lambda_{\max}$  of the unfunctionalized nanosandwich array was measured to be 741.02 nm (Figure 3.12-A). In order to conjugate the specific polymer to middle Al<sub>2</sub>O<sub>3</sub> layer, the sample was incubated in the phosphate terminated polymer solution for 24 hours. After rinsing and drying with N<sub>2</sub> gas, the LSPR  $\lambda_{\max}$  with the polymer was measured to be 746.31 nm (Figure 3.12-B). The LSPR  $\lambda_{\max}$  shift corresponding to this surface functionalization step was a 5.29 nm red-shift with regard to unfunctionalized MIM nanosandwich arrays. Next, the sample was incubated in the thiol terminated polymer solution for 24 hours to conjugate the specific polymer to the bottom and top Au layers. Again, after rinsing and drying with N<sub>2</sub> gas, the LSPR  $\lambda_{\max}$  of surface modification with the polymer was measured to be 749.84 nm corresponding to 3.53 nm red-shift (Figure 3.12-C). Moreover, the dipole and quadrupole peaks were located approximately at 741.02 nm and 550 nm, respectively. Upon exposure to

polymers, the dipole peak shifted to 749.84 nm as quadrupole peak remained constant (Figure 3.12). After binding polymer to nanosandwiches, the Au sample provided smaller LSPR shift this response is due to changes in the electromagnetic field strengths surrounding the nanosandwiches and also the polymer packing density.

After Au / Al<sub>2</sub>O<sub>3</sub> / Au nanosandwiches, the functionalisation of 30 nm Au / 30 nm HfO<sub>2</sub> / 30 nm Au nanosandwiches with silane terminated polymers were analyzed by SEM, AFM and LSPR, respectively.

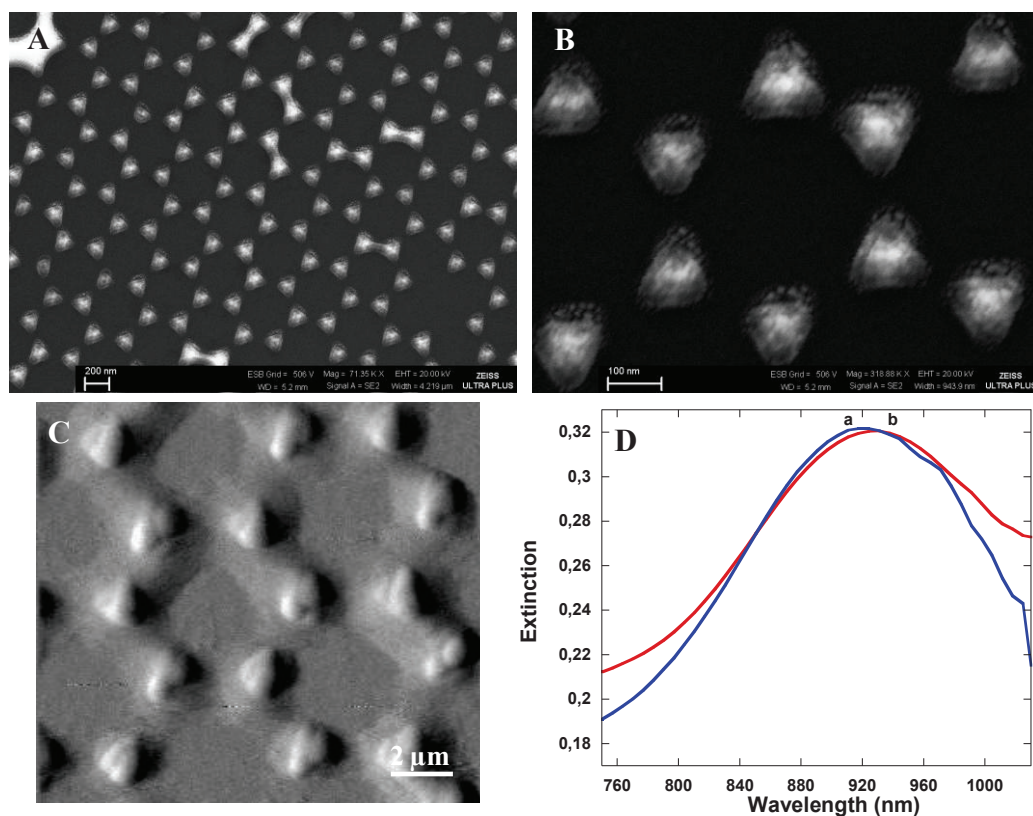


**Figure 3.13** (A, B) SEM images of functionalized 30 nm Au / 30 nm HfO<sub>2</sub> / 30 nm Au nanosandwich arrays with silane terminated polymers. (C) Tapping mode AFM image of functionalized nanosandwich arrays with silane terminated polymers. (D) Comparison of LSPR spectra between unfunctionalized (a)  $\lambda_{\max}$  = 918.8 nm and functionalized with silane terminated polymers (b)  $\lambda_{\max}$  = 928.8 nm.

To investigate the morphology of nanosandwiches arrays (Au / HfO<sub>2</sub> / Au) the SEM and AFM were conducted. Figure 3.13(A and B) illustrated the low and high magnification images of nanosandwiches. The image in Figure 3.13B reveals that almost all nanosandwiches after interact with silane terminated polymers seems to be covered. To improve this issue AFM was applied to get higher resolution image for observation the binding process in detail. The AFM image (Figure 3.13C) illustrated that the nanosandwiches all were covered with polymers in which the shape of these structures became smaller with compare to unfunctionalized nanosandwiches.

LSPR measurement was presented in Figure 3.13D. The LSPR  $\lambda_{\max}$  between the unfunctionalized (a) and functionalized (b) nanosandwich arrays shows the total shift of 10 nm. A 10 nm red-shift in HfO<sub>2</sub> spectrum was smaller than the shift from thiolated polymer in nanosandwich arrays (Figure 3.11A). This small shift is due to the smaller surface area of HfO<sub>2</sub> layer compared to the surface area of Au layers on nanosandwich arrays which leads to decreased in the silane-terminated polymer.

### 3.4 Investigation of Polymer Phase Transition on Nanosandwich Arrays

Temperature-responsive polymers are polymers that respond with large physical changes to small temperature changes in their environment. Typically, when the polymer is stimulated by a temperature increase above a critical temperature, the polymer chain in solution shows conformational changes and phase separation. Similarly, the surface-adsorbed or grafted polymer chains collapse, when they are stimulated by a temperature increase, converting the interface from hydrophilic to relatively less hydrophilic state. The temperature at which the phase transition (chain collapse) occurs is called lower critical solution temperature (LCST).<sup>219</sup> The transition is reversible (i.e. the chains return to their extended conformation when temperature is decreased below LCST, and the reversible transition can be repeated numerous times by changing the temperature above and below LCST. The LCST of the polymers can be adjusted over a wide temperature range simply by introducing

hydrophilic or hydrophobic components into the temperature-responsive polymer structure. Poly(N-isopropyl acrylamide) and poly(ethyleneglycol methylether (meth)acrylate) polymers are well-known temperature responsive polymers with tunable LCST values at temperatures practical for biological applications (i.e. between 10°C and 50°C). Poly(ethylene glycol) (PEG) based temperature-responsive polymers show also non-fouling (protein-repellent) properties. These PEG based temperature responsive polymers were used to modified the nanosandwiches for biosensor application in this thesis.<sup>220</sup>

Figure 3.14A schematically shows the nanosandwich arrays having Au layers functionalized with thiol-terminated polymer at its expanded (a) and collapse (b) states. Figure 3.14B depicts the extinction spectra shifts of the thiol-terminated polymer-coated Au nanosandwich arrays (30 nm Au / 30 nm Al<sub>2</sub>O<sub>3</sub> / 30 nm Au) below (b) and above (c) the LCST of the polymer. The LSPR  $\lambda_{\text{max}}$  of unfunctionalized nanosandwich arrays was first measured to be 757.77 nm (a). After the functionalization with the thiol-terminated polymers, the LSPR  $\lambda_{\text{max}}$  of nanosandwich arrays was recorded to be 770.09 nm (b). As the surface was heated up to 45°C, a red shift in the LSPR wavelength from 770.09 nm to 781.51 nm was observed (c), possibly due to the increase in the polymer density close to the nanosandwiches. This red-shift of approx. 10 nm was attributed to the collapse state of the polymer, causing an increase in the refractive index of the surrounding medium. As well-known in the literature,<sup>95</sup> the temperature-responsive polymers used in this study undergo a reversible phase transition from a hydrophilic expanded state to a hydrophobic collapsed state when the temperature is increased above its LCST. These conformational changes lead to variations in the optical properties of nanostructures.

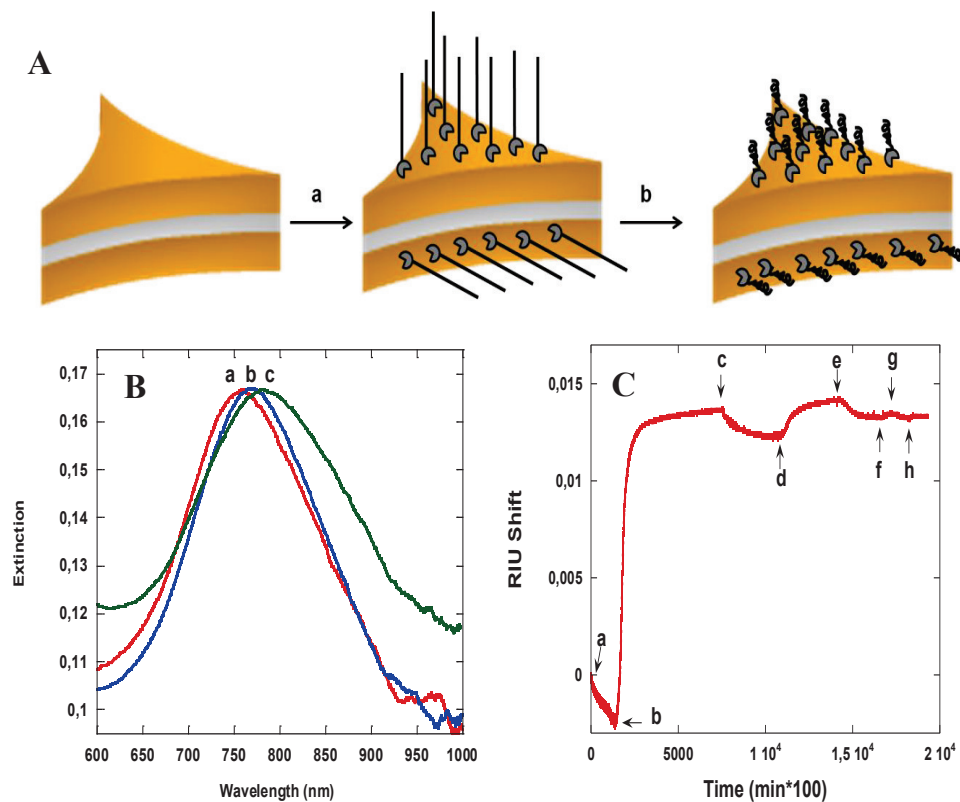


**Figure 3.14** (A) Schematic illustration of the functionalized nanosandwich arrays with thiol terminated polymer above the LCST. (B) LSPR results of (a) unfunctionalized and (b) functionalized nanosandwich arrays with thiol terminated polymer at below LCST (25°C) and (c) above LCST (45°C). (C) SPR sensogram of the adsorption and temperature-responsive behaviour of polymer.

The main purpose of the SPR Spectroscopy technique was to monitor both the adsorption and thermoresponsive behaviour of the thin polymer films which were formed. The analysis involved using 0.1 mM concentrated polymer, followed by multiple injections of hot water. Before the main experiments could be carried out, it was important to rule out any extraneous causes which would result in an increase in the signal level when the hot water is injected. The hot water itself will possess a higher refractive index than cold water and it was important to see whether a change in the water temperature would cause a shift in the signal level. Since the hot water injections will pursue the polymer injections, there is the possibility that a small amount of polymer is still being injected which would cause the signal shift. This can be investigated by injecting cold water. If cold water produces similar shifts to hot

water, then the signal shift cannot be attributed to the thermoresponsive behaviour of the polymer.

The first control experiment carried out involved injecting water at different temperatures to see the effects it has on the sensogram. The hot water control (Figure 3.15) shows that there is no change in the sensogram and so the water temperature itself does not influence the signal level.

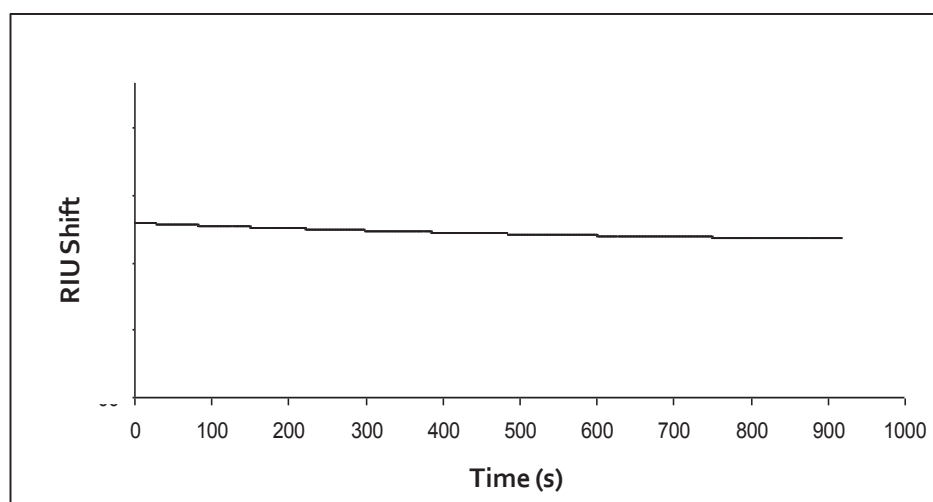


**Figure 3.15** The hot water injection on gold substrate as control experiment.

The thiol terminated polymer solution (0.1 mM) was injected followed by numerous hot water (~40°C) injections. The resulting sensogram shows the formation of a thin polymer film due to a shift in the signal level (Figure 3.14C). The reference signal was obtained by DI water injection (a). The polymer solution was injected to chip surface (b and d) to reach the saturation point. The adsorption of the polymer to the gold surface was followed by the cold water rinse (c, e and g), The following injections (f and h) were hot water at 55°C which was above the LCST of the polymer (40°C). The sensogram shows a series of signals which are much larger compared to the cold water injections and also do not dissipate when compared to the



cold water runs (see Figure 3.14C, f-h). These signals are therefore a direct result of the thermoresponsive behaviour of the thin polymer film.

In order to show the stability of the system, the sensogram of the 0.1 mM sample was left running with water overnight. The result showed that the signal dropped to the original injection level which supported the claim of the stability and also the presence of the thin polymer film. If the polymers were not chemisorbed onto the gold surface, the signal would have been expected to fall down to the starting point which it did not.

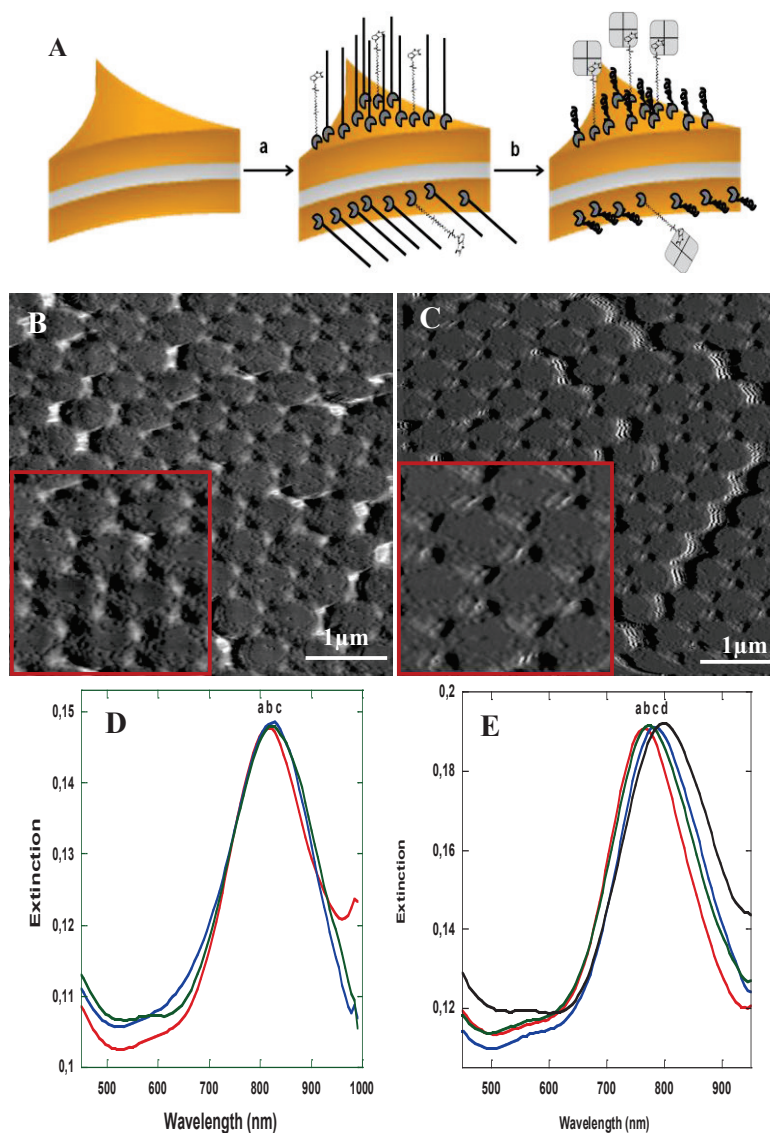
### **3.5 Analyses of Bioaffinity Binding to Nanosandwich Arrays Functionalized with a Mix of Thiol-Terminated Polymer**

Figure 3.16A schematically demonstrates the binding event of (a) mixed SAM (thiol-terminated polymer+EZ-Link HPDP-Biotin) and (b) streptavidin (SA) interaction above the LCST of the polymer on nanosandwich arrays. Figure 3.16B and 3.16C show AFM images of the mixed SAM before and after streptavidin (SA) binding above the LCST of the polymer (45°C). The polymer morphology changed depending on the temperature being below or above the LCST. The height of the polymer chains decreased upon heating, leading to the binding of SA molecules to biotin molecules, as clearly observed in AFM images.

The LSPR spectra presented in Figure 3.16D display that SA molecules did not bind to the mixed SAM (containing thiol terminated polymer and EZ-Link HPDP-Biotin at a mol ratio of 9:1) when the temperature was below the LCST of the polymer (room temperature). LSPR  $\lambda_{\max}$  of the unfunctionalized nanosandwich array was measured to be 816.11 nm (a). After incubation of the polymer and biotin mixture (0.1 mM) for 24 h, the LSPR analysis of the nanosandwich array showed a LSPR  $\lambda_{\max}$  of 822.22 nm (b). A red-shift of 6,11 nm was observed due to the binding

of the mixed SAM to nanosandwich array. After the substrate was incubated with SA (2  $\mu\text{M}$ ) in PBS (Phosphate-Buffered Saline) for 30 min, the LSPR  $\lambda_{\text{max}}$  was measured to be only 823.88 nm (c). Such a small shift (1.66 nm) corresponds to the instrumental noise or non-specific binding of SA molecules.

The LSPR spectra in Figure 3.16E display the shifts observed with the unfunctionalized and functionalized nanosandwich arrays (30 nm Au / 30 nm  $\text{Al}_2\text{O}_3$  / 30 nm Au). The LSPR  $\lambda_{\text{max}}$  of the unfunctionalized nanosandwich array (red peak) was measured to be 765.28 nm (a). After functionalization, LSPR  $\lambda_{\text{max}}$  showed an increase to 772.22 nm (b). A 6.94 nm red-shift was attributed to the binding of polymer mixture. The mixed SAM coated nanosandwich array was then heated above the LCST (45°C) and LSPR  $\lambda_{\text{max}}$  was recorded to be 781 nm (c). A red-shift of 8.78 nm was attributed to the collapse state of the temperature-responsive polymer in the mixed SAM. The nanosandwich arrays having the collapsed state of the polymer was incubated with SA (2  $\mu\text{M}$ ) in PBS for 30 min. The LSPR  $\lambda_{\text{max}}$  was recorded at 800 nm, yielding a red-shift of 19 nm (black peak in Figure 3.16E). The overall shift after all kind of modifications was 34.72 nm which was attributed to the change in the refractive index of the surrounding medium of the nanosandwich array because of specific binding of polymers and biomolecules. Here it should be noted that the LSPR  $\lambda_{\text{max}}$  in Figure 3.16D is different when compared with Figure 3.16E owing to the varied thickness of nanosandwich arrays. Also the LSPR responses depend on not only the local refractive index but also the orientation of the linked molecules, which may explain the differences in the results.



**Figure 3.16** (A) Schematic illustration of mixed SAM functionalized nanosandwiches and streptavidin detection above the LCST. Tapping mode AFM images of (B) Unfunctionalized and (C) 0.1 mM 9:1 thiol and terminated polymer/EZ-Link HPDP-Biotin. LSPR measurements of (D) (a) Unfunctionalized nanosandwiches, (b) Nanosandwiches after modification with 0.1 mM 9:1 thiol terminated polymer / EZ-Link HPDP-Biotin, (c) Functionalized nanosandwich arrays after modification with SA (2 μM) (E) Unfunctionalized nanosandwiches, (b) Nanosandwiches after modification with 0.1 mM 9:1 thiol terminated polymer / EZ-Link HPDP-Biotin, (c) Nanosandwich arrays were obtained by coating 9:1 mixed SAM after heating above the LCST, and (d) Functionalized nanosandwich arrays after modification with SA (2 μM).

The binding of SA onto the mix SAM (thiol-terminated polymer and EZ-Link HPDP-Biotin) functionalized surface was also quantified by SPR (Figure 3.17). The reference signal was obtained by DI water injection. Mixture solution (polymer: EZ-Link, 9:1) was injected to chip surface several times till the saturation point. After each injection the chip surface was rinsed with DI water. SA solution (2  $\mu\text{M}$ ) was then injected to the modified chip surface at 25  $^{\circ}\text{C}$ . The binding event between streptavidin and biotin did not occur due to the expanded coil state of the temperature-responsive polymer at 25  $^{\circ}\text{C}$ . The chip surface was rinsed with DI water (25 $^{\circ}\text{C}$ ). To increase the surface temperature, heated DI water was injected to the chip (above LCST). The SA solution was then injected to the surface till the saturation point. After each injection the modified surface was rinsed with heated DI water. The  $\Delta\text{RIU}$  was calculated as 0,00046 RIU. The sensogram in Figure 3.17 represents the binding event and proved that the binding occurred only at high temperature (above the LCST). Surface thickness was calculated based on SPR analysis according to the literature.<sup>221</sup> The total thickness value was obtained as 8,17 nm. Surface coverage was also calculated to be as  $3,692 \times 10^{13}$  SA molecules/ $\text{cm}^2$  surface. The working area of the Nanodev SPR device was  $3,14 \text{cm}^2$ . According to this,  $1,16 \times 10^{13}$  SA molecules were adsorbed to the chip surface.

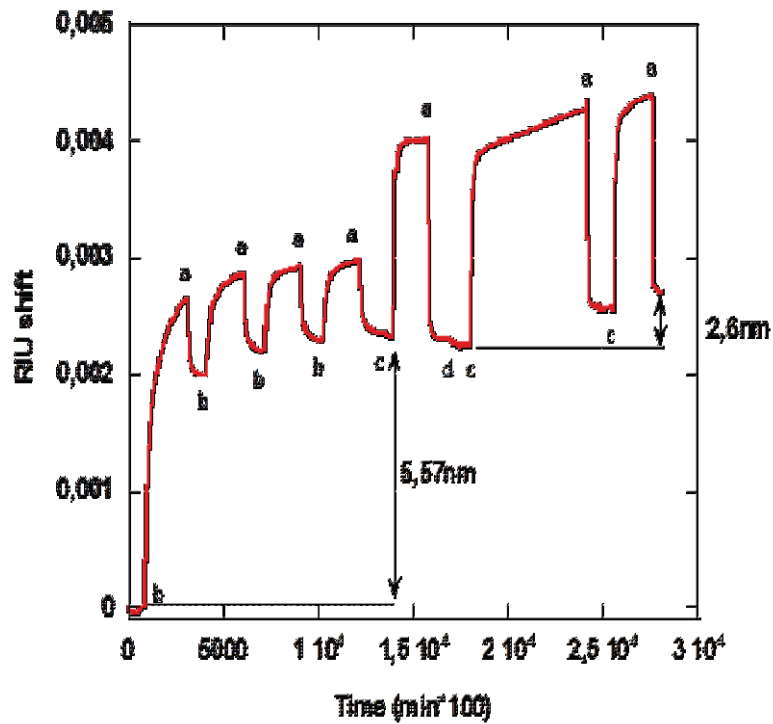


**Figure 3.17** Bioaffinity binding between streptavidin and mixed SAM (polymer+EZ-Link) below and above LCST. (a) DI water injection below LCST, (b) mixed SAM (polymer: EZ-Link, 9:1) injection, (c) SA injection and (d) DI water injection above LCST. Flow rates were, respectively, 100  $\mu\text{L}/\text{min}$ , 20  $\mu\text{L}/\text{min}$ , 20  $\mu\text{L}/\text{min}$  and 100  $\mu\text{L}/\text{min}$ .

### **3.6 Optical Analysis of Gold Nanorods with Different Aspect Ratio**

In this part of the thesis the gold nanorods (GNRs) and their conversion to particles and bubbles were characterized using different techniques such as UV-Vis, Surface Enhanced Raman Scattering (SERS), SEM and AFM. GNRs exhibited specifically two absorption peaks. The first one was transverse absorption peak which was related to the diameter of NRs. The second one, i.e. longitudinal absorption peak, was caused by the length of NRs. Figure 3.18C shows the UV-Vis spectra of GNRs with different aspect ratio. The effect of  $\text{AgNO}_3$  solution can also be seen in Figure 3.18C. The first peak, transverse plasmon band, was approximately observed at 530 nm and the position of peak was the same for all experiments as all of the GNRs were prepared following the same procedure. The second peak, the longitudinal plasmon band indicates the formation of GNRs. The second peak shifted from 680 to 780 nm. The longitudinal plasmon band red-shifted and its intensity increased by increasing the silver concentration.

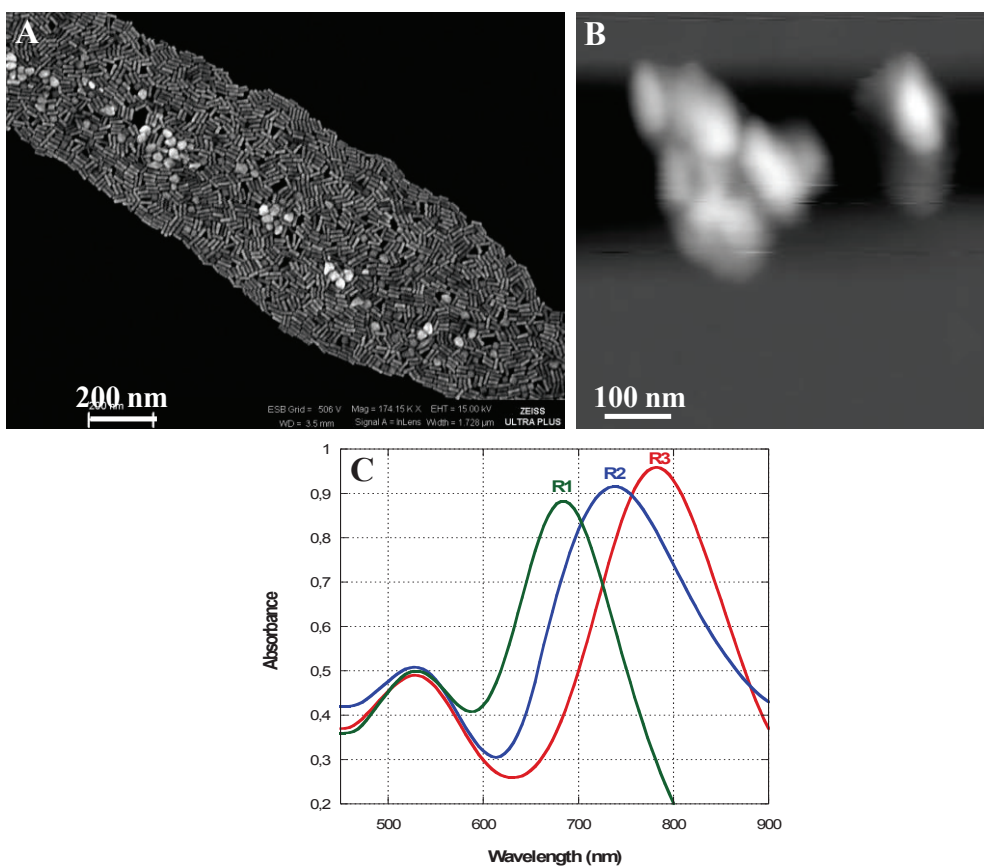


**Figure 3.18** (A) SEM image of GNRs. (B) Tapping mode AFM image of GNRs. (C) UV-Vis spectra of GNRs prepared with different aspect ratio.

Figure 3.18 A and B represent the SEM and AFM images of GNRs on silicon substrate. From the SEM image, the size of GNRs was determined to be 10 nm in diameter and 35 nm in length. The AFM image shows the size of NRs to be 20 nm in diameter and 80 nm in length. These sizes were larger than the ones calculated from SEM images. This was due to broadening effect of AFM tips and CTAB effect on AFM image. As seen in AFM image, the rods were all surrounded by CTAB layers.

### 3.7 Gold Nanorod Preparation with Nitrogen Gas

The effect of various gases was investigated in the synthesis of GNRs to record possible changes in optical property. In this series of experiments the GNRs were converted to GNPs by applying  $N_2$  gas in the seed and also growth solutions. Different nanostructures exhibited varying optical properties owing to their shapes.

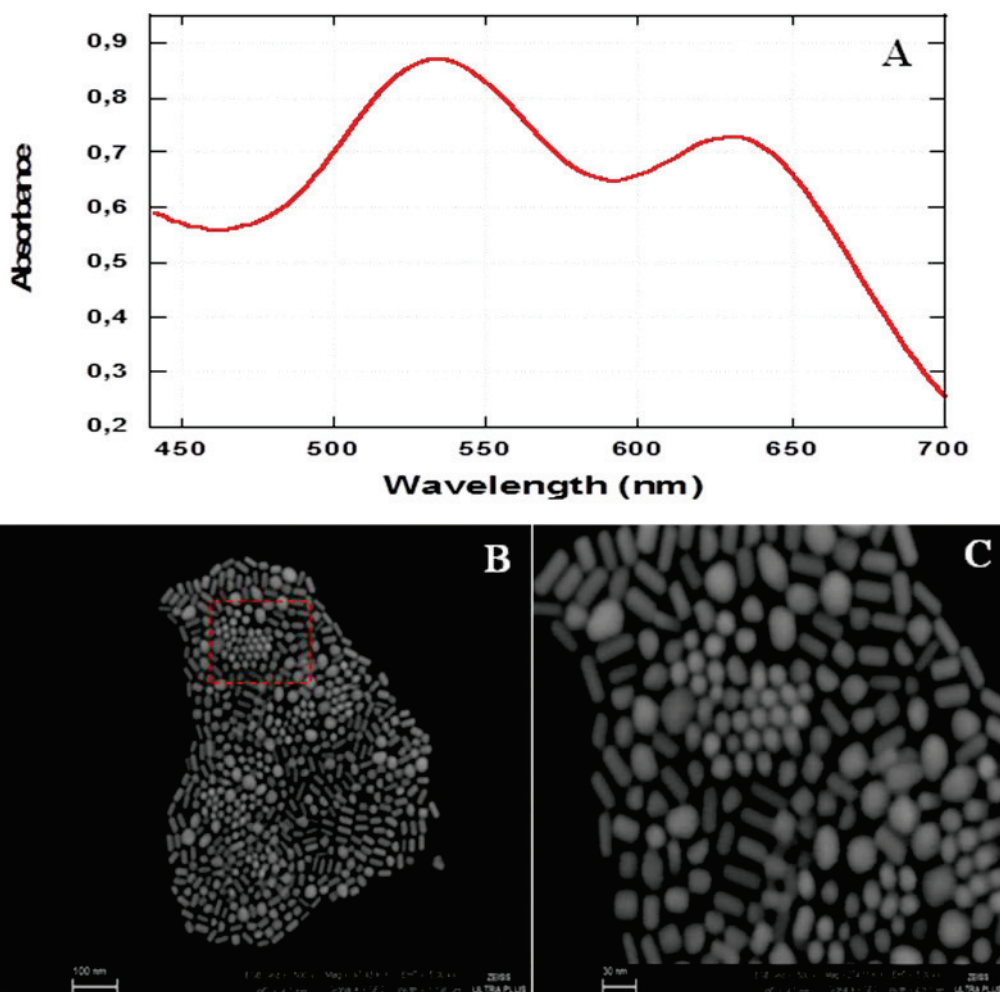


**Figure 3.19** (A) UV-Vis spectrum of GNRs after treatment with  $N_2$  gas. (B) SEM image of GNRs after treatment with  $N_2$  gas. (C) Enlarged image of (B).

In Figure 3.19A, LSPR spectrum show that the absorbance value of longitudinal peak is close to transverse peak. The amount of particles increased in growth solution when  $N_2$  gas was flowed through the reaction. Figure 3.19B and 3.19C are SEM images of GNPs that were produced from GNRs treated with  $N_2$  gas.



Here, in this experiment it should be mentioned that the amount of the N<sub>2</sub> gas flow was very small. This result indicated that the gas molecules may prevent the growth process of the NRs by halting the CTAB. In Figure 3.19B, hexagonally close-packed lattices of GNPs were observed between the GNRs. This formation can be clearly seen in Figure 3.19C. The reason for these may be attributed to the applied gas velocity.

By increasing the velocity and amount of N<sub>2</sub> gas in both seed and growth solutions, the particle formation and the number of particles dramatically increase due to the conversion of NRs to the particles. Figure 3.20A illustrates the LSPR spectra with two blue and red peaks. The red peak indicates the gas flow through both seed and growth solution concentrated twice of the solutions used for NR syntheses. The first peak was measured to be 520 nm which was identical for nanoparticle formation. The second peak was measured to be 820 nm which demonstrated that a small amount of GNRs still existed in solution. The increase in the seed solution concentration together with N<sub>2</sub> gas led to a dramatic increase in the amount of particles which were converted from NRs. The blue LSPR spectrum clearly shows a single peak at 520 nm without having a peak causing from the presence of NRs. SEM images in Figure 3.20C and 3.20D revealed that the formation of only nanoparticles. A very small amount of NRs can still be seen in the solution but they are at a negligible amount to have any optical response as can be seen in blue spectrum in Figure 3.20A.

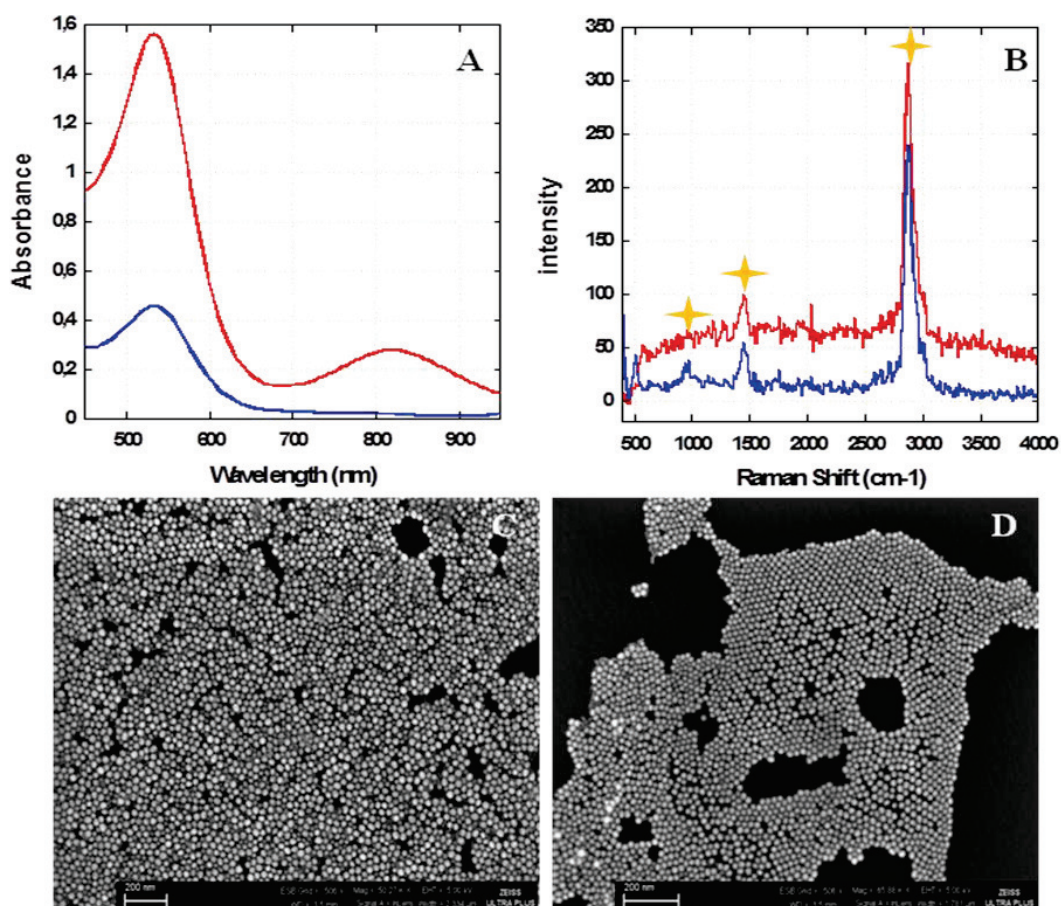


**Figure 3.20** (A) UV-Vis spectra of GNRs treated by N<sub>2</sub> gas. (B) SERS spectra of the same samples A red and blue. (C) SEM image of the nanoparticles and nanorods corresponding to red curve. (D) SEM image of nanoparticles corresponding to blue curve.

Figure 3.20B displays a SERS spectra from gold nanorods treated with N<sub>2</sub> gas. The spectra were taken with an excitation wavelength of 532 nm, which is well matched to the LSPR of NRs. The band at 1070 cm<sup>-1</sup> corresponds to the C-C bonds in the alkyl chain of surfactant. The 1445 cm<sup>-1</sup> band is due to CH<sub>2</sub> scissor modes that are present only along the alkyl chain for CTAB. The band at 2875 cm<sup>-1</sup> owing to CH<sub>2</sub> and CH<sub>3</sub> vibration modes were strongly observed compared to the other peaks.<sup>222</sup>

### 3.8 Gold Nanorod Preparation with Argon Gas

The effect of gas type on the conversion of GNRs to nanoparticles was also investigated to see whether the conversion was due to nitrogen or not. In this experiment, the argon (Ar) gas was used instead of N<sub>2</sub>. The result of this experiment was the same with the result obtained from the experiment performed with N<sub>2</sub>. Figure 3.21A shows the absorption spectra of this experiment. From the spectra one can clearly observe the strong peaks which were due to low and high Ar gas pressure. Single absorption band was observed in the blue spectrum whereas the red spectrum (belonging to the experiment performed under high pressure) had two absorption bands. The  $\lambda_{\text{max}}$  of the absorption peak in the blue spectrum was found to be 530 nm. Single absorption band was an indication of GNPs. Figure 3.21B and 3.21C display SEM images of GNPs, confirming the LSPR results.

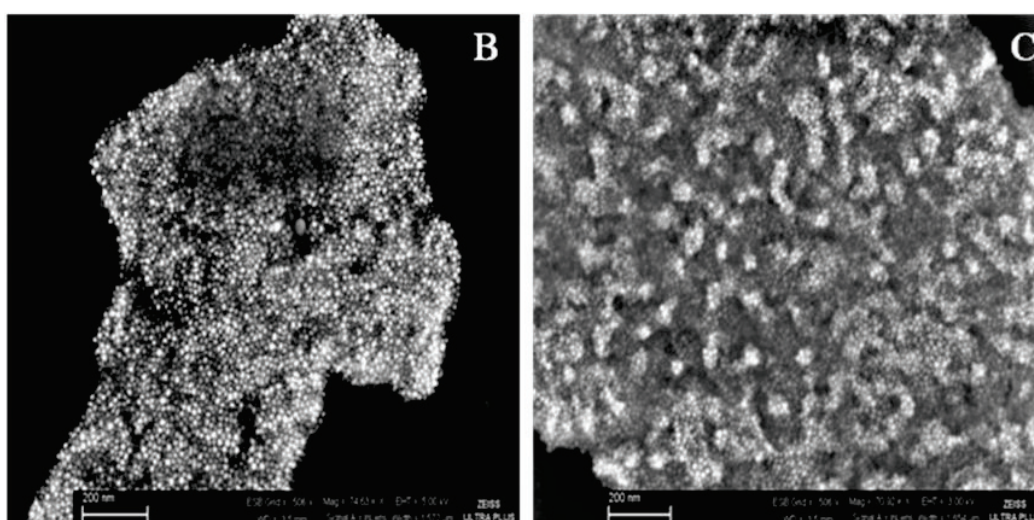
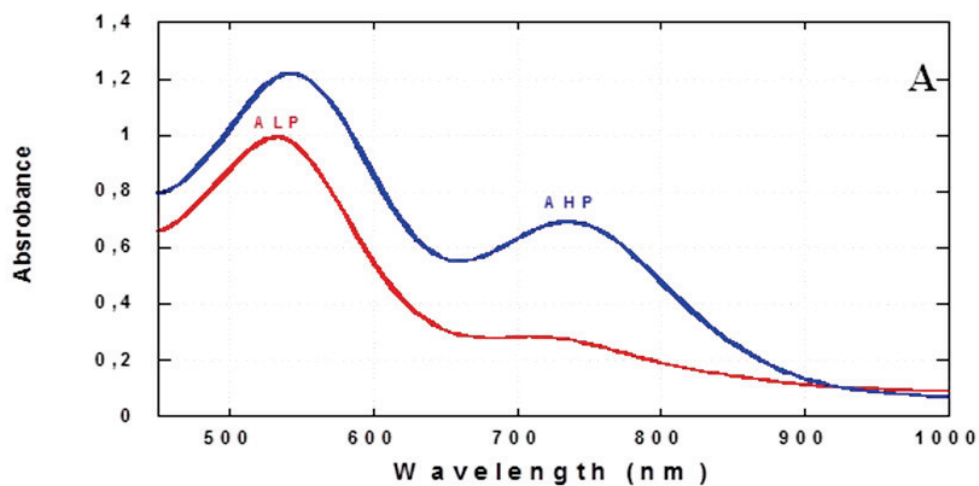


**Figure 3.21** (A) UV-Vis spectra of GNPs according to single step synthesis prepared under low and high pressure Ar. (B) SEM image of particles under low pressure. (C) Enlarged image of (B).

### 3.9 Conversion of Gold Nanorods to Semi-shell and Bubbles

In this part of the experiments performed under gas flow, nanoshells and nanobubbles were produced using nitrogen gas. In these experiments, nitrogen gas flow rate was higher than the rate used for conversion of rods to particles.

Figure 3.22A gives UV-Vis absorption spectrum of semi-shells formed from NRs. The absorption peak was measured to be 520 nm. A small shoulder in the spectrum was observed at approximately 800 nm which may be due to NRs.

Figure 3.22B displays SERS spectrum of semi-shells. The spectrum was taken with an excitation wavelength of 532 nm, which was well matched to the LSPR of semi-shell. The band at  $1070\text{ cm}^{-1}$  corresponded to the C-C bonds in the alkyl chain of surfactant. The  $1445\text{ cm}^{-1}$  band was due to  $\text{CH}_2$  scissor modes that were present only along the alkyl chain for CTAB. In the SERS spectrum, extra band can be seen at  $589\text{ cm}^{-1}$ . This band arises from Si substrate. The band at  $2875\text{ cm}^{-1}$  owing to  $\text{CH}_2$  and  $\text{CH}_3$  vibration modes were strongly observed compared to the other peaks.

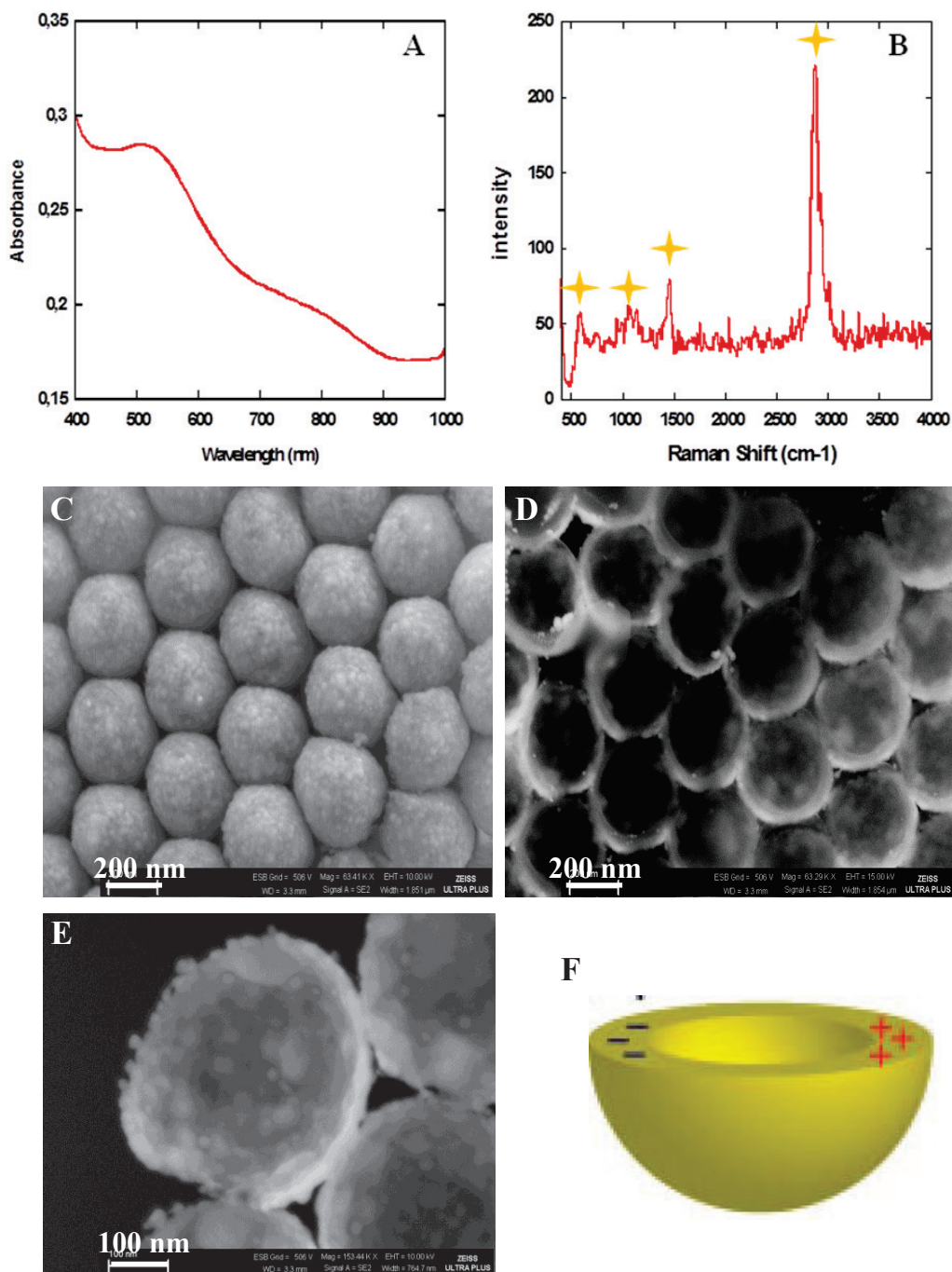


**Figure 3.22** (A) UV-Vis spectrum of semi-shells, seed solution was prepared under N<sub>2</sub>. (B) SERS spectrum of semi-shell. (C) SEM image of face off semi-shells, (D and E) low and high magnification of face up nanoshell. (F) Model of the semi-shell.

A series of SEM images with low and high magnification illustrate the conversion of NRs to nanoshells. Two packings of semi-shells can be observed from the images. One shows that the semi-shells are seated face-up onto silicon substrate. Figure 3.22C shows the high resolution image of the face-up semishells. Figure 3.22D and 3.22E are low and high magnification of face up semi-shells. The highest resolution clearly shows the semi-shells wall occupied with NRs and NPs (Figure 3.22E).

The nitrogen gas introduced to all processes in the NRs synthesis to understand why the bubbles or semi-shells are developed after gas treatment. For this a series of control experiments were run and the results are given in this section.

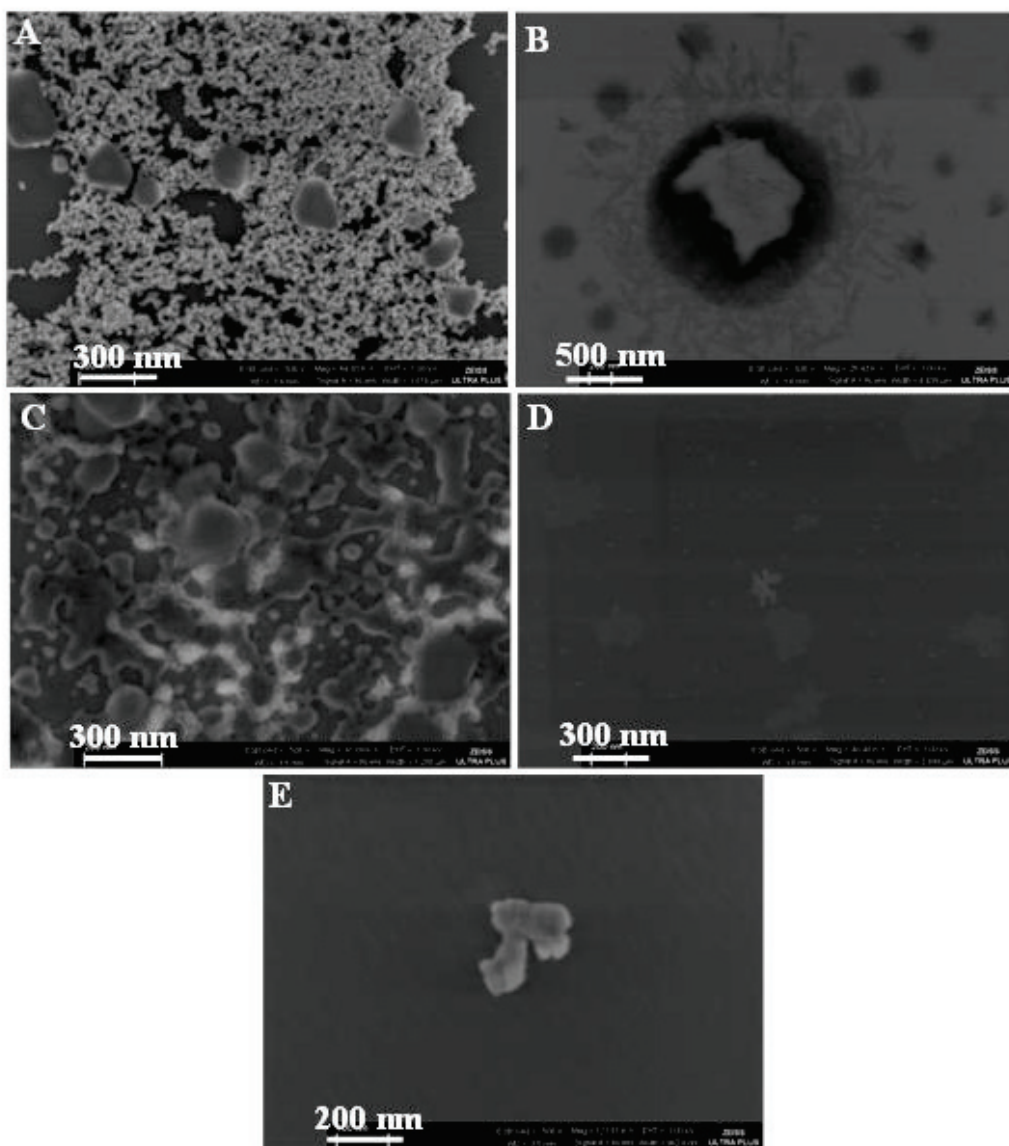


**Figure 3.23** Control experiments for gas treatment.

The control experiments show in Figure 3.23 revealed the effect of gas treatment at each stage of GNR synthesis. First,  $N_2$  gas was applied only to auric acid solution (Figure 3.23A). From the image there is no evidence of any bubble or semi-shell formations. Second, sodium borohydride were taken under  $N_2$  gas, as seen in the Figure 3.23B and again no bubble shape or other formation found in the image. In Figure 3.23C and 3.23D CTAB and CTAB/ auric acid mixture were reacted with  $N_2$  gas, respectively. In both images no bubbles either semi-shells observed. In the last control experiment sodium borohydride and CTAB mixture were taken under  $N_2$



gas and no evidence of any bubble or semishell formation was observed. As a conclusion for this part, the bubble and semi-shell can be produced only during nanorods synthesis.

It can be speculated that during NRs synthesis CTAB molecules act like bridges between hydrophobic gas bubble and negatively charged gold seeds leading to formation of gold nanoshells at low gas flow and nanobubbles at high gas flow rate.

Figure 3.24 demonstrates LSPR spectrum and SEM images of nanobubbles. In LSPR spectrum, two peaks appear at 530 nm and 750 nm. The peak at 530 nm is due to well known GNP in UV-Vis region. A peak at 750 nm indicates that the GNRs still exist in the solution, but these NRs are encapsulated inside the bubbles as shown in SEM images. The SEM image in Figure 3.24B demonstrated the bubbles with diameters ranging between 200-500 nm. The surface of particles seems to be like the CTAB micelles grown with nitrogen gas. When these particles are under electron microscope for at least 1 minute the bubbles get transparent probably due to the burning of CTAB molecules (Figure 3.24C and 3.24D).

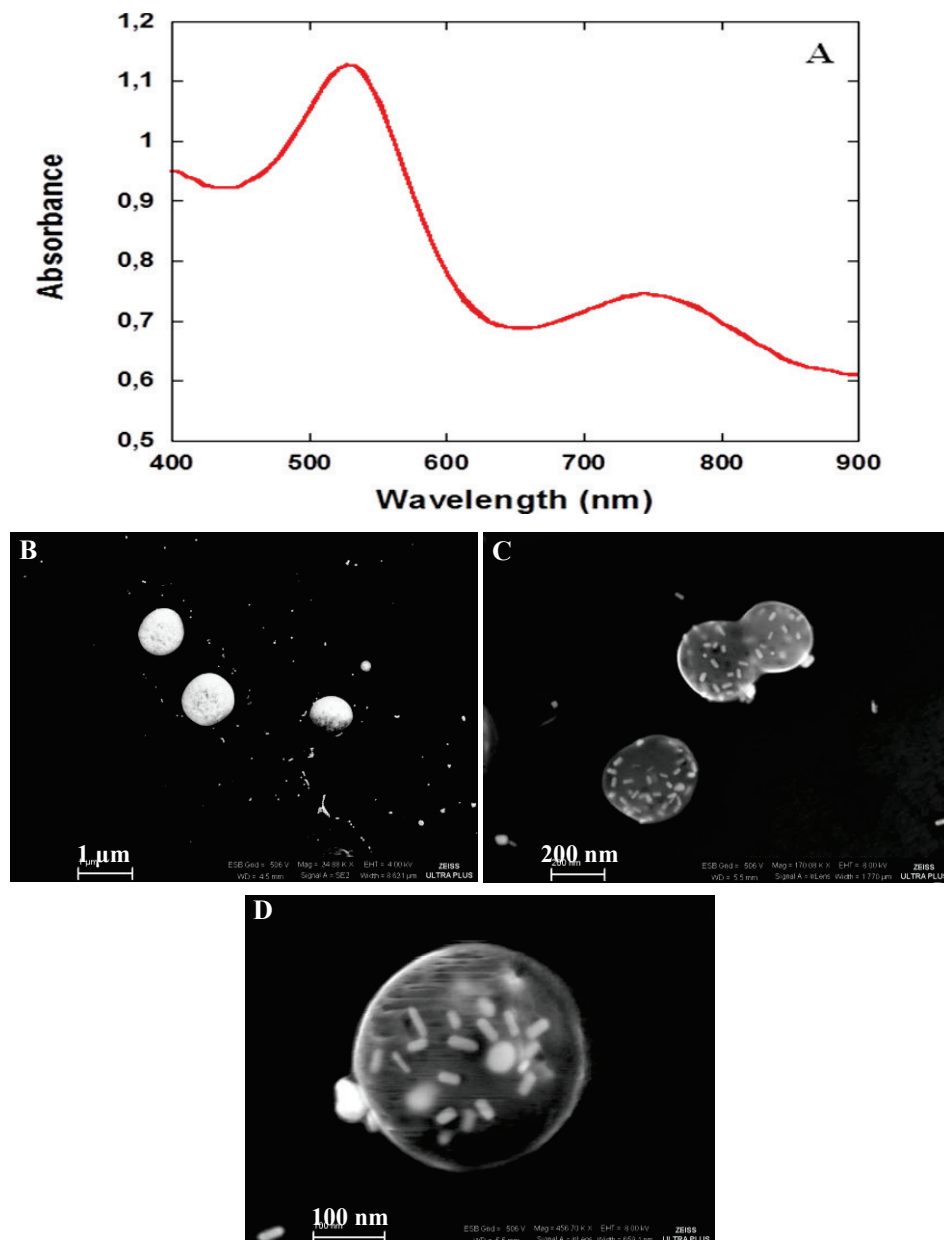


**Figure 3.24** (A) UV-Vis spectrum of gold nanobubbles, seed solution was prepared under  $N_2$  gas. (B-D) SEM images of nanobubbles.

### 3.10 Conjugation of Gold Nanorods with Nanodots Arrays

GNRs exhibit wellknown affinity to thiol compounds. The only (111) face of the GNRs are easily utilized by alkanethiols for formation of SAMs or other biological molecules. The formation of alkanethiol SAM leads to a red-shift of the plasmon in which the peak is due to the changes in refractive index at the surface of the GNRs.<sup>223</sup> Figure 3.25A illustrates the LSPR spectra of nanorods suspension before and after interaction with mix SAM (which is composed of 9:1 decanethiol (DT): EZ-Link HPDP-Biotin). The longitudinal peak shifts from 696 nm to 707 nm while the transverse peak remains at ~520 nm. After functionalization, plasmon peak shows a significant move through the red region of 8-11 nm that may be due to the mix SAM formation.

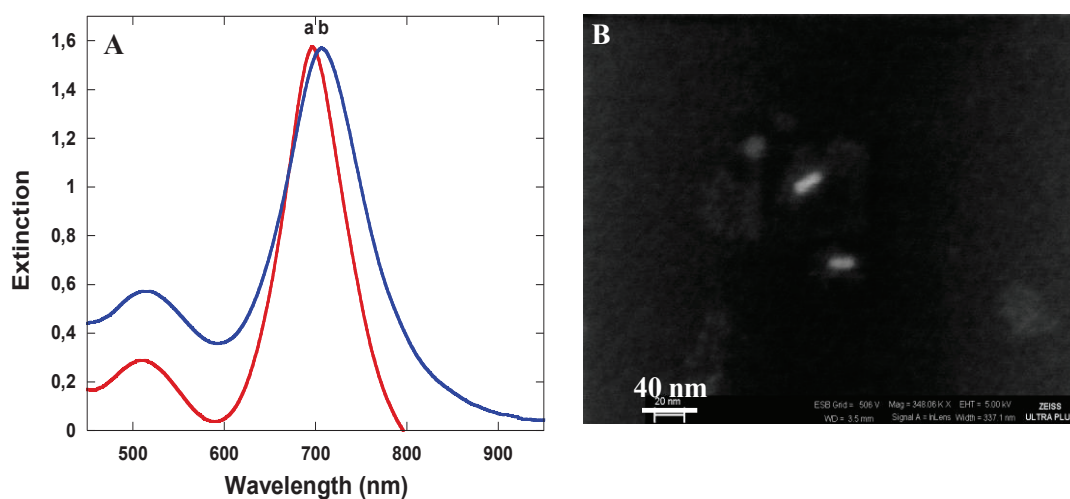


**Figure 3.25** (A) LSPR spectra of (a) unfunctionalized and (b) functionalized GNRs. (B) SEM image of functionalized GNRs.

The SEM image of the GNRs coated with mix SAM is illustrated in Figure 3.25B. From the image it is clear that the mix SAM bound to the NRs, which is in good agreement with the LSPR measurement.

This final section of the thesis show how a nanoscale mechano-optical device can be produced by the process of chemical self-assembly. The device that envisaged

will consist of multitude of nanoscale rods of gold that can be raised or lowered in response to an external stimulus. The actuator for this movement will be a conformation-changing responsive polymer. The movement of the rod will cause the optical properties of a surface change. The basic experiments were performed here in this thesis and will be continue for future work. Here, we demonstrated that the GNRs can be attached to triangle nanodot arrays with organic molecules. The same process will be repeated with temperature responsive polymer instead of organic molecules in future work and is not covered in this thesis.

Figure 3.26A represents the schematic structures of GNRs after functionalization with SAM, followed by the binding to nanodots arrays which were modified with mixed SAM and SA molecules. The LSPR spectra presented in Figure 3.26B display that the shifts observed with the unfunctionalized and functionalized Au nanodot arrays. LSPR  $\lambda_{\max}$  of the unfunctionalized Au nanodot array was measured to be 698.6 nm (a). After incubation of the nanodots with mixture of 9:1 DT and EZ-Link HPDP-Biotin (0.1 mM) for 24 h, the LSPR analysis showed a  $\lambda_{\max}$  of 712.5 nm (b). A red-shift of 13,9 nm was attributed to the binding of the mixed SAM to nanodot array. After the nanodot arrays coated with the mix SAM, the sample was incubated with SA (2  $\mu$ M) for 30 min and the LSPR  $\lambda_{\max}$  was measured to be 731.94 nm, yielding a red shift of 19,44 nm (c). On the other hand, GNRs were incubated in the mixed SAM solution for 24 h. After 24 h, the functionalized nanodots substrate was incubated with the thiolated GNRs using streptavidin as linker and the LSPR  $\lambda_{\max}$  was recorded at 745,83 nm (d). The overall shift after modifications was 47,23 nm which corresponded to the change in the refractive index of the surrounding medium of the nanodot arrays due to the linked biomolecules. The SEM and AFM images in Figure 3.26C and 3.26D, respectively show the binding of GNRs to nanodots arrays through linker molecules.

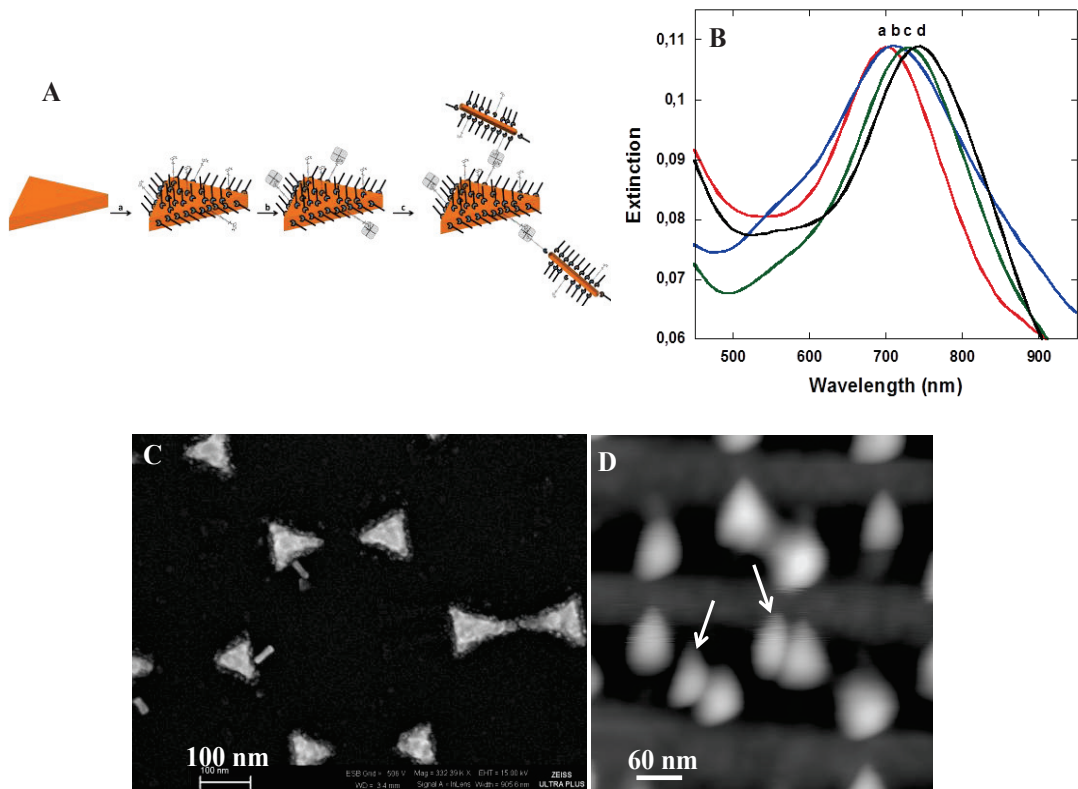


**Figure 3.26** (A) Schematic illustration of the binding event of (a) mixed SAM (DT+Ez-Link biotin), (b) streptavidin (SA) and (c) mixed SAM functionalized GNRs on nanodot arrays. (B) LSPR spectra of the modified nanodot arrays with functionalized GNRs. (C) SEM and (D) AFM images of the modified nanodot arrays with functionalized GNRs.

## 4 CONCLUSION

This thesis reveals that nanoparticles in the form of triangle nanosandwiches prepared using natural lithography or in the form of nanorods/nanobubbles prepared by wet chemistry have important optical properties and that the enhanced sensitivity of their surrounding environment can be used as a new class of optical sensors using Localized Surface Plasmon Resonance (LSPR) spectroscopy and Surface Enhanced Raman Scattering (SERS).

The major findings of the work are summarized below:

The nanostructures with single or multilayers before and after treatment with polymeric materials and biological macromolecules were initially analyzed using different techniques. The principle of nanostructure preparation by nanosphere lithography was illustrated and explained. The nanoparticle arrays were used as a mask for deposition of the noble metals and inorganic compounds such as Au, Ag, Al<sub>2</sub>O<sub>3</sub> and HfO<sub>2</sub>.

The temperature-responsive polymers were used to control over biomolecular recognitions by slight temperature changes. This would allow the detection of different biomolecular recognition events on nanostructure arrays to be differentiated by changing the temperature of the environment.

The functionalisation of 20 nm Au / 20 nm Al<sub>2</sub>O<sub>3</sub> / 20 nm Au or 20 nm Au / 20 nm HfO<sub>2</sub> / 20 nm Au nanosandwiches with thiol and phosphate terminated polymers, or thiol terminated polymer and allyltriethoxy silane (ATES), respectively, were analyzed by LSPR and Atomic Force Microscopy (AFM). From the LSPR measurements it was observed that both Au, Al<sub>2</sub>O<sub>3</sub> and HfO<sub>2</sub> layers of nanosandwiches were successfully modified with thiolated and phosphonated

polymers and ATEs, respectively, as indicated by significant red-shifts of the  $\lambda_{\text{max}}$  values. The presence of polymers and ATEs at the surrounding of nanosandwiches was also verified by AFM images of nanosandwiches. It was also shown by SPR experiments that phosphonated polymer and ATEs do not bind to Au layer, proving that there is no cross-binding of these compounds to Au layer of nanosandwiches.

The 20 nm Au / 20 nm Al<sub>2</sub>O<sub>3</sub> / 20 nm Au nanosandwiches were then functionalized with the mixed SAM of thiol terminated polymer and EZ-Link HPDP-Biotin (9:1). The binding of streptavidin to the mixed SAM below and above the Lower Critical Solution Temperature (LCST) of the polymer was analyzed by LSPR and AFM. The data showed the efficient binding of the protein to the nanosandwiches above the LCST while there was no binding below the LCST. As expected, the temperature-responsive polymer actuator inhibits the binding of protein due to steric hindrance effect when the temperature was below LCST. AFM images supported the data obtained by LSPR.

The gold nanorods, nanoparticles and nanobubbles were prepared using various gases flow, and characterized by different techniques such as UV-Vis, SERS, SEM and AFM. By increasing the velocity and amount of nitrogen gas in both seed and growth solutions of nanorods, the conversion of nanorods to nanoparticles increases. Different nanostructures exhibited varying optical properties owing to their shapes. Finally, the gold nanorods conjugated with nanodots arrays for development of a nanoscale mechano-optical device.

## 5 FUTURE WORK

In this thesis, three polymers with thiol, phosphate and silane end group were bound to the nanosandwiches and investigated in detailed by various techniques. This work which was a part of TUBITAK (PROJECT NO:110T759) funded project, can be continued by binding to the nanosandwiches different end functionalized polymers and biomolecules for real-life biosensor applications required in medical, environmental or agricultural areas.

The nanorods with various aspect ratios were prepared in this thesis together with conversion of these rods to bubbles and semi-shell. The work can be continued for applications of these encapsulated nanorods in the bubbles/semishells for cancer treatment and targeting. The work related to mechano-optical device that was performed in the last section of this thesis can be continued by attaching gold nanorods to triangle nanodots arrays using temperature responsive polymers as linkers for temperature controlled for mechano-optical devices.



## REFERENCES

1. Bok, S.; Korampally, V.; Darr, C. M.; Folk, W. R.; Polo-Parada, L.; Gangopadhyay, K.; Gangopadhyay, S., Femtogram-level detection of Clostridium botulinum neurotoxin type A by sandwich immunoassay using nanoporous substrate and ultra-bright fluorescent suprananoparticles. *Biosensors and Bioelectronics* **2013**, *41* (0), 409-416.
2. Chen, Y. U. S. A. U. a. S.-M., *Nanostructured Materials for Electrochemical Biosensors* Nova Science Publishers, Inc. New York 2011.
3. Lowe, C. R., Introduction to Biosensor and Biochip Technologies. In *Handbook of Biosensors and Biochips*, John Wiley & Sons, Ltd: 2008.
4. Lowe, C. R., Biosensors. *Trends in Biotechnology* **1984**, *2* (3), 59-65.
5. Qlark, L. C. J., Monitor and Control of Blood and Tissue Oxygen Tensions. *ASAIO Journal* **1956**, *2* (1), 41-48.
6. Clark, L. C.; Lyons, C., ELECTRODE SYSTEMS FOR CONTINUOUS MONITORING IN CARDIOVASCULAR SURGERY. *Annals of the New York Academy of Sciences* **1962**, *102* (1), 29-45.
7. Updike, S. J.; Hicks, G. P., The Enzyme Electrode. *Nature* **1967**, *214* (5092), 986-988.
8. Guilbault, G. G.; Montalvo, J. G., Urea-specific enzyme electrode. *Journal of the American Chemical Society* **1969**, *91* (8), 2164-2165.
9. Cooney, C. L.; Weaver, J. C.; Tannebaum, S. R.; Faller, D. V.; Shields, A.; Jahnke, M., The Thermal Enzyme Probe — A Novel Approach to Chemical Analysis. In *Enzyme Engineering Volume 2*, Pye, E. K.; Wingard, L., Jr., Eds. Springer US: 1974; pp 411-417.
10. Mosbach, K.; Danielsson, B., An enzyme thermistor. *Biochimica et Biophysica Acta (BBA) - Enzymology* **1974**, *364* (1), 140-145.
11. Lubbers, D. W.; Opitz, N., GE))PCO<sub>2</sub>-OPTODE-PO<sub>2</sub>-OPTODE - NEW PROBE FOR MEASUREMENT OF PCO<sub>2</sub> OR PO<sub>2</sub> IN FLUIDS AND GASES. *Zeitschrift Fur Naturforschung C-a Journal of Biosciences* **1975**, *30* (7-8), 532-533.
12. Shichiri, M.; Kawamori, R.; Yamasaki, Y.; Hakui, N.; Abe, H., WEARABLE ARTIFICIAL ENDOCRINE PANCREAS WITH NEEDLE-TYPE GLUCOSE SENSOR. *Lancet* **1982**, *2* (8308), 1129-1131.
13. Liedberg, B.; Nylander, C.; Lundstrom, I., SURFACE-PLASMON RESONANCE FOR GAS-DETECTION AND BIOSENSING. *Sensors and Actuators* **1983**, *4* (2), 299-304.
14. (a) Lee, Y. H.; Mutharasan, R., Chapter 6 - Biosensors. In *Sensor Technology Handbook*, Jon, S. W., Ed. Newnes: Burlington, 2005; pp 161-180; (b) Davis, J.; Huw Vaughan, D.; Cardosi, M. F., Elements of biosensor construction. *Enzyme and Microbial Technology* **1995**, *17* (12), 1030-1035.
15. Mandke, R.; Layek, B.; Sharma, G.; Singh, J., Fabrication and Evaluation of Nanoparticle-Based Biosensors. In *Biosensor Nanomaterials*, Wiley-VCH Verlag GmbH & Co. KGaA: 2011; pp 73-93.
16. Wang, J., Glucose Biosensors: 40 Years of Advances and Challenges. *Electroanalysis* **2001**, *13* (12), 983-988.
17. Spink, C.; Wadsö, I., Calorimetry as an Analytical Tool in Biochemistry and Biology. In *Methods of Biochemical Analysis*, John Wiley & Sons, Inc.: 2006; pp 1-159.
18. (a) Fan, X.; White, I. M.; Shopova, S. I.; Zhu, H.; Suter, J. D.; Sun, Y., Sensitive optical biosensors for unlabeled targets: A review. *Analytica Chimica Acta*

- 2008**, 620 (1–2), 8-26; (b) Passaro, V.; Dell'Olio, F.; Casamassima, B.; De Leonardis, F., Guided-Wave Optical Biosensors. *Sensors* **2007**, 7 (4), 508-536.
19. Proll, G., R. Narayanaswamy, O.S. Wolfbeis (eds.): Optical Sensors: Industrial, Environmental and Diagnostic Applications. *Anal Bioanal Chem* **2005**, 381 (1), 18-19.
20. Skoog, D. A.; Holler, F. J.; Crouch, S. R., *Principles of Instrumental Analysis* Brooks Cole: Boston, 2006.
21. Wang, J.; Zhang, P.; Li, C. M.; Li, Y. F.; Huang, C. Z., A highly selective and colorimetric assay of lysine by molecular-driven gold nanorods assembly. *Biosens. Bioelectron.* **2012**, 34 (1), 197-201.
22. Li, Y.; Liu, X.; Lin, Z., Recent developments and applications of surface plasmon resonance biosensors for the detection of mycotoxins in foodstuffs. *Food Chem.* **2012**, 132 (3), 1549-1554.
23. (a) Kalogianni, D. P.; Koraki, T.; Christopoulos, T. K.; Ioannou, P. C., Nanoparticle-based DNA biosensor for visual detection of genetically modified organisms. *Biosensors and Bioelectronics* **2006**, 21 (7), 1069-1076; (b) Terry, L. A.; White, S. F.; Tigwell, L. J., The Application of Biosensors to Fresh Produce and the Wider Food Industry. *Journal of Agricultural and Food Chemistry* **2005**, 53 (5), 1309-1316.
24. Barrado, E.; Rodriguez, J. A.; Castrillejo, Y., Renewable stationary phase liquid magnetochromatography: determining aspartame and its hydrolysis products in diet soft drinks. *Anal Bioanal Chem* **2006**, 385 (7), 1233-1240.
25. Kress-Rogers, E.; D'Costa, E. J.; Sollars, J. E.; Gibbs, P. A.; Turner, A. P. F., Measurement of meat freshness in situ with a biosensor array. *Food Control* **1993**, 4 (3), 149-154.
26. Marrazza, G.; Chianella, I.; Mascini, M., Disposable DNA electrochemical biosensors for environmental monitoring. *Analytica Chimica Acta* **1999**, 387 (3), 297-307.
27. Eltzov, E.; Pavluchkov, V.; Burstin, M.; Marks, R. S., Creation of a fiber optic based biosensor for air toxicity monitoring. *Sens. Actuator B-Chem.* **2011**, 155 (2), 859-867.
28. Kumar, J.; D'Souza, S. F., An optical microbial biosensor for detection of methyl parathion using *Sphingomonas* sp immobilized on microplate as a reusable biocomponent. *Biosens. Bioelectron.* **2010**, 26 (4), 1292-1296.
29. Elad, T.; Almog, R.; Yagur-Kroll, S.; Levkov, K.; Melamed, S.; Shacham-Diamand, Y.; Belkin, S., Online Monitoring of Water Toxicity by Use of Bioluminescent Reporter Bacterial Biochips. *Environ. Sci. Technol.* **2011**, 45 (19), 8536-8544.
30. Frense, D.; Müller, A.; Beckmann, D., Detection of environmental pollutants using optical biosensor with immobilized algae cells. *Sensors and Actuators B: Chemical* **1998**, 51 (1–3), 256-260.
31. McGrath, T. F.; Campbell, K.; Fodey, T. L.; O'Kennedy, R.; Elliott, C. T., An evaluation of the capability of a biolayer interferometry biosensor to detect low-molecular-weight food contaminants. *Anal Bioanal Chem* **2013**, 405 (8), 2535-2544.
32. Skládal, P.; Fiala, M.; Krejčí, J., Detection of Pesticides in the Environment Using Biosensors Based on Cholinesterases. *International Journal of Environmental Analytical Chemistry* **1996**, 65 (1-4), 139-148.
33. Rasmussen, M.; Minter, S. D., Self-powered herbicide biosensor utilizing thylakoid membranes. *Anal. Methods* **2013**, 5 (5), 1140-1144.

34. Bok, S.; Korampally, V.; Darr, C. M.; Folk, W. R.; Polo-Parada, L.; Gangopadhyay, K.; Gangopadhyay, S., Femtogram-level detection of Clostridium botulinum neurotoxin type A by sandwich immunoassay using nanoporous substrate and ultra-bright fluorescent suprananoparticles. *Biosens. Bioelectron.* **2013**, *41*, 409-416.
35. Sommer, A. P.; Gheorghiu, E.; Cehreli, M.; Mester, A. R.; Whelan, H. T., Biosensor for Detection of Nanobacteria in Water. *Crystal Growth & Design* **2006**, *6* (2), 492-497.
36. (a) Xu, M. Y.; Luo, X. L.; Davis, J. J., The label free picomolar detection of insulin in blood serum. *Biosens. Bioelectron.* **2013**, *39* (1), 21-25; (b) Wang, L. X.; Zheng, Q.; Zhang, Q. A.; Xu, H. F.; Tong, J. L.; Zhu, C. D.; Wan, Y., Detection of single tumor cell resistance with aptamer biochip. *Oncol. Lett.* **2012**, *4* (5), 935-940; (c) Jeong, H. J.; Ohmuro-Matsuyama, Y.; Ohashi, H.; Ohsawa, F.; Tatsu, Y.; Inagaki, M.; Ueda, H., Detection of vimentin serine phosphorylation by multicolor Quenchbodies. *Biosens. Bioelectron.* **2013**, *40* (1), 17-23.
37. (a) Kartha, K. K.; Babu, S. S.; Srinivasan, S.; Ajayaghosh, A., Attogram Sensing of Trinitrotoluene with a Self-Assembled Molecular Gelator. *J. Am. Chem. Soc.* **2012**, *134* (10), 4834-4841; (b) Svabenska, E., Systems for Detection and Identification of Biological Aerosols. *Def. Sci. J.* **2012**, *62* (6), 404-411.
38. Bohrn, U.; Stutz, E.; Fuchs, K.; Fleischer, M.; Schoning, M. J.; Wagner, P., Monitoring of irritant gas using a whole-cell-based sensor system. *Sens. Actuator B-Chem.* **2012**, *175*, 208-217.
39. Notingher, I.; Green, C.; Dyer, C.; Perkins, E.; Hopkins, N.; Lindsay, C.; Hench, L. L., Discrimination between ricin and sulphur mustard toxicity in vitro using Raman spectroscopy. *J. R. Soc. Interface* **2004**, *1* (1), 79-90.
40. Arduini, F.; Neagu, D.; Dall'Oglio, S.; Moscone, D.; Palleschi, G., Towards a Portable Prototype Based on Electrochemical Cholinesterase Biosensor to be Assembled to Soldier Overall for Nerve Agent Detection. *Electroanalysis* **2012**, *24* (3), 581-590.
41. Lee, S.-W.; Ahn, J.; Kim, M.-G.; Shin, Y.-B.; Lee, J. J.; Lim, K.-P.; Kim, K.-B., Enhanced Biomolecular Detection Based on Localized Surface Plasmon Resonance (LSPR) Using Enzyme-Precipitation Reaction. *Journal of Nanoscience and Nanotechnology* **2010**, *10* (5), 3246-3249.
42. Chung, T.; Lee, S. Y.; Song, E. Y.; Chun, H.; Lee, B., Plasmonic nanostructures for nano-scale bio-sensing. *Sensors* **2011**, *11* (11), 10907-29.
43. Hall, W. P.; Ngatia, S. N.; Van Duyne, R. P., LSPR Biosensor Signal Enhancement Using Nanoparticle-Antibody Conjugates. *The journal of physical chemistry. C, Nanomaterials and interfaces* **2011**, *115* (5), 1410-1414.
44. Kohls, O.; Scheper, T., Setup of a fiber optical oxygen multisensor-system and its applications in biotechnology. *Sensors and Actuators B: Chemical* **2000**, *70* (1-3), 121-130.
45. (a) Yonzon, C. R.; Haynes, C. L.; Zhang, X.; Walsh, J. T.; Van Duyne, R. P., A Glucose Biosensor Based on Surface-Enhanced Raman Scattering: Improved Partition Layer, Temporal Stability, Reversibility, and Resistance to Serum Protein Interference. *Analytical Chemistry* **2003**, *76* (1), 78-85; (b) Haes, A. J.; Hall, W. P.; Chang, L.; Klein, W. L.; Van Duyne, R. P., A Localized Surface Plasmon Resonance Biosensor: First Steps toward an Assay for Alzheimer's Disease. *Nano Letters* **2004**, *4* (6), 1029-1034.

46. Ho, H.-A.; Leclerc, M., Optical Sensors Based on Hybrid Aptamer/Conjugated Polymer Complexes. *Journal of the American Chemical Society* **2004**, *126* (5), 1384-1387.
47. Bauer, G.; Hassmann, J.; Walter, H.; Haglmüller, J.; Mayer, C.; Schalkhammer, T., Resonant nanocluster technology—from optical coding and high quality security features to biochips. *Nanotechnology* **2003**, *14* (12), 1289.
48. Yonzon, C. R.; Stuart, D. A.; Zhang, X.; McFarland, A. D.; Haynes, C. L.; Van Duyne, R. P., Towards advanced chemical and biological nanosensors—An overview. *Talanta* **2005**, *67* (3), 438-448.
49. Chin, C. W.-S. Localized Surface Plasmon Resonance with the use of Silver and Titanium Oxide Nanostructures The University of Tennessee, Knoxville 2011.
50. Edgar, J. A. Development of New Methods for the Synthesis of Plasmonically-Active Precious Metal Rods and Shells University of Technology, Sydney 2011
51. Lemmens, K. Preparation and Optimization of New Interfaces for Localized Surface Plasmon Resonance (LSPR) and Surface-Enhanced Raman Scattering (SERS) Studies Industriële Wetenschappen, Biochemie, 2008.
52. Hong, Y.; Huh, Y.-M.; Yoon, D. S.; Yang, J., Nanobiosensors based on localized surface plasmon resonance for biomarker detection. *J. Nanomaterials* **2012**, *2012*, 111-111.
53. (a) Freeman, R. G.; Grabar, K. C.; Allison, K. J.; Bright, R. M.; Davis, J. A.; Guthrie, A. P.; Hommer, M. B.; Jackson, M. A.; Smith, P. C.; Walter, D. G.; Natan, M. J., Self-Assembled Metal Colloid Monolayers: An Approach to SERS Substrates. *Science* **1995**, *267* (5204), 1629-1632; (b) Kahl, M.; Voges, E.; Kostrewa, S.; Viets, C.; Hill, W., Periodically structured metallic substrates for SERS. *Sensors and Actuators B: Chemical* **1998**, *51* (1-3), 285-291; (c) Schatz, G. C.; Van Duyne, R. P., Electromagnetic Mechanism of Surface-Enhanced Spectroscopy. In *Handbook of Vibrational Spectroscopy*, John Wiley & Sons, Ltd: 2006; (d) Haynes, C. L.; Van Duyne, R. P., Plasmon-Sampled Surface-Enhanced Raman Excitation Spectroscopy†. *The Journal of Physical Chemistry B* **2003**, *107* (30), 7426-7433; (e) Haynes, C. L.; McFarland, A. D.; Zhao, L.; Van Duyne, R. P.; Schatz, G. C.; Gunnarsson, L.; Prikulis, J.; Kasemo, B.; Käll, M., Nanoparticle Optics: The Importance of Radiative Dipole Coupling in Two-Dimensional Nanoparticle Arrays†. *The Journal of Physical Chemistry B* **2003**, *107* (30), 7337-7342.
54. (a) Dirix, Y.; Bastiaansen, C.; Caseri, W.; Smith, P., Oriented Pearl-Necklace Arrays of Metallic Nanoparticles in Polymers: A New Route Toward Polarization-Dependent Color Filters. *Advanced Materials* **1999**, *11* (3), 223-227; (b) Haynes, C. L.; Van Duyne, R. P., Dichroic Optical Properties of Extended Nanostructures Fabricated Using Angle-Resolved Nanosphere Lithography. *Nano Letters* **2003**, *3* (7), 939-943.
55. (a) Maier, S. A.; Brongersma, M. L.; Kik, P. G.; Meltzer, S.; Requicha, A. A. G.; Atwater, H. A., Plasmonics—A Route to Nanoscale Optical Devices. *Advanced Materials* **2001**, *13* (19), 1501-1505; (b) Maier, S. A.; Kik, P. G.; Atwater, H. A.; Meltzer, S.; Harel, E.; Koel, B. E.; Requicha, A. A. G., Local detection of electromagnetic energy transport below the diffraction limit in metal nanoparticle plasmon waveguides. *Nat Mater* **2003**, *2* (4), 229-232; (c) Shelby, R. A.; Smith, D. R.; Schultz, S., Experimental Verification of a Negative Index of Refraction. *Science* **2001**, *292* (5514), 77-79; (d) Andersen, P. C.; Rowlen, K. L., Brilliant Optical

Properties of Nanometric Noble Metal Spheres, Rods, and Aperture Arrays. *Appl. Spectrosc.* **2002**, *56* (5), 124A-135A.

56. (a) Haes, A. J.; Zou, S.; Schatz, G. C.; Van Duyne, R. P., A Nanoscale Optical Biosensor: The Long Range Distance Dependence of the Localized Surface Plasmon Resonance of Noble Metal Nanoparticles. *The Journal of Physical Chemistry B* **2003**, *108* (1), 109-116; (b) Obare, S. O.; Hollowell, R. E.; Murphy, C. J., Sensing Strategy for Lithium Ion Based on Gold Nanoparticles. *Langmuir* **2002**, *18* (26), 10407-10410; (c) Bailey, R. C.; Nam, J.-M.; Mirkin, C. A.; Hupp, J. T., Real-Time Multicolor DNA Detection with Chemoresponsive Diffraction Gratings and Nanoparticle Probes. *Journal of the American Chemical Society* **2003**, *125* (44), 13541-13547; (d) Hirsch, L. R.; Jackson, J. B.; Lee, A.; Halas, N. J.; West, J. L., A Whole Blood Immunoassay Using Gold Nanoshells. *Analytical Chemistry* **2003**, *75* (10), 2377-2381; (e) Haes, A. J. Localized Surface Plasmon Resonance Spectroscopy for Fundamental Studies of Nanoparticle Optics and Applications to Biosensors Northwestern University 2004.

57. (a) El-Sayed, M. A., Some Interesting Properties of Metals Confined in Time and Nanometer Space of Different Shapes. *Accounts of Chemical Research* **2001**, *34* (4), 257-264; (b) Mulvaney, P., Surface Plasmon Spectroscopy of Nanosized Metal Particles. *Langmuir* **1996**, *12* (3), 788-800; (c) Hulteen, J. C.; Treichel, D. A.; Smith, M. T.; Duval, M. L.; Jensen, T. R.; Van Duyne, R. P., Nanosphere Lithography: Size-Tunable Silver Nanoparticle and Surface Cluster Arrays. *The Journal of Physical Chemistry B* **1999**, *103* (19), 3854-3863.

58. Jensen, T. R.; Malinsky, M. D.; Haynes, C. L.; Van Duyne, R. P., Nanosphere Lithography: Tunable Localized Surface Plasmon Resonance Spectra of Silver Nanoparticles. *The Journal of Physical Chemistry B* **2000**, *104* (45), 10549-10556.

59. (a) Michaels, A. M.; Nirmal, M.; Brus, L. E., Surface Enhanced Raman Spectroscopy of Individual Rhodamine 6G Molecules on Large Ag Nanocrystals. *Journal of the American Chemical Society* **1999**, *121* (43), 9932-9939; (b) Schultz, S.; Smith, D. R.; Mock, J. J.; Schultz, D. A., Single-target molecule detection with nonbleaching multicolor optical immunolabels. *Proceedings of the National Academy of Sciences* **2000**, *97* (3), 996-1001.

60. Yguerabide, J.; Yguerabide, E. E., Light-Scattering Submicroscopic Particles as Highly Fluorescent Analogs and Their Use as Tracer Labels in Clinical and Biological Applications: I. Theory. *Analytical Biochemistry* **1998**, *262* (2), 137-156.

61. Kreibig, U. V., M., *Cluster Materials*. Springer-Verlag: Heidelberg: 1995; Vol. 25.

62. (a) Sönnichsen, C.; Franzl, T.; Wilk, T.; von Plessen, G.; Feldmann, J.; Wilson, O.; Mulvaney, P., Drastic Reduction of Plasmon Damping in Gold Nanorods. *Physical Review Letters* **2002**, *88* (7), 077402; (b) Bao, P.; Frutos, A. G.; Greef, C.; Lahiri, J.; Muller, U.; Peterson, T. C.; Warden, L.; Xie, X., High-Sensitivity Detection of DNA Hybridization on Microarrays Using Resonance Light Scattering. *Analytical Chemistry* **2002**, *74* (8), 1792-1797; (c) McFarland, A. D.; Van Duyne, R. P., Single Silver Nanoparticles as Real-Time Optical Sensors with Zeptomole Sensitivity. *Nano Letters* **2003**, *3* (8), 1057-1062.

63. (a) Connolly, S.; Cobbe, S.; Fitzmaurice, D., Effects of Ligand-Receptor Geometry and Stoichiometry on Protein-Induced Aggregation of Biotin-Modified Colloidal Gold. *The Journal of Physical Chemistry B* **2001**, *105* (11), 2222-2226; (b) Storhoff, J. J.; Lazarides, A. A.; Mucic, R. C.; Mirkin, C. A.; Letsinger, R. L.; Schatz, G. C., What Controls the Optical Properties of DNA-Linked Gold

Nanoparticle Assemblies? *Journal of the American Chemical Society* **2000**, *122* (19), 4640-4650; (c) Connolly, S.; Rao, S. N.; Fitzmaurice, D., Characterization of Protein Aggregated Gold Nanocrystals. *The Journal of Physical Chemistry B* **2000**, *104* (19), 4765-4776.

64. (a) Malinsky, M. D.; Kelly, K. L.; Schatz, G. C.; Van Duyne, R. P., Chain Length Dependence and Sensing Capabilities of the Localized Surface Plasmon Resonance of Silver Nanoparticles Chemically Modified with Alkanethiol Self-Assembled Monolayers. *Journal of the American Chemical Society* **2001**, *123* (7), 1471-1482; (b) Hilger, A.; Cüppers, N.; Tenfelde, M.; Kreibig, U., Surface and interface effects in the optical properties of silver nanoparticles. *Eur. Phys. J. D* **2000**, *10* (1), 115-118; (c) Henglein, A.; Meisel, D., Spectrophotometric Observations of the Adsorption of Organosulfur Compounds on Colloidal Silver Nanoparticles. *The Journal of Physical Chemistry B* **1998**, *102* (43), 8364-8366.

65. (a) Nath, N.; Chilkoti, A., A Colorimetric Gold Nanoparticle Sensor To Interrogate Biomolecular Interactions in Real Time on a Surface. *Analytical Chemistry* **2001**, *74* (3), 504-509; (b) Eck, D.; Helm, C. A.; Wagner, N. J.; Vaynberg, K. A., Plasmon Resonance Measurements of the Adsorption and Adsorption Kinetics of a Biopolymer onto Gold Nanocolloids. *Langmuir* **2001**, *17* (4), 957-960; (c) Okamoto, T.; Yamaguchi, I.; Kobayashi, T., Local plasmon sensor with gold colloid monolayers deposited upon glass substrates. *Opt. Lett.* **2000**, *25* (6), 372-374; (d) Himmelhaus, M.; Takei, H., Cap-shaped gold nanoparticles for an optical biosensor. *Sensors and Actuators B: Chemical* **2000**, *63* (1-2), 24-30.

66. Szunerits, S.; Das, M. R.; Boukherroub, R., Short- and Long-Range Sensing on Gold Nanostructures, Deposited on Glass, Coated with Silicon Oxide Films of Different Thicknesses. *The Journal of Physical Chemistry C* **2008**, *112* (22), 8239-8243.

67. Englebienne, P., Use of colloidal gold surface plasmon resonance peak shift to infer affinity constants from the interactions between protein antigens and antibodies specific for single or multiple epitopes. *Analyst* **1998**, *123* (7), 1599-1603.

68. (a) Haes, A. J.; Zou, S.; Schatz, G. C.; Van Duyne, R. P., Nanoscale Optical Biosensor: Short Range Distance Dependence of the Localized Surface Plasmon Resonance of Noble Metal Nanoparticles. *The Journal of Physical Chemistry B* **2004**, *108* (22), 6961-6968; (b) Whitney, A. V.; Elam, J. W.; Zou, S.; Zinovev, A. V.; Stair, P. C.; Schatz, G. C.; Van Duyne, R. P., Localized Surface Plasmon Resonance Nanosensor: A High-Resolution Distance-Dependence Study Using Atomic Layer Deposition. *The Journal of Physical Chemistry B* **2005**, *109* (43), 20522-20528.

69. (a) Haes, A. J.; Zou, S.; Zhao, J.; Schatz, G. C.; Van Duyne, R. P., Localized Surface Plasmon Resonance Spectroscopy near Molecular Resonances. *Journal of the American Chemical Society* **2006**, *128* (33), 10905-10914; (b) Zhao, J.; Jensen, L.; Sung, J.; Zou, S.; Schatz, G. C.; Van Duyne, R. P., Interaction of Plasmon and Molecular Resonances for Rhodamine 6G Adsorbed on Silver Nanoparticles. *Journal of the American Chemical Society* **2007**, *129* (24), 7647-7656.

70. (a) Haes, A. J.; Van Duyne, R. P., A Nanoscale Optical Biosensor: Sensitivity and Selectivity of an Approach Based on the Localized Surface Plasmon Resonance Spectroscopy of Triangular Silver Nanoparticles. *Journal of the American Chemical Society* **2002**, *124* (35), 10596-10604; (b) Bingham, J.; Hall, W. P.; Duyne, R., Exploring the Unique Characteristics of LSPR Biosensing. In *Nanoplasmonic Sensors*, Dmitriev, A., Ed. Springer New York: 2012; pp 29-58.

71. (a) Lukosz, W., Principles and sensitivities of integrated optical and surface plasmon sensors for direct affinity sensing and immunosensing. *Biosensors and Bioelectronics* **1991**, *6* (3), 215-225; (b) Liedberg, B.; Nylander, C.; Lundström, I., Biosensing with surface plasmon resonance — how it all started. *Biosensors and Bioelectronics* **1995**, *10* (8), i-ix; (c) Garland, P. B., Optical evanescent wave methods for the study of biomolecular interactions. *Quarterly Reviews of Biophysics* **1996**, *29* (01), 91-117; (d) Jung, L. S.; Shumaker-Parry, J. S.; Campbell, C. T.; Yee, S. S.; Gelb, M. H., Quantification of Tight Binding to Surface-Immobilized Phospholipid Vesicles Using Surface Plasmon Resonance: Binding Constant of Phospholipase A2. *Journal of the American Chemical Society* **2000**, *122* (17), 4177-4184.
72. (a) Jung, L. S.; Campbell, C. T., Sticking Probabilities in Adsorption of Alkanethiols from Liquid Ethanol Solution onto Gold. *The Journal of Physical Chemistry B* **2000**, *104* (47), 11168-11178; (b) Schuck, P., USE OF SURFACE PLASMON RESONANCE TO PROBE THE EQUILIBRIUM AND DYNAMIC ASPECTS OF INTERACTIONS BETWEEN BIOLOGICAL MACROMOLECULES<sup>1</sup>. *Annual Review of Biophysics and Biomolecular Structure* **1997**, *26* (1), 541-566.
73. Brockman, J. M.; Nelson, B. P.; Corn, R. M., SURFACE PLASMON RESONANCE IMAGING MEASUREMENTS OF ULTRATHIN ORGANIC FILMS. *Annual Review of Physical Chemistry* **2000**, *51* (1), 41-63.
74. Jung, L. S.; Campbell, C. T.; Chinowsky, T. M.; Mar, M. N.; Yee, S. S., Quantitative Interpretation of the Response of Surface Plasmon Resonance Sensors to Adsorbed Films. *Langmuir* **1998**, *14* (19), 5636-5648.
75. Mock, J. J.; Smith, D. R.; Schultz, S., Local Refractive Index Dependence of Plasmon Resonance Spectra from Individual Nanoparticles. *Nano Letters* **2003**, *3* (4), 485-491.
76. (a) Frederix, F.; Friedt, J.-M.; Choi, K.-H.; Laureyn, W.; Campitelli, A.; Mondelaers, D.; Maes, G.; Borghe, G., Biosensing Based on Light Absorption of Nanoscaled Gold and Silver Particles. *Analytical Chemistry* **2003**, *75* (24), 6894-6900; (b) Lahav, M.; Vaskevich, A.; Rubinstein, I., Biological Sensing Using Transmission Surface Plasmon Resonance Spectroscopy. *Langmuir* **2004**, *20* (18), 7365-7367.
77. Riboh, J. C.; Haes, A. J.; McFarland, A. D.; Ranjit Yonzon, C.; Van Duyne, R. P., A Nanoscale Optical Biosensor: Real-Time Immunoassay in Physiological Buffer Enabled by Improved Nanoparticle Adhesion. *The Journal of Physical Chemistry B* **2003**, *107* (8), 1772-1780.
78. Yonzon, C. R.; Jeoung, E.; Zou, S.; Schatz, G. C.; Mrksich, M.; Van Duyne, R. P., A Comparative Analysis of Localized and Propagating Surface Plasmon Resonance Sensors: The Binding of Concanavalin A to a Monosaccharide Functionalized Self-Assembled Monolayer. *Journal of the American Chemical Society* **2004**, *126* (39), 12669-12676.
79. Haes, A. J.; Chang, L.; Klein, W. L.; Van Duyne, R. P., Detection of a Biomarker for Alzheimer's Disease from Synthetic and Clinical Samples Using a Nanoscale Optical Biosensor. *Journal of the American Chemical Society* **2005**, *127* (7), 2264-2271.
80. Dahlin, A.; Zäch, M.; Rindzevicius, T.; Käll, M.; Sutherland, D. S.; Höök, F., Localized Surface Plasmon Resonance Sensing of Lipid-Membrane-Mediated

Biorecognition Events. *Journal of the American Chemical Society* **2005**, *127* (14), 5043-5048.

81. Lin, T.-J.; Huang, K.-T.; Liu, C.-Y., Determination of organophosphorous pesticides by a novel biosensor based on localized surface plasmon resonance. *Biosensors and Bioelectronics* **2006**, *22* (4), 513-518.

82. Endo, T.; Yanagida, Y.; Hatsuzawa, T., Quantitative determination of hydrogen peroxide using polymer coated Ag nanoparticles. *Measurement* **2008**, *41* (9), 1045-1053.

83. Dubas, S. T.; Pimpan, V., Green synthesis of silver nanoparticles for ammonia sensing. *Talanta* **2008**, *76* (1), 29-33.

84. (a) Bingham, J. M.; Anker, J. N.; Kreno, L. E.; Van Duyne, R. P., Gas Sensing with High-Resolution Localized Surface Plasmon Resonance Spectroscopy. *Journal of the American Chemical Society* **2010**, *132* (49), 17358-17359; (b) Kreno, L. E.; Hupp, J. T.; Van Duyne, R. P., Metal–Organic Framework Thin Film for Enhanced Localized Surface Plasmon Resonance Gas Sensing. *Analytical Chemistry* **2010**, *82* (19), 8042-8046; (c) Cheng, C.-S.; Chen, Y.-Q.; Lu, C.-J., Organic vapour sensing using localized surface plasmon resonance spectrum of metallic nanoparticles self assemble monolayer. *Talanta* **2007**, *73* (2), 358-365; (d) Chen, Y.-Q.; Lu, C.-J., Surface modification on silver nanoparticles for enhancing vapor selectivity of localized surface plasmon resonance sensors. *Sensors and Actuators B: Chemical* **2009**, *135* (2), 492-498.

85. Duval Malinsky, M.; Kelly, K. L.; Schatz, G. C.; Van Duyne, R. P., Nanosphere Lithography: Effect of Substrate on the Localized Surface Plasmon Resonance Spectrum of Silver Nanoparticles. *The Journal of Physical Chemistry B* **2001**, *105* (12), 2343-2350.

86. Pinchuk, A.; Hilger, A.; Plessen, G. v.; Kreibig, U., Substrate effect on the optical response of silver nanoparticles. *Nanotechnology* **2004**, *15* (12), 1890.

87. Hanarp, P.; Käll, M.; Sutherland, D. S., Optical Properties of Short Range Ordered Arrays of Nanometer Gold Disks Prepared by Colloidal Lithography. *The Journal of Physical Chemistry B* **2003**, *107* (24), 5768-5772.

88. Haynes, C. L.; Van Duyne, R. P., Nanosphere Lithography: A Versatile Nanofabrication Tool for Studies of Size-Dependent Nanoparticle Optics. *The Journal of Physical Chemistry B* **2001**, *105* (24), 5599-5611.

89. Sherry, L. J.; Chang, S.-H.; Schatz, G. C.; Van Duyne, R. P.; Wiley, B. J.; Xia, Y., Localized Surface Plasmon Resonance Spectroscopy of Single Silver Nanocubes. *Nano Letters* **2005**, *5* (10), 2034-2038.

90. Hicks, E. M.; Zhang, X.; Zou, S.; Lyandres, O.; Spears, K. G.; Schatz, G. C.; Van Duyne, R. P., Plasmonic Properties of Film over Nanowell Surfaces Fabricated by Nanosphere Lithography. *The Journal of Physical Chemistry B* **2005**, *109* (47), 22351-22358.

91. Xiang, G.; Zhang, N.; Zhou, X., Localized Surface Plasmon Resonance Biosensing with Large Area of Gold Nanoholes Fabricated by Nanosphere Lithography. *Nanoscale Res Lett* **2010**, *5* (5), 818-822.

92. Dmitriev, A.; Pakizeh, T.; Käll, M.; Sutherland, D. S., Gold–Silica–Gold Nanosandwiches: Tunable Bimodal Plasmonic Resonators. *Small* **2007**, *3* (2), 294-299.

93. Endo, T.; Ikeda, R.; Yanagida, Y.; Hatsuzawa, T., Stimuli-responsive hydrogel–silver nanoparticles composite for development of localized surface



plasmon resonance-based optical biosensor. *Analytica Chimica Acta* **2008**, *611* (2), 205-211.

94. Ma, W.; Yang, H.; Wang, W.; Gao, P.; Yao, J., Ethanol Vapor Sensing Properties of Triangular Silver Nanostructures Based on Localized Surface Plasmon Resonance. *Sensors* **2011**, *11* (9), 8643-8653.

95. Gehan, H. I. n.; Mangeney, C.; Aubard, J.; Lévi, G.; Hohenau, A.; Krenn, J. R.; Lacaze, E.; Félidj, N., Design and Optical Properties of Active Polymer-Coated Plasmonic Nanostructures. *The Journal of Physical Chemistry Letters* **2011**, *2* (8), 926-931.

96. (a) Willets, K. A.; Van Duyne, R. P., Localized Surface Plasmon Resonance Spectroscopy and Sensing. *Annual Review of Physical Chemistry* **2007**, *58* (1), 267-297; (b) Aroca, R., *Surface-enhanced vibrational spectroscopy*. Wiley:Chichester: 2006.

97. Castro, J. L.; Lopez-Ramirez, M. R.; Arenas, J. F.; Soto, J.; Otero, J. C., Evidence of Deprotonation of Aromatic Acids and Amides Adsorbed on Silver Colloids by Surface-Enhanced Raman Scattering. *Langmuir* **2012**, *28* (24), 8926-8932.

98. Linn, N. C. Scaleable and Reproducible Fabrication of SERS (Surface-Enhanced Raman Scattering) Substrates with High Enhancement Factors University of Florida, 2010.

99. Smith, E.; Dent, G., *Modern Raman Spectroscopy: A Practical Approach*. John Wiley and Sons: 2005.

100. Champion, A.; Kambhampati, P., Surface-enhanced Raman scattering. *Chemical Society Reviews* **1998**, *27* (4), 241-250.

101. Creighton, J. A.; Eadon, D. G., Ultraviolet-visible absorption spectra of the colloidal metallic elements. *Journal of the Chemical Society, Faraday Transactions* **1991**, *87* (24), 3881-3891.

102. Lombardi, J. R.; Birke, R. L.; Lu, T.; Xu, J., Charge-transfer theory of surface enhanced Raman spectroscopy: Herzberg--Teller contributions. *The Journal of Chemical Physics* **1986**, *84* (8), 4174-4180.

103. (a) Brolo, A. G.; Jiang, Z.; Irish, D. E., The orientation of 2,2'-bipyridine adsorbed at a SERS-active Au(111) electrode surface. *Journal of Electroanalytical Chemistry* **2003**, *547* (2), 163-172; (b) Michota, A.; Bukowska, J., Surface-enhanced Raman scattering (SERS) of 4-mercaptopbenzoic acid on silver and gold substrates. *Journal of Raman Spectroscopy* **2003**, *34* (1), 21-25.

104. Le Ru, E. C.; Blackie, E.; Meyer, M.; Etchegoin, P. G., Surface Enhanced Raman Scattering Enhancement Factors: A Comprehensive Study. *The Journal of Physical Chemistry C* **2007**, *111* (37), 13794-13803.

105. Skoog, D. A. H., F. J.; Nieman, T. A., *Principles of Instrumental Analysis*. Harcourt Brace & Company: Orlando: 1998.

106. Fleischmann, M.; Hendra, P. J.; McQuillan, A. J., Raman spectra of pyridine adsorbed at a silver electrode. *Chemical Physics Letters* **1974**, *26* (2), 163-166.

107. Jeanmaire, D. L.; Van Duyne, R. P., Surface raman spectroelectrochemistry: Part I. Heterocyclic, aromatic, and aliphatic amines adsorbed on the anodized silver electrode. *Journal of Electroanalytical Chemistry and Interfacial Electrochemistry* **1977**, *84* (1), 1-20.

108. Albrecht, M. G.; Creighton, J. A., Anomalously intense Raman spectra of pyridine at a silver electrode. *Journal of the American Chemical Society* **1977**, *99* (15), 5215-5217.

109. (a) Moskovits, M., Surface-enhanced spectroscopy. *Reviews of Modern Physics* **1985**, 57 (3), 783-826; (b) Haynes, C. L.; Yonzon, C. R.; Zhang, X.; Van Duyne, R. P., Surface-enhanced Raman sensors: early history and the development of sensors for quantitative biowarfare agent and glucose detection. *Journal of Raman Spectroscopy* **2005**, 36 (6-7), 471-484.
110. (a) Koglin, E.; Séquaris, J.-M., Surface enhanced raman scattering of biomolecules. In *Analytical Problems*, Springer Berlin Heidelberg: 1986; Vol. 134, pp 1-57; (b) Cotton, T. M.; Kim, J.-H.; Chumanov, G. D., Application of surface-enhanced Raman spectroscopy to biological systems. *Journal of Raman Spectroscopy* **1991**, 22 (12), 729-742; (c) Sokolov, K.; Khodorchenko, P.; Petukhov, A.; Nabiev, I.; Chumanov, G.; Cotton, T. M., Contributions of Short-Range and Classical Electromagnetic Mechanisms to Surface-Enhanced Raman Scattering from Several Types of Biomolecules Adsorbed on Cold-Deposited Island Films. *Appl. Spectrosc.* **1993**, 47 (4), 515-522.
111. Shafer-Peltier, K. E.; Haynes, C. L.; Glucksberg, M. R.; Van Duyne, R. P., Toward a Glucose Biosensor Based on Surface-Enhanced Raman Scattering. *Journal of the American Chemical Society* **2002**, 125 (2), 588-593.
112. Dick, L. A.; McFarland, A. D.; Haynes, C. L.; Van Duyne, R. P., Metal Film over Nanosphere (MFON) Electrodes for Surface-Enhanced Raman Spectroscopy (SERS): Improvements in Surface Nanostructure Stability and Suppression of Irreversible Loss. *The Journal of Physical Chemistry B* **2001**, 106 (4), 853-860.
113. Nikoobakht, B.; Wang, J.; El-Sayed, M. A., Surface-enhanced Raman scattering of molecules adsorbed on gold nanorods: off-surface plasmon resonance condition. *Chemical Physics Letters* **2002**, 366 (1-2), 17-23.
114. Xu, H.; Bjerneld, E. J.; Käll, M.; Börjesson, L., Spectroscopy of Single Hemoglobin Molecules by Surface Enhanced Raman Scattering. *Physical Review Letters* **1999**, 83 (21), 4357-4360.
115. Kneipp, K.; Wang, Y.; Kneipp, H.; Perelman, L. T.; Itzkan, I.; Dasari, R. R.; Feld, M. S., Single Molecule Detection Using Surface-Enhanced Raman Scattering (SERS). *Physical Review Letters* **1997**, 78 (9), 1667-1670.
116. (a) Nikoobakht, B.; El-Sayed, M. A., Surface-Enhanced Raman Scattering Studies on Aggregated Gold Nanorods†. *The Journal of Physical Chemistry A* **2003**, 107 (18), 3372-3378; (b) Faulds, K.; Littleford, R. E.; Graham, D.; Dent, G.; Smith, W. E., Comparison of Surface-Enhanced Resonance Raman Scattering from Unaggregated and Aggregated Nanoparticles. *Analytical Chemistry* **2003**, 76 (3), 592-598; (c) Kneipp, K.; Kneipp, H.; Manoharan, R.; Hanlon, E. B.; Itzkan, I.; Dasari, R. R.; Feld, M. S., Extremely Large Enhancement Factors in Surface-Enhanced Raman Scattering for Molecules on Colloidal Gold Clusters. *Appl. Spectrosc.* **1998**, 52 (12), 1493-1497.
117. Schwartzberg, A. M.; Grant, C. D.; Wolcott, A.; Talley, C. E.; Huser, T. R.; Bogomolni, R.; Zhang, J. Z., Unique Gold Nanoparticle Aggregates as a Highly Active Surface-Enhanced Raman Scattering Substrate. *The Journal of Physical Chemistry B* **2004**, 108 (50), 19191-19197.
118. Kho, K. W.; Shen, Z. X.; Zeng, H. C.; Soo, K. C.; Olivo, M., Deposition Method for Preparing SERS-Active Gold Nanoparticle Substrates. *Analytical Chemistry* **2005**, 77 (22), 7462-7471.
119. Zhang, X.; Shah, N. C.; Van Duyne, R. P., Sensitive and selective chem/bio sensing based on surface-enhanced Raman spectroscopy (SERS). *Vibrational Spectroscopy* **2006**, 42 (1), 2-8.

120. Baia, M.; Baia, L.; Astilean, S., Gold nanostructured films deposited on polystyrene colloidal crystal templates for surface-enhanced Raman spectroscopy. *Chemical Physics Letters* **2005**, *404* (1–3), 3-8.
121. Baia, L.; Baia, M.; Popp, J.; Astilean, S., Gold Films Deposited over Regular Arrays of Polystyrene Nanospheres as Highly Effective SERS Substrates from Visible to NIR. *The Journal of Physical Chemistry B* **2006**, *110* (47), 23982-23986.
122. Dasary, S. S. R.; Singh, A. K.; Senapati, D.; Yu, H.; Ray, P. C., Gold Nanoparticle Based Label-Free SERS Probe for Ultrasensitive and Selective Detection of Trinitrotoluene. *Journal of the American Chemical Society* **2009**, *131* (38), 13806-13812.
123. Lee, S. J.; Morrill, A. R.; Moskovits, M., Hot Spots in Silver Nanowire Bundles for Surface-Enhanced Raman Spectroscopy. *Journal of the American Chemical Society* **2006**, *128* (7), 2200-2201.
124. Bae, Y.; Kim, N. H.; Kim, M.; Lee, K. Y.; Han, S. W., Anisotropic Assembly of Ag Nanoprisms. *Journal of the American Chemical Society* **2008**, *130* (16), 5432-5433.
125. Oldenburg, S. J.; Westcott, S. L.; Averitt, R. D.; Halas, N. J., Surface enhanced Raman scattering in the near infrared using metal nanoshell substrates. *The Journal of Chemical Physics* **1999**, *111* (10), 4729-4735.
126. Ghosh, S. K.; Pal, T., Interparticle Coupling Effect on the Surface Plasmon Resonance of Gold Nanoparticles: From Theory to Applications. *Chemical Reviews* **2007**, *107* (11), 4797-4862.
127. (a) Kim, T.; Lee, K.; Gong, M.-s.; Joo, S.-W., Control of Gold Nanoparticle Aggregates by Manipulation of Interparticle Interaction. *Langmuir* **2005**, *21* (21), 9524-9528; (b) Zhong, Z.; Patskovskyy, S.; Bouvrette, P.; Luong, J. H. T.; Gedanken, A., The Surface Chemistry of Au Colloids and Their Interactions with Functional Amino Acids. *The Journal of Physical Chemistry B* **2004**, *108* (13), 4046-4052.
128. Yoon, J. H.; Park, J. S.; Yoon, S., Time-Dependent and Symmetry-Selective Charge-Transfer Contribution to SERS in Gold Nanoparticle Aggregates. *Langmuir* **2009**, *25* (21), 12475-12480.
129. Gehan, H.; Fillaud, L.; Chehimi, M. M.; Aubard, J.; Hohenau, A.; Felidj, N.; Mangeney, C., Thermo-induced Electromagnetic Coupling in Gold/Polymer Hybrid Plasmonic Structures Probed by Surface-Enhanced Raman Scattering. *ACS Nano* **2010**, *4* (11), 6491-6500.
130. Malham, I. B.; Bureau, L., Density Effects on Collapse, Compression, and Adhesion of Thermoresponsive Polymer Brushes. *Langmuir* **2009**, *26* (7), 4762-4768.
131. Boca, S. C.; Astilean, S., Detoxification of gold nanorods by conjugation with thiolated poly(ethylene glycol) and their assessment as SERS-active carriers of Raman tags. *Nanotechnology* **2010**, *21* (23), 235601.
132. Vigderman, L.; Zubarev, E. R., Starfruit-Shaped Gold Nanorods and Nanowires: Synthesis and SERS Characterization. *Langmuir* **2012**, *28* (24), 9034-9040.
133. Haynes, C. L.; McFarland, A. D.; Smith, M. T.; Hulteen, J. C.; Van Duyne, R. P., Angle-Resolved Nanosphere Lithography: Manipulation of Nanoparticle Size, Shape, and Interparticle Spacing. *The Journal of Physical Chemistry B* **2002**, *106* (8), 1898-1902.
134. Kandulski, W. Shadow Nanosphere Lithography. University of Bonn, 2007.

135. (a) New, R. M. H.; Pease, R. F. W.; White, R. L. In *Physical and magnetic properties of submicron lithographically patterned magnetic islands*, Denver, Colorado (USA), AVS: Denver, Colorado (USA), 1995; pp 1089-1094; (b) Shi, J.; Gider, S.; Babcock, K.; Awschalom, D. D., Magnetic Clusters in Molecular Beams, Metals, and Semiconductors. *Science* **1996**, *271* (5251), 937-941.
136. Grabar, K. C.; Smith, P. C.; Musick, M. D.; Davis, J. A.; Walter, D. G.; Jackson, M. A.; Guthrie, A. P.; Natan, M. J., Kinetic Control of Interparticle Spacing in Au Colloid-Based Surfaces: Rational Nanometer-Scale Architecture. *Journal of the American Chemical Society* **1996**, *118* (5), 1148-1153.
137. (a) Street, S. C.; Xu, C.; Goodman, D. W., THE PHYSICAL AND CHEMICAL PROPERTIES OF ULTRATHIN OXIDE FILMS. *Annual Review of Physical Chemistry* **1997**, *48* (1), 43-68; (b) Heiz, U.; Vanolli, F.; Sanchez, A.; Schneider, W. D., Size-Dependent Molecular Dissociation on Mass-Selected, Supported Metal Clusters. *Journal of the American Chemical Society* **1998**, *120* (37), 9668-9671.
138. Wang, Z. L.; Petroski, J. M.; Green, T. C.; El-Sayed, M. A., Shape Transformation and Surface Melting of Cubic and Tetrahedral Platinum Nanocrystals. *The Journal of Physical Chemistry B* **1998**, *102* (32), 6145-6151.
139. Gorer, S.; Ganske, J. A.; Hemminger, J. C.; Penner, R. M., Size-Selective and Epitaxial Electrochemical/Chemical Synthesis of Sulfur-Passivated Cadmium Sulfide Nanocrystals on Graphite. *Journal of the American Chemical Society* **1998**, *120* (37), 9584-9593.
140. (a) Alivisatos, A. P., Perspectives on the Physical Chemistry of Semiconductor Nanocrystals. *The Journal of Physical Chemistry* **1996**, *100* (31), 13226-13239; (b) Andres, R. P.; Bielefeld, J. D.; Henderson, J. I.; Janes, D. B.; Kolagunta, V. R.; Kubiak, C. P.; Mahoney, W. J.; Osifchin, R. G., Self-Assembly of a Two-Dimensional Superlattice of Molecularly Linked Metal Clusters. *Science* **1996**, *273* (5282), 1690-1693.
141. Munro, C. H.; Pajcini, V.; Asher, S. A., Dielectric Stack Filters for Ex Situ and In Situ UV Optical-Fiber Probe Raman Spectroscopic Measurements. *Appl. Spectrosc.* **1997**, *51* (11), 1722-1729.
142. (a) Zou, S.; Williams, C. T.; Chen, E. K. Y.; Weaver, M. J., Probing Molecular Vibrations at Catalytically Significant Interfaces: A New Ubiquity of Surface-Enhanced Raman Scattering. *Journal of the American Chemical Society* **1998**, *120* (15), 3811-3812; (b) Emory, S. R.; Haskins, W. E.; Nie, S., Direct Observation of Size-Dependent Optical Enhancement in Single Metal Nanoparticles. *Journal of the American Chemical Society* **1998**, *120* (31), 8009-8010; (c) Caldwell, W. B.; Chen, K.; Herr, B. R.; Mirkin, C. A.; Hulteen, J. C.; Van Duyne, R. P., Self-Assembled Monolayers of Ferrocenylazobenzenes on Au(111)/Mica Films: Surface-Enhanced Raman Scattering Response vs Surface Morphology. *Langmuir* **1994**, *10* (11), 4109-4115; (d) Pipino, A. C. R.; Van Duyne, R. P.; Schatz, G. C., Surface-enhanced second-harmonic diffraction: Experimental investigation of selective enhancement. *Physical Review B* **1996**, *53* (7), 4162-4169; (e) Zhu, J.; Xu, F.; Schofer, S. J.; Mirkin, C. A., The First Raman Spectrum of an Organic Monolayer on a High-Temperature Superconductor: Direct Spectroscopic Evidence for a Chemical Interaction between an Amine and YBa<sub>2</sub>Cu<sub>3</sub>O<sub>7-δ</sub>. *Journal of the American Chemical Society* **1997**, *119* (1), 235-236.

143. Mirkin, C. A.; Letsinger, R. L.; Mucic, R. C.; Storhoff, J. J., A DNA-based method for rationally assembling nanoparticles into macroscopic materials. *Nature* **1996**, *382* (6592), 607-9.
144. Pan, G.; Kesavamoorthy, R.; Asher, S. A., Nanosecond Switchable Polymerized Crystalline Colloidal Array Bragg Diffracting Materials. *Journal of the American Chemical Society* **1998**, *120* (26), 6525-6530.
145. Joannopoulos, J. D.; Villeneuve, P. R.; Fan, S., Photonic crystals: putting a new twist on light. *Nature* **1997**, *386* (6621), 143-149.
146. Bates, A. K.; Rothschild, M.; Bloomstein, T. M.; Fedynyshyn, T. H.; Kunz, R. R.; Liberman, V.; Switkes, M., Review of technology for 157-nm lithography. *IBM J. Res. Dev.* **2001**, *45* (5), 605-614.
147. Harrison, C.; Park, M.; Chaikin, P. M.; Register, R. A.; Adamson, D. H., Lithography with a mask of block copolymer microstructures. *Journal of Vacuum Science & Technology B: Microelectronics and Nanometer Structures* **1998**, *16* (2), 544-552.
148. (a) Burmeister, F.; Schäfle, C.; Matthes, T.; Böhmisch, M.; Boneberg, J.; Leiderer, P., Colloid Monolayers as Versatile Lithographic Masks. *Langmuir* **1997**, *13* (11), 2983-2987; (b) Ji, W. Y.; Jae, I. S.; Ho, M. A.; Tae, G. K., Fabrication of Nanometer-scale Pillar Structures by Using Nanosphere Lithography. *Journal of the Korean Physical Society* **2011**, *58* (42), 994.
149. (a) Yang, Z.; Huck, W. T. S.; Clarke, S. M.; Tajbakhsh, A. R.; Terentjev, E. M., Shape-memory nanoparticles from inherently non-spherical polymer colloids. *Nat Mater* **2005**, *4* (6), 486-490; (b) Ng, V.; Lee, Y. V.; Chen, B. T.; Adeyeye, A. O., Nanostructure array fabrication with temperature-controlled self-assembly techniques. *Nanotechnology* **2002**, *13* (5), 554.
150. Schlotterbeck, U.; Aymonier, C.; Thomann, R.; Hofmeister, H.; Tromp, M.; Richtering, W.; Mecking, S., Shape-Selective Synthesis of Palladium Nanoparticles Stabilized by Highly Branched Amphiphilic Polymers. *Advanced Functional Materials* **2004**, *14* (10), 999-1004.
151. (a) Andersson, A.-S.; Glasmästar, K.; Hanarp, P.; Seantier, B.; Sutherland, D. S., Patterning colloidal monolayer films using microcontact particle stripping. *Nanotechnology* **2007**, *18* (20), 205303; (b) Silván, M. M.; Hernández, M. A.; Costa, V. T.; Palma, R. J. M.; Duart, J. M. M., Structured porous silicon sub-micrometer wells grown by colloidal lithography. *EPL (Europhysics Letters)* **2006**, *76* (4), 690.
152. Juillerat, F.; Solak, H. H.; Bowen, P.; Hofmann, H., Fabrication of large-area ordered arrays of nanoparticles on patterned substrates. *Nanotechnology* **2005**, *16* (8), 1311.
153. Merkoçi, A., *Biosensing using Nanomaterials*. John Wiley & Sons, Inc. : Hoboken, New Jersey, 2009.
154. Bhaviripudi, S.; Reina, A.; Qi, J.; Kong, J.; Belcher, A. M., Block-copolymer assisted synthesis of arrays of metal nanoparticles and their catalytic activities for the growth of SWNTs. *Nanotechnology* **2006**, *17* (20), 5080.
155. Städler, B.; Solak, H. H.; Frerker, S.; Bonroy, K.; Frederix, F.; Vörös, J.; Grandin, H. M., Nanopatterning of gold colloids for label-free biosensing. *Nanotechnology* **2007**, *18* (15), 155306.
156. Hanarp, P.; Sutherland, D. S.; Gold, J.; Kasemo, B., Control of nanoparticle film structure for colloidal lithography. *Colloids and Surfaces A: Physicochemical and Engineering Aspects* **2003**, *214* (1-3), 23-36.

157. Hultheen, J. C.; Van Duyne, R. P., Nanosphere lithography: A materials general fabrication process for periodic particle array surfaces. *Journal of Vacuum Science & Technology A: Vacuum, Surfaces, and Films* **1995**, *13* (3), 1553-1558.
158. Micheletto, R.; Fukuda, H.; Ohtsu, M., A Simple Method for the Production of a Two-Dimensional, Ordered Array of Small Latex Particles. *Langmuir* **1995**, *11* (9), 3333-3336.
159. (a) Jensen, T. R.; Schatz, G. C.; Van Duyne, R. P., Nanosphere Lithography: Surface Plasmon Resonance Spectrum of a Periodic Array of Silver Nanoparticles by Ultraviolet-Visible Extinction Spectroscopy and Electrodynamic Modeling. *The Journal of Physical Chemistry B* **1999**, *103* (13), 2394-2401; (b) Denkov, N.; Velev, O.; Kralchevski, P.; Ivanov, I.; Yoshimura, H.; Nagayama, K., Mechanism of formation of two-dimensional crystals from latex particles on substrates. *Langmuir* **1992**, *8* (12), 3183-3190; (c) Burmeister, F.; Badowsky, W.; Braun, T.; Wieprich, S.; Boneberg, J.; Leiderer, P., Colloid monolayer lithography-A flexible approach for nanostructuring of surfaces. *Applied Surface Science* **1999**, *144-145* (0), 461-466.
160. (a) Deckman, H. W.; Dunsmuir, J. H., Applications of surface textures produced with natural lithography. *Journal of Vacuum Science & Technology B: Microelectronics and Nanometer Structures* **1983**, *1* (4), 1109-1112; (b) Deckman, H. W.; Dunsmuir, J. H., Natural lithography. *Applied Physics Letters* **1982**, *41* (4), 377-379.
161. Rossi, R. C.; Tan, M. X.; Lewis, N. S., Size-dependent electrical behavior of spatially inhomogeneous barrier height regions on silicon. *Applied Physics Letters* **2000**, *77* (17), 2698-2700.
162. Fulda, K.-U.; Tieke, B., Langmuir films of monodisperse 0.5  $\mu\text{m}$  spherical polymer particles with a hydrophobic core and a hydrophilic shell. *Advanced Materials* **1994**, *6* (4), 288-290.
163. (a) Hoogenboom, J. P.; Rétif, C.; de Bres, E.; van de Boer, M.; van Langen-Suurling, A. K.; Romijn, J.; van Blaaderen, A., Template-Induced Growth of Close-Packed and Non-Close-Packed Colloidal Crystals during Solvent Evaporation. *Nano Letters* **2004**, *4* (2), 205-208; (b) Lu, Y.; Yin, Y.; Xia, Y., A Self-Assembly Approach to the Fabrication of Patterned, Two-Dimensional Arrays of Microlenses of Organic Polymers. *Advanced Materials* **2001**, *13* (1), 34-37.
164. (a) Rogach, A. L.; Kotov, N. A.; Koktysh, D. S.; Ostrander, J. W.; Ragoisha, G. A., Electrophoretic Deposition of Latex-Based 3D Colloidal Photonic Crystals: A Technique for Rapid Production of High-Quality Opals. *Chemistry of Materials* **2000**, *12* (9), 2721-2726; (b) Giersig, M.; Mulvaney, P., Preparation of ordered colloid monolayers by electrophoretic deposition. *Langmuir* **1993**, *9* (12), 3408-3413.
165. Jiang, P.; McFarland, M. J., Wafer-Scale Periodic Nanohole Arrays Templated from Two-Dimensional Nonclose-Packed Colloidal Crystals. *Journal of the American Chemical Society* **2005**, *127* (11), 3710-3711.
166. Fischer, U. C.; Zingsheim, H. P., Submicroscopic pattern replication with visible light. *Journal of Vacuum Science and Technology* **1981**, *19* (4), 881-885.
167. (a) Roxlo, C. B.; Deckman, H. W.; Abeles, B., Molecular Confinement in Nanometer-Size Superlattice Microstructures. *Physical Review Letters* **1986**, *57* (19), 2462-2465; (b) Deckman, H. W.; Moustakas, T. D., Microporous GaAs/GaAlAs superlattices. *Journal of Vacuum Science & Technology B: Microelectronics and Nanometer Structures* **1988**, *6* (1), 316-318; (c) Deckman, H. W.; Dunsmuir, J. H.; Garoff, S.; McHenry, J. A.; Peiffer, D. G., Macromolecular self-organized

assemblies. *Journal of Vacuum Science & Technology B: Microelectronics and Nanometer Structures* **1988**, 6 (1), 333-336.

168. (a) Russell, B. K.; Mantovani, J. G.; Anderson, V. E.; Warmack, R. J.; Ferrell, T. L., Experimental test of the Mie theory for microlithographically produced silver spheres. *Physical Review B* **1987**, 35 (5), 2151-2154; (b) Buncick, M. C.; Warmack, R. J.; Ferrell, T. L., Optical absorbance of silver ellipsoidal particles. *J. Opt. Soc. Am. B* **1987**, 4 (6), 927-933.

169. Rybczynski, J.; Ebels, U.; Giersig, M., Large-scale, 2D arrays of magnetic nanoparticles. *Colloids and Surfaces A: Physicochemical and Engineering Aspects* **2003**, 219 (1-3), 1-6.

170. Zareie, H. M.; Morgan, S. W.; Moghaddam, M.; Maarroof, A. I.; Cortie, M. B.; Phillips, M. R., Nanocapacitive Circuit Elements. *ACS Nano* **2008**, 2 (8), 1615-1619.

171. Coutts, M. J.; Zareie, H. M.; Cortie, M. B.; Phillips, M. R.; Wuhner, R.; McDonagh, A. M., Exploiting Zinc Oxide Re-emission to Fabricate Periodic Arrays. *ACS Applied Materials & Interfaces* **2010**, 2 (6), 1774-1779.

172. Cong, C.; Junus, W.; Shen, Z.; Yu, T., New Colloidal Lithographic Nanopatterns Fabricated by Combining Pre-Heating and Reactive Ion Etching. *Nanoscale Res Lett* **2009**, 4 (11), 1324 - 1328.

173. Xiang, G.; Zhang, N.; Zhou, X., Localized Surface Plasmon Resonance Biosensing with Large Area of Gold Nanoholes Fabricated by Nanosphere Lithography. *Nanoscale Research Letters* **2010**, 5 (5), 818 - 822.

174. Colson, P.; Cloots, R.; Henrist, C., Experimental design applied to spin coating of 2D colloidal crystal masks: a relevant method? *Langmuir* **2011**, 27 (21), 12800-6.

175. Kralchevsky, P. A.; Nagayama, K., Capillary forces between colloidal particles. *Langmuir* **1994**, 10 (1), 23-36.

176. (a) Norris, D. J.; Arlinghaus, E. G.; Meng, L.; Heiny, R.; Scriven, L. E., Opaline Photonic Crystals: How Does Self-Assembly Work? *Advanced Materials* **2004**, 16 (16), 1393-1399; (b) Brewer, D. D.; Allen, J.; Miller, M. R.; de Santos, J. M.; Kumar, S.; Norris, D. J.; Tsapatsis, M.; Scriven, L. E., Mechanistic Principles of Colloidal Crystal Growth by Evaporation-Induced Convective Steering. *Langmuir* **2008**, 24 (23), 13683-13693.

177. Deegan, R. D.; Bakajin, O.; Dupont, T. F.; Huber, G.; Nagel, S. R.; Witten, T. A., Capillary flow as the cause of ring stains from dried liquid drops. *Nature* **1997**, 389 (6653), 827-829.

178. Zhao, Y.; Marshall, J. S., Spin coating of a colloidal suspension. *Physics of Fluids* **2008**, 20 (4), 043302-15.

179. Rehg, T. J.; Higgins, G., Spin coating of colloidal suspensions. *AIChE Journal* **1992**, 38 (4), 489-501.

180. Pollard, A. M.; Heron, C., *Archaeological Chemistry*. Royal Society of Chemistry: 2008.

181. Faraday, M., The Bakerian Lecture: Experimental Relations of Gold (and Other Metals) to Light. *Philosophical Transactions of the Royal Society of London* **1857**, 147, 145-181.

182. (a) Hayat, M. A., *Colloidal gold: principles, methods, and applications*. Academic Press: New York, 1989; (b) Turkevich, J.; Stevenson, P. C.; Hillier, J., A study of the nucleation and growth processes in the synthesis of colloidal gold. *Discussions of the Faraday Society* **1951**, 11 (0), 55-75.

183. (a) Pellegrino, T.; Kudera, S.; Liedl, T.; Muñoz Javier, A.; Manna, L.; Parak, W. J., On the Development of Colloidal Nanoparticles towards Multifunctional Structures and their Possible Use for Biological Applications. *Small* **2005**, *1* (1), 48-63; (b) Elghanian, R.; Storhoff, J. J.; Mucic, R. C.; Letsinger, R. L.; Mirkin, C. A., Selective Colorimetric Detection of Polynucleotides Based on the Distance-Dependent Optical Properties of Gold Nanoparticles. *Science* **1997**, *277* (5329), 1078-1081.
184. Daniel, M.-C.; Astruc, D., Gold Nanoparticles: Assembly, Supramolecular Chemistry, Quantum-Size-Related Properties, and Applications toward Biology, Catalysis, and Nanotechnology. *Chemical Reviews* **2003**, *104* (1), 293-346.
185. Park, K. Synthesis, Characterization, and Self-Assembly of Size Tunable Gold Nanorods Georgia Institute of Technology, 2006.
186. (a) Chen, C.-D.; Cheng, S.-F.; Chau, L.-K.; Wang, C. R. C., Sensing capability of the localized surface plasmon resonance of gold nanorods. *Biosensors and Bioelectronics* **2007**, *22* (6), 926-932; (b) Matcheswala, A. M. Gold Nanospheres and Gold Nanorods as Localized Surface Plasmon Resonance Sensors. University of Kentucky, 2010.
187. Link, S.; Sayed, E., Shape and size dependence of radiative, non-radiative and photothermal properties of gold nanocrystals. *Int. Rev. in Phys. Chem.* **2000**, *19*, 409.
188. Pérez-Juste, J.; Pastoriza-Santos, I.; Liz-Marzán, L. M.; Mulvaney, P., Gold nanorods: Synthesis, characterization and applications. *Coordination Chemistry Reviews* **2005**, *249* (17-18), 1870-1901.
189. El-Sayed, I. H.; Huang, X.; El-Sayed, M. A., Surface Plasmon Resonance Scattering and Absorption of anti-EGFR Antibody Conjugated Gold Nanoparticles in Cancer Diagnostics: Applications in Oral Cancer. *Nano Letters* **2005**, *5* (5), 829-834.
190. Eustis, S.; El-Sayed, M., Aspect Ratio Dependence of the Enhanced Fluorescence Intensity of Gold Nanorods: Experimental and Simulation Study. *The Journal of Physical Chemistry B* **2005**, *109* (34), 16350-16356.
191. Marks, L. D., Experimental studies of small particle structures. *Reports on Progress in Physics* **1994**, *57* (6), 603.
192. Yu; Chang, S.-S.; Lee, C.-L.; Wang, C. R. C., Gold Nanorods: Electrochemical Synthesis and Optical Properties. *The Journal of Physical Chemistry B* **1997**, *101* (34), 6661-6664.
193. Mohamed, M. B.; Ismail, K. Z.; Link, S.; El-Sayed, M. A., Thermal Reshaping of Gold Nanorods in Micelles. *The Journal of Physical Chemistry B* **1998**, *102* (47), 9370-9374.
194. Esumi, K.; Matsuhisa, K.; Torigoe, K., Preparation of Rodlike Gold Particles by UV Irradiation Using Cationic Micelles as a Template. *Langmuir* **1995**, *11* (9), 3285-3287.
195. Jana, N. R.; Gearheart, L.; Murphy, C. J., Wet Chemical Synthesis of High Aspect Ratio Cylindrical Gold Nanorods. *The Journal of Physical Chemistry B* **2001**, *105* (19), 4065-4067.
196. Gole, A.; Murphy, C. J., Seed-Mediated Synthesis of Gold Nanorods: Role of the Size and Nature of the Seed. *Chemistry of Materials* **2004**, *16* (19), 3633-3640.
197. Gao, J.; Bender, C. M.; Murphy, C. J., Dependence of the Gold Nanorod Aspect Ratio on the Nature of the Directing Surfactant in Aqueous Solution. *Langmuir* **2003**, *19* (21), 9065-9070.
198. Wei, Z.; Zamborini, F. P., Directly Monitoring the Growth of Gold Nanoparticle Seeds into Gold Nanorods. *Langmuir* **2004**, *20* (26), 11301-11304.



199. Wei, Z.; Mieszawska, A. J.; Zamborini, F. P., Synthesis and Manipulation of High Aspect Ratio Gold Nanorods Grown Directly on Surfaces. *Langmuir* **2004**, *20* (11), 4322-4326.
200. Nikoobakht, B.; El-Sayed, M. A., Preparation and Growth Mechanism of Gold Nanorods (NRs) Using Seed-Mediated Growth Method. *Chemistry of Materials* **2003**, *15* (10), 1957-1962.
201. Sau, T. K.; Murphy, C. J., Seeded High Yield Synthesis of Short Au Nanorods in Aqueous Solution. *Langmuir* **2004**, *20* (15), 6414-6420.
202. Zweifel, D. A.; Wei, A., Sulfide-Arrested Growth of Gold Nanorods. *Chemistry of Materials* **2005**, *17* (16), 4256-4261.
203. Jana, N. R., Gram-Scale Synthesis of Soluble, Near-Monodisperse Gold Nanorods and Other Anisotropic Nanoparticles. *Small* **2005**, *1* (8-9), 875-882.
204. Kim, F.; Song, J. H.; Yang, P., Photochemical Synthesis of Gold Nanorods. *Journal of the American Chemical Society* **2002**, *124* (48), 14316-14317.
205. Busbee, B. D.; Obare, S. O.; Murphy, C. J., An Improved Synthesis of High-Aspect-Ratio Gold Nanorods. *Advanced Materials* **2003**, *15* (5), 414-416.
206. Wu, H.-Y.; Chu, H.-C.; Kuo, T.-J.; Kuo, C.-L.; Huang, M. H., Seed-Mediated Synthesis of High Aspect Ratio Gold Nanorods with Nitric Acid. *Chemistry of Materials* **2005**, *17* (25), 6447-6451.
207. Pérez-Juste, J.; Liz-Marzán, L. M.; Carnie, S.; Chan, D. Y. C.; Mulvaney, P., Electric-Field-Directed Growth of Gold Nanorods in Aqueous Surfactant Solutions. *Advanced Functional Materials* **2004**, *14* (6), 571-579.
208. Zijlstra, P.; Bullen, C.; Chon, J. W. M.; Gu, M., High-Temperature Seedless Synthesis of Gold Nanorods. *The Journal of Physical Chemistry B* **2006**, *110* (39), 19315-19318.
209. Zareie, M. H.; Xu, X.; Cortie, M. B., In Situ Organization of Gold Nanorods on Mixed Self-Assembled-Monolayer Substrates. *Small* **2007**, *3* (1), 139-145.
210. Caswell, K. K.; Wilson, J. N.; Bunz, U. H. F.; Murphy, C. J., Preferential End-to-End Assembly of Gold Nanorods by Biotin–Streptavidin Connectors. *Journal of the American Chemical Society* **2003**, *125* (46), 13914-13915.
211. Green, H. N.; Martyshkin, D. V.; Rodenburg, C. M.; Rosenthal, E. L.; Mirov, S. B., Gold Nanorod Bioconjugates for Active Tumor Targeting and Photothermal Therapy. *Journal of Nanotechnology* **2011**, *2011*.
212. Liao, H.; Hafner, J. H., Gold Nanorod Bioconjugates. *Chemistry of Materials* **2005**, *17* (18), 4636-4641.
213. Özer, E. Development of end-group functional temperature responsive polymers. İzmir Institute of Technology 2013 in press.
214. Cheung, C. L.; Nikolić, R. J.; Reinhardt, C. E.; Wang, T. F., Fabrication of nanopillars by nanosphere lithography. *Nanotechnology* **2006**, *17* (5), 1339-1343.
215. Smith, D. K.; Korgel, B. A., The Importance of the CTAB Surfactant on the Colloidal Seed-Mediated Synthesis of Gold Nanorods. *Langmuir* **2008**, *24* (3), 644-649.
216. Shumaker-Parry, J. S.; Zareie, M. H.; Aebersold, R.; Campbell, C. T., Microspotting Streptavidin and Double-Stranded DNA Arrays on Gold for High-Throughput Studies of Protein–DNA Interactions by Surface Plasmon Resonance Microscopy. *Analytical Chemistry* **2004**, *76* (4), 918-929.
217. Chan, G. H.; Zhao, J.; Schatz, G. C.; Duyne, R. P. V., Localized Surface Plasmon Resonance Spectroscopy of Triangular Aluminum Nanoparticles. *The Journal of Physical Chemistry C* **2008**, *112* (36), 13958-13963.

218. Haes, A. J., Localized Surface Plasmon Resonance Spectroscopy for Fundamental Studies of Nanoparticle Optics and Applications to Biosensors *Northwestern University Ph.D. Dissertation* **2004**.
219. Jeong, B.; Gutowska, A., Lessons from nature: stimuli-responsive polymers and their biomedical applications. *Trends in Biotechnology* **2002**, *20* (7), 305-311.
220. Nateghi, E. Investigation of Stimuli-Responsive Polymers on Gold Surfaces. University of Technology, Sydney 2007.
221. Zareie, H. M.; Boyer, C.; Bulmus, V.; Nateghi, E.; Davis, T. P., Temperature-Responsive Self-Assembled Monolayers of Oligo(ethylene glycol): Control of Biomolecular Recognition. *ACS Nano* **2008**, *2* (4), 757-765.
222. Lee, S.; Anderson, L. J. E.; Payne, C. M.; Hafner, J. H. Structural Transition in the Surfactant Layer that Surrounds Gold Nanorods as Observed by Analytical Surface-Enhanced Raman Spectroscopy. American Chemical Society, 2011.
223. Yu, C.; Irudayaraj, J., Multiplex Biosensor Using Gold Nanorods. *Analytical Chemistry* **2006**, *79* (2), 572-579.

## CURRICULUM VITAE

**Aysel TOMAK**

**Place and Date of Birth:** İZMİR / 17.08.1988

**Address:** 832/2 Sokak No:1 Bornova/İZMİR

**Tel:** 0532 697 60 86

**E-Mail:** tomakaysel@gmail.com

### EDUCATION AND RELATED EXPERIENCE

**2011- present** Nanotechnology Master Programme, Gediz University, Izmir/Turkey

**2008-2009** Master of Chemistry Programme (Without Thesis), Celal Bayar University, Manisa/Turkey

**2004-2008** BSc. Chemistry, Faculty of Science and Literature, Celal Bayar University, Manisa/Turkey

**Research Interest:** Biosensor, Synthesis of various metallic Nanoparticles, Nanorods and Nanobubbles, Nanolithography, Self-Assembled Monolayer, Characterization Techniques such as: Scanning Probe Microscopes, Surface Enhanced Raman Scattering, Surface Plasmon Resonance, Localized Surface Plasmon Resonance, Coating Techniques.

### EXPERIENCE

**2011-present** TUBITAK research project scholar

### OTHER QUALIFICATIONS

**Computer skills:** Excellent in Windows, Microsoft Office: (word, excel, power point)

## CONFERENCE PARTICIPATIONS

**2012**                      2<sup>nd</sup> International Advances in Applied Physics and Materials  
Science Congress, Antalya Turkey, April, 26-29, 2012.